Ab Initio Modeling of the Structures and Catalytic Properties of Selected Mononuclear, Dinuclear, Supramolecular, and Periodic Metal-Organic Complexes

A THESIS

SUBMITTED TO THE FACULTY OF THE GRADUATE SCHOOL

OF THE UNIVERSITY OF MINNESOTA

BY

Aaron B. League

IN PARTIAL FULFILLMENT OF THE REQUIREMENTS

FOR THE DEGREE OF

DOCTOR OF PHILOSOPHY

Professor Christopher J. Cramer

July, 2016

Acknowledgements

The completion of my doctorate degree marks what is perhaps the most significant milestone in my life to date. I have been in school of one form or another almost continuously since the age of four, so one might say that earning my PhD is an achievement more than 20 years in the making. A comprehensive list of the people who have had an impact in my life in that time is beyond the scope of this section (and, alas, my memory) but here are the highlights.

First and foremost, I would like to thank my advisor, Prof. Christopher J. Cramer, without whose support and guidance I would have had neither the courage nor the knowledge to get to this point. Chris has been, to me, the ideal of what a teacher should be: slow to anger, consistently available, and ludicrously good at explaining things.

In a similar vein, I'd like to thank a number of faculty who helped, encouraged, and challenged me along the way: Profs. Rita Majerle, Melissa Skeate, Marina Gorina, Michelle Driessen, Steven R. Kass, Wayne Bosma, Alberto Delgado, Matthew Timm, Michael Lang, and Troy Halvorsen. Thanks especially to Profs. Bosma and Kass for letting me work for them for a summer each to gain research experience, and to Prof. Halvorsen, from whom I took no fewer than four chemistry classes, and who first instilled in me a love of the subject.

School in general (and graduate school in particular) can be a real roller coaster of emotions, and the people on whom I've leaned during the worst times deserve a lot of credit for sticking around as long as they have (or as long as they did). Utmost thanks, in no particular order, to my parents Richard and Vanessa League, my brother Graham,

Dedication

For

my father,

who paved the way

Labor omnia vincit.

Abstract

Numerous varieties of metal-organic compounds have been synthesized to date, ranging in size from complexes containing only one or two metal atoms to supramolecular clusters, cages, and periodic latices. Metal-organic compounds can be tuned for a multitude of applications by modifying organic ligands and metal centers to select for desired size, shape, and electronic properties. Because of the complicated nature of many such systems, characterization of them can be a challenge. Mechanisms of reactivity, too, are notoriously difficult to characterize experimentally; as the saying goes, "If you can isolate the species, it probably isn't important to the mechanism." Theory can be of assistance in both cases.

Herein, we investigate the properties of a variety of metal-organic systems, including mononuclear and dinuclear ruthenium water oxidation catalysts, supramolecular Cu(I) and Fe(II) host-guest complexes, and a metal-organic framework modified with single-site Ni(II) and Co(II). In each case, we are able to use *ab initio* methods to provide some valuable insight into the system: for the water oxidation catalysts, we examine the effects on catalytic efficacy of modifications to the ligand systems in order to advise the development of even better catalysts; for the host-guest complexes, we help to explain the binding trends observed between small molecules that incorporate into the internal cavities of the cages; and for the metal-organic framework, we take steps toward elucidating the structure resulting from deposition of Ni(II), as well as giving insight into the mechanisms by which the deposited metals catalyze ethylene hydrogenation and oligomerization.

Contents

List of Tables

List of Figures

---

[a] Peaks for the S_4 isomer of [$C_{70} \subset 1$] could not be clearly identified due to their low intensity and are not marked. We estimate this isomer accounts for ca. 5% of the total distribution.

List of Schemes

[b] The two representations shown are X-ray crystal structures. One configuration of the trigold guest is shown.

[c] $[Cu(Au(CN)_2)_2 \subset \mathbf{1c}\text{-}D_4]$ is shown as the X-ray crystal structure.

List of Abbreviations

AIM	:	ALD in MOFs
ALD	:	Atomic layer deposition
CASPT2	:	Complete active space second order perturbation theory
CASSCF	:	Complete active space self-consistent field method
CCSD(T)	:	Coupled cluster on single, double, and perturbative triple excitations
CV	:	Cyclic voltammetry
DCM	:	Dichloromethane
DFT	:	Density functional theory
DOSY	:	Diffusion-ordered nuclear magnetic resonance spectroscopy
ED	:	Electron donating
EW	:	Electron withdrawing
EXAFS	:	Extended X-ray absorption fine structure
GGA	:	Generalized gradient approximation
HF	:	Hartree Fock theory
HOMO	:	Highest occupied molecular orbital
LDA	:	Local density approximation
LSDA	:	Local spin density approximation
LUMO	:	Lowest unoccupied molecular orbital
MALDI	:	Matrix-assisted laser desorption/ionization
MGGA	:	Meta-generalized gradient approximation
MLCT	:	Metal-to-ligand charge transfer
MO	:	Molecular orbital
MOF	:	Metal-organic framework
MS	:	Mass spectrometry
NHE	:	Normal hydrogen electrode
NMR	:	Nuclear magnetic resonance spectroscopy

PAH	:	Polycyclic aromatic hydrocarbon
PCET	:	Proton-coupled electron transfer
PS	:	Photosensitizer
rds	:	Rate-determining step
SCE	:	Saturated calomel electrode
SEA	:	Sacrificial electron acceptor
SQWV	:	Square wave voltammetry
SSCE	:	Sodium saturated calomel electrode
SVD	:	Singular value decomposition
TM	:	Transition metal
TOF	:	Turnover frequency
TON	:	Turnover number
TS	:	Transition state
UV	:	Ultraviolet spectroscopy
UV-vis	:	Ultraviolet and visible spectroscopy
WNA	:	Water nucleophilic attack
WOC	:	Water oxidation catalyst
XANES	:	X-ray absorption near edge structure
ZORA	:	Zero-order regular approximation

Preface

Parts of this thesis have been reproduced from previously published work. Permissions to reproduce these sections have been obtained, and are as follows:

Chapter 2.1: Water oxidation catalysis with ligand substituted Ru-bpp type complexes

Adapted with permission from

S. Roeser, F. Bozoglian, C. J. Richmond, A. B. League, M. Z. Ertem, L. Francàs, P. Miró, J. Benet-Buchholz, C. J. Cramer, and A. Llobet, *Catal. Sci. Technol.*, **2016**, Advance Article, **DOI**: 10.1039/C6CY00197A – Published by The Royal Society of Chemistry.

Supporting Information: `http://www.rsc.org/suppdata/c6/cy/c6cy00197a/c6cy00197a1.pdf`

Chapter 2.2: Mechanisms and Factors Controlling Photoisomerization Equilibria, Ligand Exchange, and Water Oxidation Catalysis Capabilities of Mononuclear Ruthenium(II) Complexes

Adapted with permission from

M. Hirahara, T. Hakamata, A.B. League, M.Z. Ertem, K. Takahashi, S. Nagai, K. Inaba, H. Yamazaki, K. Saito, T. Yui, C.J. Cramer, and M. Yagi, *Eur. J. Inorg. Chem.*, **2015**, 3892. **DOI**: 10.1002/ejic.201500642 – Copyright © 2015 WILEY-VCH Verlag GmbH & Co. KGaA, Weinheim.

Supporting Information: `http://onlinelibrary.wiley.com/store/10.1002/ejic.201500642/asset/supinfo/ejic_201500642_sm_miscellaneous_information.pdf?v=1&s=ee9fc4b67160beee6d139a0b6e546b5146ca85ca`

Chapter 3.1: Empirical and Theoretical Insights into the Structural Features and Host-Guest Chemistry of M_8L_4 Tube Architectures

Adapted with permission from

W. Meng, A.B. League, T.K. Ronson, J.K. Clegg, W.C. Isley III, D. Semrouni, L. Gagliardi, C.J. Cramer, and J.R. Nitschke, *J. Am. Chem. Soc.* **2014**, 136 (10), 3972. **DOI**: 10.1021/ja412964r – Copyright © 2014 American Chemical Society.

Supporting Information: `http://pubs.acs.org/doi/suppl/10.1021/ja412964r`

Chapter 3.2: Pyrene-Edged Fe(II)$_4$L$_6$ Cages Adaptively Reconfigure During Guest Binding

Adapted with permission from

T.K. Ronson, A.B. League, L. Gagliardi, C.J. Cramer, and J.R. Nitschke, *J. Am. Chem. Soc.* **2014**, 136 (44), 15615. **DOI**: 10.1021/ja507617h – Copyright © 2014 American Chemical Society.

Supporting Information: `http://pubs.acs.org/doi/suppl/10.1021/ja507617h`

Chapter 4.1: Sintering-Resistant Single-Site Nickel Catalyst Supported by Metal-Organic Framework

Adapted with permission from

Z. Li, N.M. Schweitzer, A.B. League, V. Bernales, A.W. Peters, A. Getsoian, T.C. Wang, J.T. Miller, A. Vjunov, J.L. Fulton, J.A. Lercher, C.J. Cramer, L. Gagliardi, J.T. Hupp, and O.K. Farha, *J. Am. Chem. Soc.* **2016**, 138 (6), 1977 **DOI**: 10.1021/jacs.5b12515 – Copyright © 2016 American Chemical Society.

Supporting Information: `http://pubs.acs.org/doi/suppl/10.1021/jacs.5b12515`

Chapter 1

Introduction

1.1 Overview

The past few decades have seen explosive growth in the field of metal-organic chemistry. With an increasing understanding of the interactions possible between transition metals and the ligand systems that chelate them, and with an ever expanding array of synthetic techniques that make possible the creation of complexes of which previous generations of chemists could only dream, chemists and chemical engineers alike have set their sights on some of the toughest remaining challenges in catalysis: chemical water oxidation, alkane activation, and molecular shape recognition for enzyme-mimetic catalysis. Pick the right transition metal and the perfect ligand system, and the possibilites, it seems, are endless. But with rapid growth comes a commensurate ungainliness in the strides we take.

Theory can be an enormous help in guiding and focusing experiment. Using theory, we can check mechanistic pathways for viability, explain the reasons for different reaction rates between modified complexes, work synergistically with X-ray crystallographers to elucidate difficult structures, suggest rational ways to modify compounds to increase catalytic activity, and even examine the properties of large numbers of real and theoretical systems *via* high-throughput theoretical methods.

For many of the questions that arise when studying chemical systems, Density Functional Theory (DFT) stands out among theoretical methods because it offers a balance between chemical accuracy and computational thrift. This thesis contains several case studies of such complexes, where we have used DFT to elucidate some combination of structural and catalytic properties. Hence, it will be useful to examine the method in some detail.

1.2 Computational Methods

1.2.1 Density Functional Theory

The electron density (the product of the wave function with its complex conjugate) is a physical observable which makes an intuitive choice for use in computation. An electron density contains almost all of the same information as a wave function (it does not contain phase information or the many-body structure of the wave function), but is a physical observable.

In 1964, Hohenberg and Kohn proved two theorems which set the stage for the rise of DFT as a means of computing electronic energy.[8] The first theorem showed that an external potential (the interactions between electrons and non-electron particles and fields) is uniquely defined by a ground-state density, which gives rise to the Hamiltonian operator. The Hamiltonian operator, in turn, defines the ground state and all excited state wave functions.

The second theorem proved a variational principle for the density; that is, it showed that the expectation value of the electronic energy obtained from any candidate density cannot be less than the true ground-state energy of the functional in use. Equation 1.2.1 shows the mathematical representation of this theorem, where $\mathbf{H}_c$ and $|\Psi_c\rangle$ are the Hamiltonian and wave function determined from the candidate density, and E_0 is the true ground-state energy.[9]

$$\langle \Psi_c | \mathbf{H}_c | \Psi_c \rangle \geq E_0 \qquad (1.2.1)$$

The Kohn-Sham Method

If Hohenberg and Kohn set the stage for modern DFT in 1964, then the curtain was lifted by Kohn and Sham in 1965.[10] In their paper, Kohn and Sham defined electronic

energy as a density functional (a function whose domain is a vector space – in this case the density – and whose range is a scalar value, to wit, the electronic energy) by starting with a system where the Hamiltonian was that of a system without electron interaction, but which had the density of the real system, in which electron interaction was accounted for.[9] In this formalism, the determinant of non-interacting electrons used to construct the density was not, in the strictest sense, a wave function, but gave the same density as the true wavefunction. Constructing the density in this way allowed for the calculation of kinetic energies for the non-interacting electrons.

The energy functional $E[\rho(\mathbf{r})]$ can be split into the following components

$$E[\rho(\mathbf{r})] = T_{ni}[\rho(\mathbf{r})] + V_{ne}[\rho(\mathbf{r})] + V_{ee}[\rho(\mathbf{r})] + \underbrace{\Delta T[\rho(\mathbf{r})] + \Delta V_{ee}[\rho(\mathbf{r})]}_{E_{xc}[\rho(\mathbf{r})]} \qquad (1.2.2)$$

where T_{ni} is the kinetic energy of non-interacting electrons, V_{ne} and V_{ee} are classical nuclear-electron and electron-electron interactions, respectively, and ΔT and ΔV_{ee} are quantum mechanical corrections to the electron kinetic energy and electronic repulsions to recover electronic correlation.[9] The first three terms on the right hand side of Equation 1.2.2 have intuitive mathematical forms complementary to those defined for HF theory, because the difficulty incurred by including electronic correlation has been neatly combined into the final two terms, which are typically jointly represented by an $E_{xc}[\rho(\mathbf{r})]$ term. This term is commonly known as the exchange-correlation functional.

Exchange-Correlation Functionals

Having grouped the difficult terms in equation 1.2.2 together, the challenge then becomes finding a functional form for them. The exchange-correlation energy is more easily modeled for a uniform electron gas (a constant electron density and a constant positive charge dispersed over all space), so by assuming that the energy of each point

in a given density is equivalent to that of a uniform electron gas having the same density, an approximation to the electronic energy can be calculated.[10] This assumption is known as the Local Density Approximation (LDA).[9]

Generalized Gradient Approximation (GGA) functionals take this method a step further and compute the energy associated with a point in space based not only on the density at that point, but also on the gradient of the density at that point. Meta-GGA (MGGA) functionals add also a dependency on either the kinetic energy density or on the Laplacian of the electron density.[9] Together, LDA, GGA, and MGGA functionals define a class of functionals commonly termed "local".

Because local functionals can sometimes overestimate or underestimate the stabilizing effect of electron correlation on the energy of a system, some functionals replace part of their exchange-correlation energy with that of HF exchange. While HF exchange can be included in a number of ways, one of the simplest follows the equation

$$E_{xc} = (1 - a)E_{xc}^{DFT} + aE_x^{HF} \tag{1.2.3}$$

where E_{xc}^{DFT} is the correlation-exchange energy calculated by DFT, E_x^{HF} is the HF exchange energy, and a is an empirical parameter.[9] These comprise a second class of functionals termed "hybrid".

Dispersion Corrections to DFT

Although they can give excellent results for covalently bonded systems, traditional density functionals tend to grossly underestimate the energetics of dispersion interactions (*e.g.* $\pi - \pi$ stacking). Because the chemistry relevant to some of the complexes described in this thesis depends strongly on non-bonded interactions, such errors are often not within the range of what may be considered acceptable. Some modern functionals, such as the M06 family, are well parameterized for mid-range interactions, and

consequently tend to perform well for dispersion interactions without any empirical correction.[11] However, the tendency to underestimate dispersion energies persists in many of the older well-loved functionals. As a means of improving the performance of popular functionals, Antony and Grimme have shown that adding a damped imperical dispersion term to the electronic energy of some test functionals increased their accuracy in predicting dispersion interactions to nearly a coupled-cluster CCSD(T) level.[12]

The equation below shows the form of Grimme's D3 dispersion correction,[13] which is subtracted from the regular DFT energy.

$$E_{\text{disp}} = E^{(2)} + E^{(3)} \tag{1.2.4}$$

This dispersion term includes two-body ($E^{(2)}$) and three-body ($E^{(3)}$) interactions. The two-body term accounts for the bulk of the correction, and is given by

$$E^{(2)} = \sum_{AB} \sum_{n=6,8,10,\ldots} s_n \frac{C_n^{AB}}{r_{AB}^n} f_{d,n}\left(r_{AB}\right) \tag{1.2.5}$$

where n represent the order of dispersion, s_n are global scaling factors dependent on functional, C_n^{AB} are atomic dispersion coefficients for atom pair AB, and r_{AB} is the distance between nuclei of atoms A and B. The $f_{d,n}$ terms are damping functions, which correct asymptotic behavior at small internuclear distances. Two general forms of damping function have been tested, and the relative value of each for varying applications has been studied in detail.[14]

Polarizable Continuum Solvation: the SMD Solvation Model

When modeling a molecule, the default option is to represent only that molecule surrounded by infinite empty space. This is a good approximation of the gas phase for a substance, in which molecules tend to be far apart. However, a significant portion of reactions which might be of interest for computational study take place not in the gas

phase, but in a liquid solution. The effects of solvent stabilization (or destabilization) of a complex often cannot be ignored, especially in charged systems like many of those we wish to model. However, since *ab initio* methods tend to scale as some power of the number of basis functions, the addition of a sufficient quantity of solvent molecules to surround even small structures can become prohibitively expensive. Consequently, the effects of solvation are often computed using an implicit solvent – that is, modeling only the physical characteristics of bulk solvent and not the solvent molecules themselves.

One such model, SMD, is a good example of the state of the art in the field of implicit solvation, and a method which we employ regularly.[15] In this method, the free energy of solvation is decomposed as

$$\Delta G_{\mathrm{S}}^{\circ} = \Delta G_{\mathrm{ENP}} + \Delta G_{\mathrm{CDS}} + \Delta G_{\mathrm{conc}}^{\circ} \tag{1.2.6}$$

where the first term on the right-hand side of the equation represents the nuclear, electronic, and polarization components – the largest components of $\Delta G_{\mathrm{S}}^{\circ}$. The term ΔG_{CDS} is for cavitation, dispersion, and solvent structure. This term represents the change in free energy involved in creating a cavity in the solvent for the solute molecule, any dispersion interactions between the solute and solvent, and any organization of the solvent surrounding the solute. Finally, the term $\Delta G_{\mathrm{conc}}^{\circ}$ in Equation 1.2.6 represents the change in free energy associated with increasing the concentration of the solute from the gas phase (typically 22.4 L mol^{-1}) to the liquid phase (typically 1 M).

1.3 Organization of the Thesis

In this thesis, quantum chemical methods are applied to address questions regarding metal-organic complexes of varying size and complexity. In Chapter 2, we explore the effects of ligand substitution on the mechanistic cycles of mononuclear and dinuclear ruthenium water oxidation catalysts. In Chapter 3, we examine the ability of

supramolecular cages to bind, and even to act as templates for, small molecules selectively based on the size, shape, and polarity of their internal cavities. Lastly, in Chapter 4 we consider a periodic metal-organic framework as a scaffold for atomic-layer-deposited single-site Ni and Co, and model their ability to catalyze ethylene hydrogenation and oligomerization. Each chapter is summarized briefly below.

Chapter 2: Water Oxidation by Ruthenium Catalysts

Sunlight is the principal source of energy for our planet, and yet human-made methods for direct capture of solar energy have as yet proven problematic. Not only are photovoltaic solar panels bulky and difficult to transport for mobile use, but, somewhat tautologically, they are also highly dependent on direct sunlight in order to function with maximal efficacy. Since our demand for electricity persists even at night and on rainy days, the idea of storing solar energy by using it to produce chemical fuel is an attractive one.

Molecular hydrogen is a practical choice as a target for the conversion of solar energy to fuel, since H_2 combustion produces a considerable amount of energy and no greenhouse gasses. Hydrogen gas can be produced *via* oxidation of water (Equation 1.3.1) and subsequent recombination of the resulting protons and electrons. The whole process, known as artificial photosynthesis, can be driven by the potential from a photovoltaic cell, as shown in Figure 1.3.1, where water oxidation occurs at the cathode and proton reduction occurs at the anode.

$$2H_2O \rightarrow O_2 + 4H^+ + 4e^- \quad E^\circ = 1.23V \text{ vs. NHE at pH} = 0 \qquad (1.3.1)$$
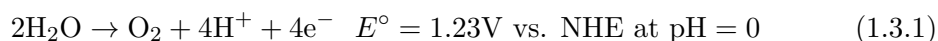
Both water oxidation and proton reduction require catalysts to function effectively, but while the problem of proton reduction is already fairly well understood, better – and cheaper – water oxidation catalysts are needed. Metal-organic ruthenium complexes
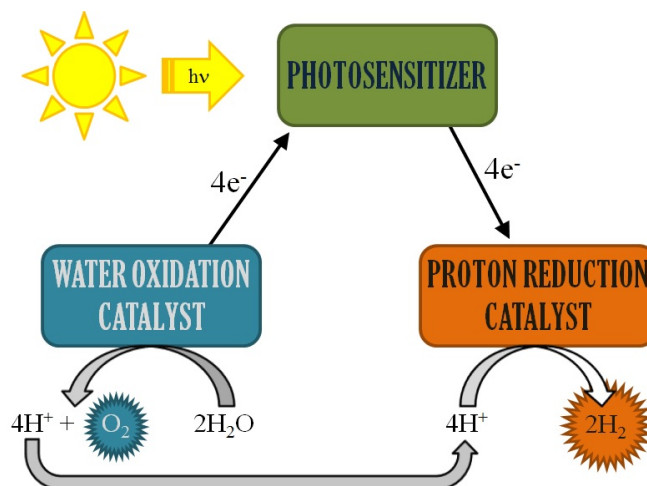
Figure 1.3.1: Diagram of the basic design of an artificial photosynthetic device.

have shown some of the greatest efficacy among water oxidation catalysts, and, despite ruthenium being too expensive a metal to make widespread use economically viable, studying the mechanisms by which these complexes work can offer insight into how to build better catalysts.

2.1 Water oxidation catalysis with ligand substituted Ru-bpp type complexes. The dinuclear Ru-Hbpp complex $[Ru(trpy)(H_2O)]_2(\mu\text{-bpp})^{3+}$ (trpy is 2,2':6':2"-terpyridine, bpp is 3,5-bis(2-pyridyl)pyrazolato) has been previously reported as an effective catalyst for water oxidation.[16] The advantage of this catalyst is that it forms a bis-(Ru=O) species under catalytic conditions, which can readily undergo intramolecular formation of an O-O bond (the rate limiting step for many WOCs, see Figure 1.3.2). In fact, the barrier for O-O bond formation is lowered so significantly that it is no longer the rate limiting step, yielding instead to the displacement of O_2 by water.

In this section, we examine the effect of modifications in the ligand system of Ru-Hbpp on its catalytic efficacy. By modeling the substitution of one of the trpy ligands of the complex with an electron donating (-OCH$_3$) or electron withdrawing (-NO$_2$)
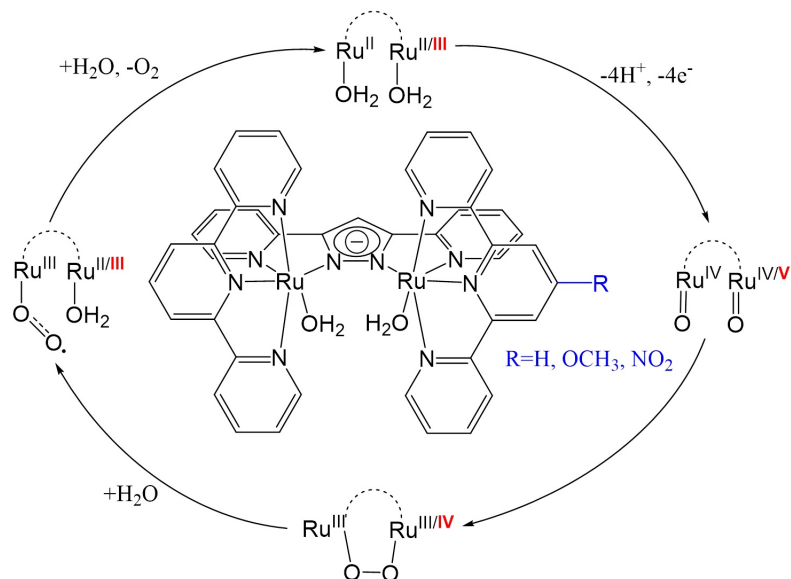
Figure 1.3.2: Depiction of the structure of Ru-Hbpp and proposed mechanistic cycle for water oxidation catalysis. In the computational study, -R was replaced with -NO$_2$ or -OCH$_3$.

group (Figure 1.3.2), we are able to modify the relative energy of the rate limiting O$_2$ displacement step.

2.2 Mechanisms and Factors Controlling Photoisomerization Equilibria, Ligand Exchange, and Water Oxidation Catalysis Capabilities of Mononuclear Ruthenium(II) Complexes. In this section, we consider replacement of the naphthyridine moiety with an analogous quinoline moiety in mononuclear water oxidation catalyst [Ru(tpy)(pynp)OH$_2$]$^{2+}$ [tpy = 2,2';6',2"-terpyridine, pynp = 2-(2-pyridyl)-1,8-naphthyridine]. The substitution amounts to the replacement of nitrogen with carbon, and produces complex [Ru(tpy)(pyqu)OH$_2$]$^{2+}$ [pyqu = 2-(2'-pyridyl)quinoline]. Upon photoexcitation, both the parent and the substituted complex are found to transition from their *distal* to their *proximal* isomers (Figure 1.3.3). However, in the

$[Ru(tpy)(pynp)OH_2]^{2+}$ $[Ru(tpy)(pyqu)OH_2]^{2+}$
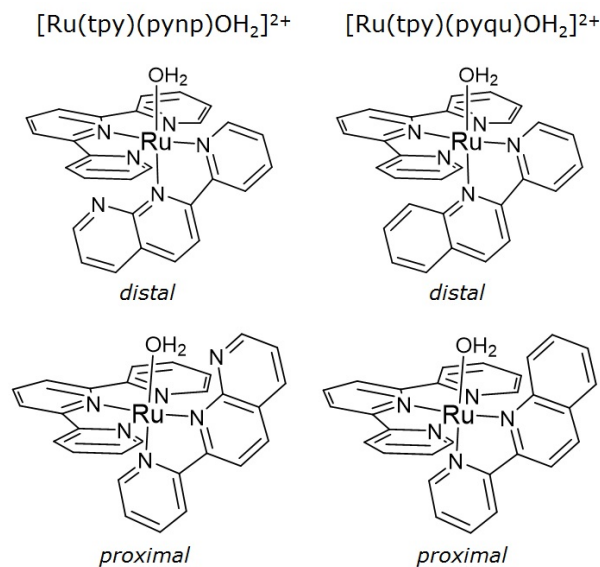
Figure 1.3.3: Depiction of the distal and proximal isomers of $[Ru(tpy)(pynp)OH_2]^{2+}$ and $[Ru(tpy)(pyqu)OH_2]^{2+}$.

parent complex, strong intramolecular interactions between the naphthyridine nitrogen and the water ligand make *distal* $\rightarrow$ *proximal* isomerization irreversible. Replacing the nitrogen with a carbon moiety allows the reverse photoisomerization process to occur. We have modeled the forward and reverse photoisomerization pathways for $[Ru(tpy)(pyqu)OH_2]^{2+}$ for comparison against those previously reported for $[Ru(tpy)(pynp)OH_2]^{2+}$.[17]

The efficacy of both *distal* and *proximal* isomers of $[Ru(tpy)(pynp)OH_2]^{2+}$ for water oxidation catalysis has been reported previously,[17] and we here extend the study to include both isomers of $[Ru(tpy)(pyqu)OH_2]^{2+}$ as well.

Chapter 3: Supramolecular Cages as a Source of Enzyme-Mimetic Shape Recognition

Since the advent of the self-assembled supramolecular structure about two decades ago, the growth of this field of research has been tremendous.[18–21] The metal-organic complexes of interest to us in this chapter have a few aspects in common: they consist of metal centers held together by organic ligands, and their formation from separate subcomponents occurs spontaneously. Metals used for these cages include copper, iron, cobalt, and platinum. The organic ligands – with some notable exceptions – either connect two metal centers *via* an edge, or can cap an entire face.
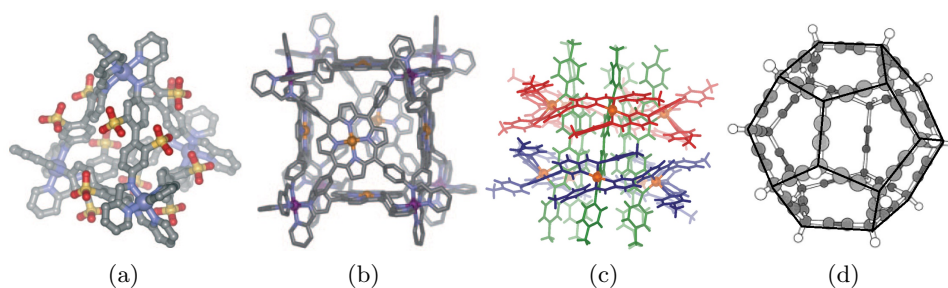
Figure 1.3.4: (a) An edge-linked water-soluble sulfonated $Fe(II)_4L_6^{-4}$ tetrahedron.[1] (b) A face-capped $Fe(II)_8L_6$ cube with porphyrin ligands.[2] (c) An edge-linked $Co(II)_{10}L_{15}^{+20}$ pentagonal prism.[3] (d) A dodecahedron of alternative design, where Pt(II) connects organic edges to organic vertices[4] (edges added in black for clarity). All structures were copied from the articles in which they were originally published. Structures (a), (b), and (d) are simplified for clarity.

Figure 1.3.4 shows some examples of the wide variety of structures that can be obtained even within the constraints outlined above. Structures (a) and (b) both have Fe(II) vertices (blue and purple, respectively) each bound to three bidentate ligands, but while the edge-linked ligands in (a) show preference for a tetrahedral structure,[1] the face-capped porphyrin ligands of (b) force the complex to adopt a cubic configuration.[2]

The ligands of complex (a) have been modified with sulfonate groups (yellow and red) bearing negative charges, making the complex soluble in water. In structure (b), the porphyrin ligands can be centered around an H_2 molecule or a metal, so the charge on the complex can vary.[2]

Complex (c) is formed by rearrangement of a 2:3 metal to ligand complex similar to (a) but with Co(II) centers instead of Fe(II).[3] This rearrangement occurs spontaneously at a slow rate, but can also be brought on by the addition of perchlorate anion, which acts as a template for the formation of the larger structure.

In complex (d), both edges and vertices are organic, and are connected by platinum(II) metal centers. The reaction scheme for the formation of complex (d) is shown in Figure 1.3.5, where the nitrogen in each pyridyl group replaces a triflate on a platinum center to form the cage.[4] This cage differs from the other three in that it uses two different linkers to connect metal centers.
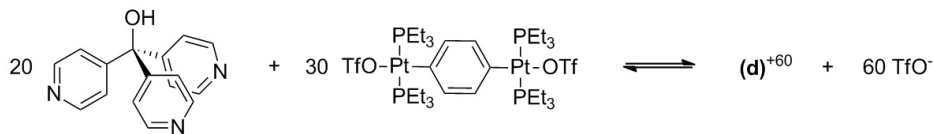
Figure 1.3.5: Complex (d) uses a tetrahedral carbon ligand for vertices and a linear ligand for edges.[4]

The capacity of such coordination cages as those shown above for containing small molecules has given rise to a field of study called host-guest chemistry, where cages are referred to as "hosts" and the encapsulated small molecules are called "guests". Host-guest chemistry has been used to modify reactions in a number of distinct ways. Guest encapsulation can increase the rate of a reaction by bringing reactants together in the internal cavity of a host molecule or decrease the reaction rate by isolating reactive intermediates (or even starting materials) from the reaction mixture.[20, 22]
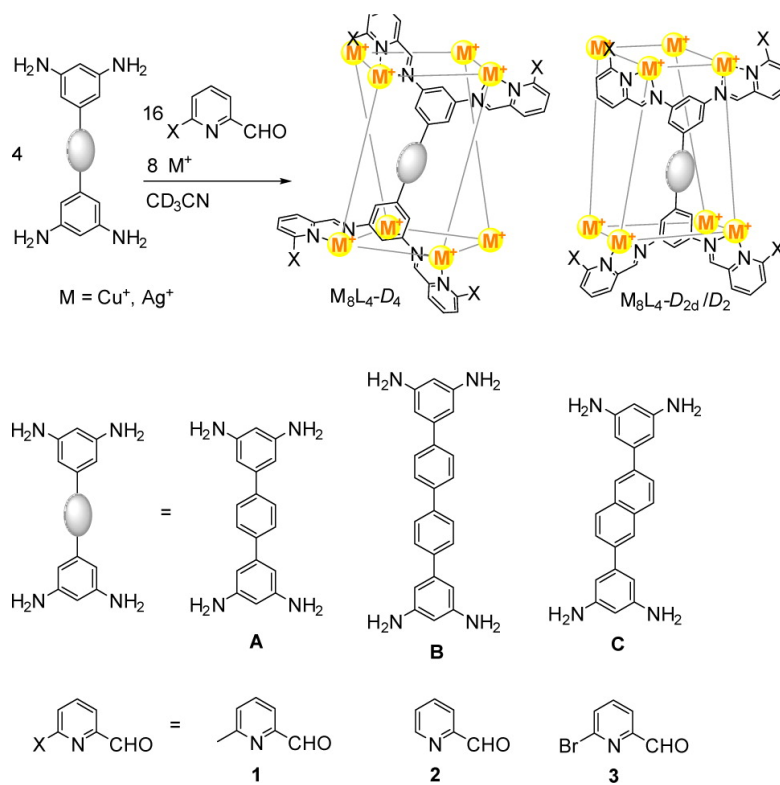
Scheme 1.3.1: General synthesis of M_8L_4 tubes. (L represents the organic linker.)

Empirical and Theoretical Insights into the Structural Features and Host-Guest Chemistry of M_8L_4 Tube Architectures. In this section, we examine supramolecular cages formed spontaneously in solution from Cu(I) and Ag(I), 2-formylpyridines, and large tetraamines (Scheme 1.3.1), whose long, narrow, internal cavities are able to encapsulate guest molecules. In fact, the presence of dicyano group-11-metalates in the solution can result in the formation inside of the host cages of linear cyanometalate guests which have not been found to form elsewhere. We have modeled a number of the host systems computationally in order to better understand the experimentally observed trends in preferential binding between Cu(I), Ag(I), and Au(I) metalates.
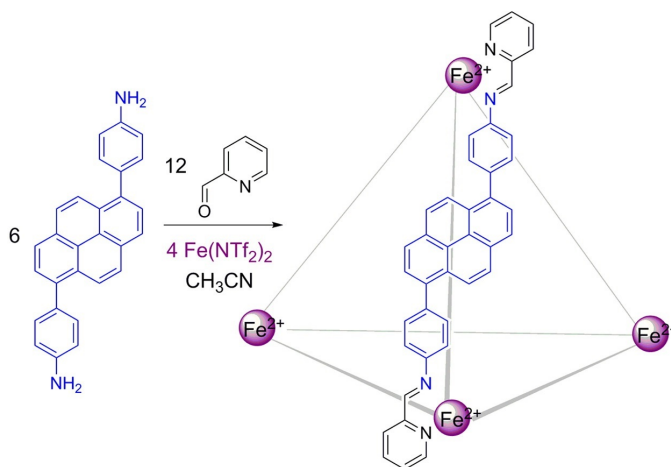
Scheme 1.3.2: General synthesis of $Fe(II)_4L_6$ tetrahedra.

Pyrene-Edged $Fe(II)_4L_6$ Cages Adaptively Reconfigure During Guest Binding. In this section, we examine the host-guest chemistry of large tetrahedral Fe(II) cages whose linkers contain pyrene rings (Scheme 1.3.2). The linkers in these cages are so long and flexible, that each of the iron centers can adopt either a Δ or a Λ local symmetry independent of one another, leading to three unique nearly isoenergetic

diastereomers (Figure 1.3.6), as determined by ^{1}H NMR. The internal cavities of these cages are large enough that they encapsulate C_{60} and C_{70} fullerenes. However, guest encapsulation leads to a simplification of the NMR signal: one of the isomers is apparently not suitable for guest binding, and rearranges in the presence of the fullerenes to form a more suitable host for guest encapsulation. We have modeled the host-guest chemistry of all three diastereomers, and offer an explanation for why only two of them bind guests
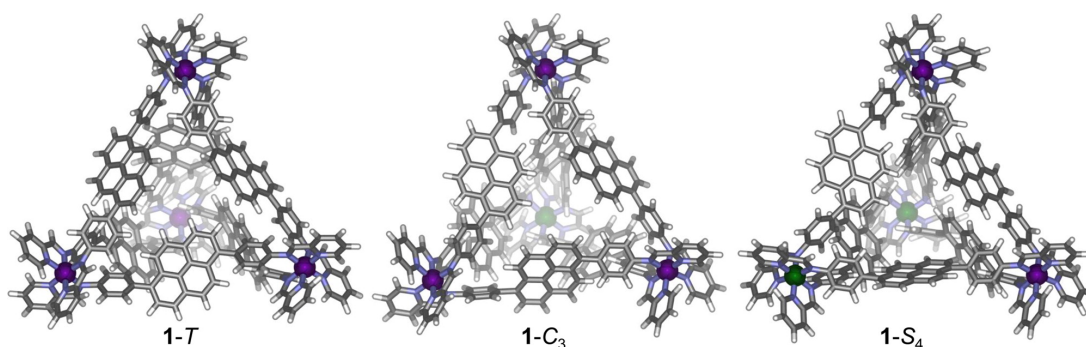
Figure 1.3.6: DFT-optimized structures of the three diastereomers of **1**. Fe(II) centers with Δ and Λ stereochemistry are colored purple and green, respectively.

Chapter 4: Metal-Organic Frameworks as Supports for Heterogeneous Catalysts

In recent years, the number of publications involving Metal-Organic Frameworks (MOFs) has skyrocketed. The idea behind these materials is relatively simple: much like the host complexes described above, MOFs are composed of metals or metal clusters connected by organic linkers. However, unlike in supramolecular cages, in MOFs the linkers and metals form periodic two- or three-dimensional frameworks.

MOFs are of particular interest as supports for heterogeneous catalysts, because

the number of active sites in a heterogeneous catalyst is proportionate to the surface area of the support, and the pores of MOFs allow them to have some of the highest effective surface areas of any class of materials currently known. Reactions of interest for catalysis include activation of alkanes and C-C bond formation, which have broad applications for commercial processes.

In this chapter, we consider the material that results from Atomic Layer Deposition (ALD) of Ni(II) into MOF NU-1000 (Figure 1.3.7; NU-1000 is composed of $Zr_6(\mu_3\text{-}O)_4(\mu_3\text{-}OH)_4(H_2O)_4(OH)_4$ nodes and tetratopic 1,3,6,8-(p-benzoate)pyrene ($TBAPy^{4-}$) linkers). Because ALD is a gas-phase process, the considerable heat released does not have a solvent to help dissipate it. Consequently, we believe, the MOF experiences a loss of crystallinity upon substrate deposition. We therefore did not have a reliable crystal structure from which to begin our computational study.
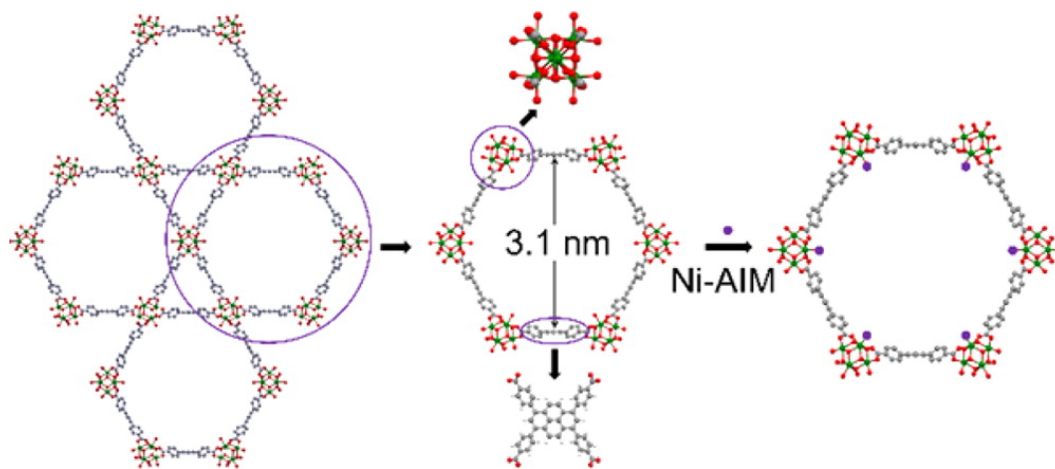
Figure 1.3.7: Structural representation of NU-1000, highlighting its organic linker, mesoporous channel, and Zr_6-containing node and a schematic depiction of the process used to anchor Ni to the Zr_6 node of NU-1000 *via* AIM.

4.1 Sintering-Resistant Single-Site Nickel Catalyst Supported by Metal-Organic Framework. In this section, we present the characterization of the material

Ni@NU-1000 – elucidated by comparison of computationally optimized structures to EXAFS data. The material has been found to be a robust catalyst for the hydrogenation of ethylene, which, by the principle of microscopic reversibility, is mechanistically identical to the dehydrogenation of ethane. While ethane is relatively inert, ethylene is a vital precursor in a great many industrial processes; hence, a durable and effective catalyst for converting ethane to ethylene would be a valuable tool.

We have undertaken a computational study of the conversion of ethylene to ethane by Ni@NU-1000, and have discovered a low barrier for the reaction, in agreement with experiment.

4.2 Computationally-Guided Discovery of Active Cobalt-Decorated Metal-Organic Framework for Ethylene Oligomerization. In this section, we examine the ability of single-site Ni(II) and Co(II) deposited on NU-1000 to catalyze ethylene oligomerization. The calculated energetics of three possible catalytic cycles are compared, as illustrated by Figure 1.3.8. Cycle I involves the generation of an active catalyst by C-H bond activation of ethylene to form a vinyl-metal species (with proton transfer to a coordinated oxide or hydroxide). In Cycle II, two ethylene molecules are bound to the metal at once, and then form a metallocyclic intermediate. Finally, in Cycle III, the catalyst is pre-activated with Et$_2$AlCl, which we assume for the sake of simplicity generates an ethylmetal species.

Experimentally, Ni(II) is observed to form a much more effective catalyst than Co(II) for ethylene oligomerization. We investigate the electronic structure of the rate-determining transition states for both catalysts in order to understand this trend.
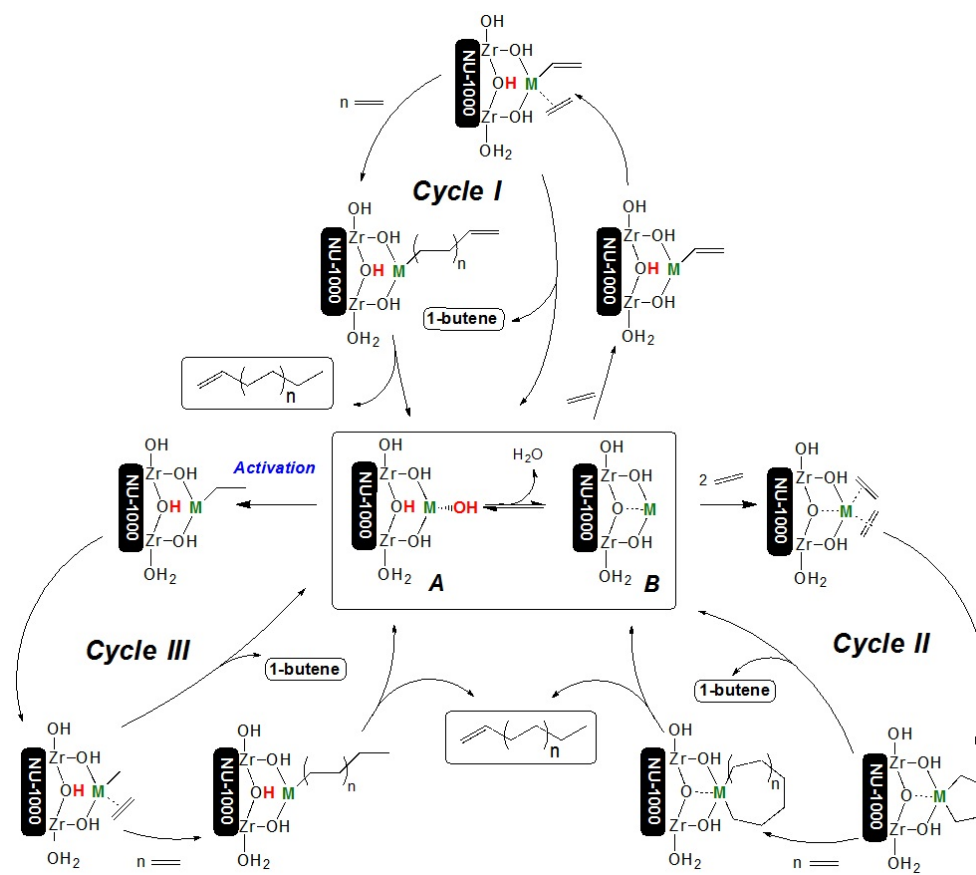
Figure 1.3.8: Schematic representation of three mechanistic pathways for ethylene oligomerization mediated by M-AIM+NU-1000, where M = Co(II) or Ni(II) metal. Linkers of the MOF are omitted for clarity.

Chapter 2

Water Oxidation by Ruthenium Catalysts

2.1 Water oxidation catalysis with ligand substituted Ru-bpp type complexes

2.1.1 Introduction

Water splitting by sunlight is considered a contributing approach to solving today's increasing energy-demand challenges as it could eventually lead to an economy based on clean, sustainable energy sources such as hydrogen and/or methanol.[23–26] Overall water splitting with light was first accomplished in an artificial manner in 1972 by Fujishima and Honda, however this required high energy UV irradiation due to the high bandgap of the TiO_2 semiconductor used.[27] In addition to shifting light absorbance from the UV to the visible region, catalytic water oxidation is also one of the key reactions that needs to be optimized in order to produce viable technological devices.[28–30] Two primary factors make water oxidation a challenging task for a catalyst: i) the large endoergonicity of the reaction, $2H_2O \rightarrow O_2 + 4H^+ + 4e^-$ $E° = 1.23$ V (vs. NHE at pH = 0); and ii) the molecular complexity from a mechanistic point of view, since two protons and two electrons have to be removed from each of the two water molecules and an oxygen-oxygen bond has to be formed between them. The first well-characterized molecular catalyst to achieve this complex reaction was presented in 1982 by Meyer and coworkers, involving the archetypal complex $[(bpy)_2(OH_2)Ru]_2(\mu\text{-}O)^{4+}$, (bpy is 2,2'-bipyridine), the so called Blue-dimer.[31] This dinuclear ruthenium based complex has been thoroughly studied mechanistically, although its activity is relatively low in terms of turnover number (TON) and turnover frequency (TOF). Substantial progress was made when in 2004 Llobet *et al.* presented a dinuclear ruthenium based complex, bridged by a pyrazolato based dinucleating tetraaza ligand, 3,5-bis(2-pyridyl)pyrazolato (bpp⁻) and containing the tridentate meridional trpy (trpy is 2,2':6':2"-terpyridine) of

formula $[Ru(trpy)(H_2O)]_2(\mu\text{-bpp})^{3+}$ and labeled as $\mathbf{15^{3+}}$ in Scheme 2.1.1.[16] This more rugged framework presented a record efficiency of up to 70% at that time under catalytic conditions and high TONs of up to 510 were achieved.[5,6] A number of dinuclear and trinuclear Ru complexes with different levels of performance have subsequently been reported.[32–42]

In this section, we explore the effect of electronic perturbations exerted by the ligand framework on the Ru-bpp type of water oxidation catalyst. For this purpose we have prepared new complexes of general formula $[Ru(R^2\text{-trpy})(H_2O)][Ru(R^3\text{-trpy})(H_2O)](\mu\text{-}R^1\text{-bpp})^{3+}$ ($\mathbf{16^{3+}}$-$\mathbf{21^{3+}}$) whose structures are presented in Scheme 2.1.1 together with a labeling scheme for these complexes and their μ-Cl and μ-OAc precursors ($\mathbf{1^{2+}}$-$\mathbf{14^{2+}}$). In these new complexes the bpp$^-$ and trpy ligands have been substituted with electron-donating and electron-withdrawing groups at the central pyrazolate unit and/or at the 4' position of the trpy ligands. In this way we have prepared symmetric ($\mathbf{15^{3+}}$-$\mathbf{19^{3+}}$) and non-symmetric ($\mathbf{20^{3+}}$-$\mathbf{21^{3+}}$) Ru-aqua dinuclear complexes with different types of electronic perturbations exerted by the auxiliary ligand framework.

2.1.2 Results and Discussion

Synthesis and Structure

The synthesis of complexes $\mathbf{1^{2+}}$-$\mathbf{5^{2+}}$ and $\mathbf{8^{2+}}$-$\mathbf{13^{2+}}$ are described elsewhere.[43] The procedure used for the synthesis of complexes $\mathbf{6^{2+}}$ and $\mathbf{7^{2+}}$ is based on the previously described[16] synthetic route for complex $\mathbf{1^{2+}}$ adapted for microwave irradiation and is outlined in Scheme 2.1.1. The process consists of the reaction between $[RuCl_3(4'\text{-}R^3\text{-trpy})]$ (R^3 = OMe, NH$_2$) and complex out-$[Ru(Cl)(Hbpp)(trpy)]^{2+}$ in the presence of N-ethylmorpholine (serving as both reducing agent and base) in ethanol, generating a mixture of isomeric dinuclear compounds with the general composition of $[Ru_2(Cl)_2(R^2\text{-}trpy)(R^3\text{-trpy})](\mu\text{-}R^1\text{-bpp})^{2+}$ in addition to the chloro-bridged dinuclear complexes $\mathbf{6^{2+}}$

1²⁺: R¹,R²,R³ = H
2²⁺: R¹ = Me; R²,R³ = H
3²⁺: R¹ = H; R²,R³ = Me
4²⁺: R¹ = H; R²,R³ = OMe
5²⁺: R¹ = NO₂; R², R³ = H
6²⁺: R¹,R² = H; R³ = OMe
7²⁺: R¹,R² = H; R³ = NH₂

8²⁺: R¹,R²,R³ = H
9²⁺: R¹ = Me; R²,R³ = H
10²⁺: R¹ = H; R²,R³ = Me
11²⁺: R¹ = H; R²,R³ = OMe
12²⁺: R¹ = NO₂; R², R³ = H
13²⁺: R¹,R² = H; R³ = OMe
14²⁺: R¹,R² = H; R³ = NH₂

15³⁺: R¹,R²,R³ = H
16³⁺: R¹ = Me; R²,R³ = H
17³⁺: R¹ = H; R²,R³ = Me
18³⁺: R¹ = H; R²,R³ = OMe
19³⁺: R¹ = NO₂; R², R³ = H
20³⁺: R¹,R² = H; R³ = OMe
21³⁺: R¹,R² = H; R³ = NH₂
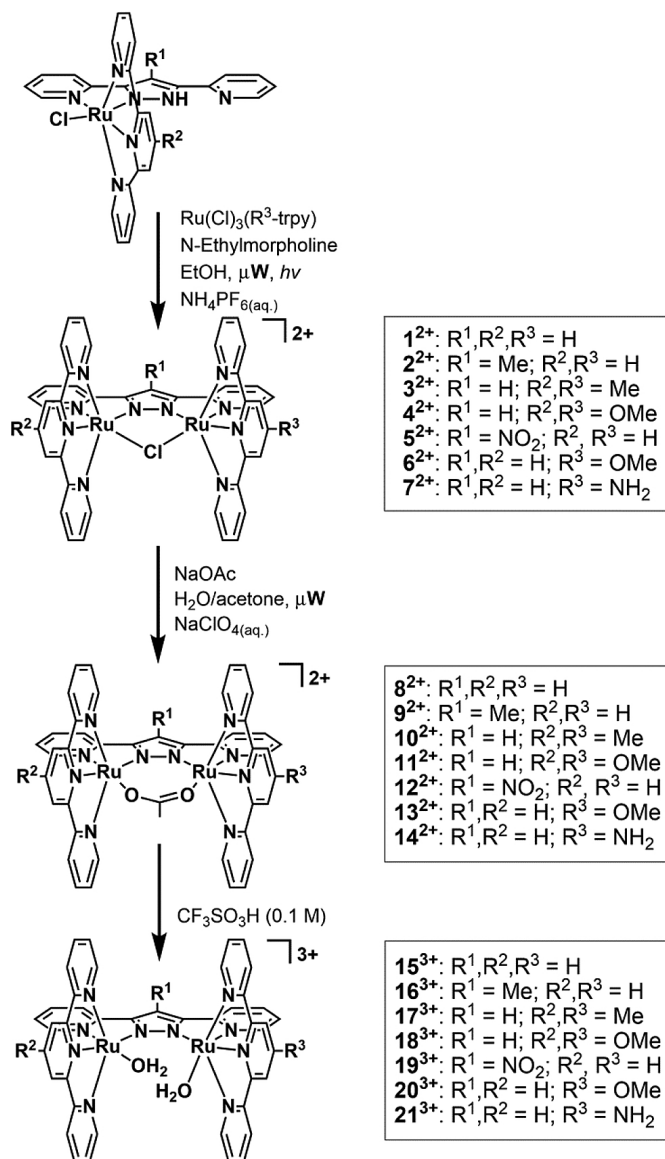
Scheme 2.1.1: General synthetic strategy for the synthesis of complexes $\mathbf{1}^{2+}$-$\mathbf{21}^{3+}$.

(R^1, R^2 = H, R^3 = OMe) or $\mathbf{7}^{2+}$ (R^1, R^2 = H, R^3 = NH_2). The isomeric mixture of din-uclear complexes was completely converted into the desired chloro-bridged compounds through light irradiation overnight.

Despite no effort having been made to optimize the duration of the light driven isomerization process, the microwave synthesis described here still presents significant advantages over the conventional synthesis, in terms of both reaction time and work-up steps. The reaction time of the original published procedure is cut in half, as the first step is completed within a few hours instead of refluxing overnight. The work-up is also much quicker, involving only filtration and washing of the residue with DCM, instead of column chromatography, to obtain the desired complexes with a high degree of purity. The bridging chloro-ligand is easily replaced with an acetato ligand by refluxing complexes $\mathbf{6}^{2+}$ or $\mathbf{7}^{2+}$ in a mixture of acetone/water (4:1) with excess sodium acetate to give complexes $\mathbf{13}^{2+}$ and $\mathbf{14}^{2+}$ respectively. Finally, acid hydrolysis of the μ-OAc Ru dinuclear complexes leads to the *in situ* formation of complexes $\mathbf{15}^{3+}$-$\mathbf{21}^{3+}$.

The bridged compounds reported here for the first time – namely $\mathbf{6}^{2+}$, $\mathbf{7}^{2+}$, $\mathbf{13}^{2+}$ and $\mathbf{14}^{2+}$ – were thoroughly characterized using a variety of spectroscopic (NMR, MS, UV-vis) and electrochemical techniques. Additionally, suitable crystals for single crystal X-ray diffraction were obtained for complexes $\mathbf{6}^{2+}$ and $\mathbf{14}^{2+}$. Figure 2.1.1 shows the Ortep plot for the cationic moiety of these two complexes, whose metric parameters are similar to previously reported Ru(II) complexes with related ligands.[16,44–47] It is worth mentioning that complex $\mathbf{6}^{2+}$ presents a pseudo-σ symmetry plane containing the bpp$^-$ ligand and the Ru metal centers, that bisects the perpendicular trpy ligands. The Me group of the MeO substituent is located outside of this plane, although at room temperature it rotates very fast. From an NMR perspective this fast rotation simplifies ^{1}H- and ^{13}C-NMR assignments. On the other hand, in complex $\mathbf{14}^{2+}$ the replacement of the Cl-bridge by an OAc-bridge produces a distortion in the planarity that eliminates

the mentioned pseudo-σ symmetry plane, due to the large binding angle of the acetato bridge acting in a κ-O^2 fashion. All 1D and 2D NMR spectra are reported in the ESI with their corresponding assignments.
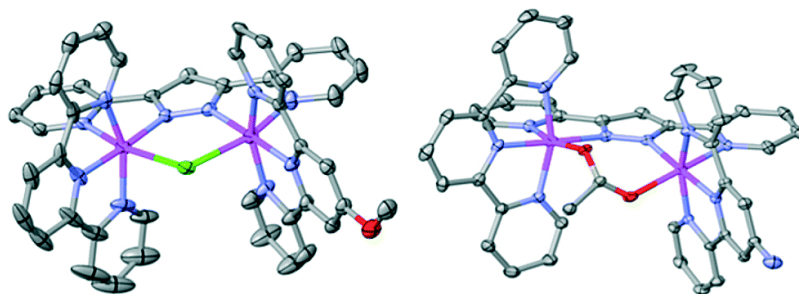
Figure 2.1.1: Ortep plot (ellipsoids at 30%) of complex $\mathbf{6}^{2+}$ (left) and $\mathbf{14}^{2+}$ (right). Hydrogen atoms are not shown. Color code: Ru, magenta; N, blue; O, red; Cl, green; C, grey.

UV-Vis Spectroscopy

Optical properties of the complexes described in this work were analyzed by UV-vis spectroscopy. Table 2.1.1 summarizes the main features of the Ru-aqua complexes $\mathbf{15}^{3+}$-$\mathbf{21}^{3+}$ whereas Figure 2.1.2 shows their UV-vis spectra in a 4:1 volumetric ratio mixture of 0.1 M triflic acid and acetone (data also in Table 2.1.1). Acetone was used as a cosolvent to overcome the very low solubility of these complexes in plain aqueous solutions.

In the UV-vis absorption spectra of the dinuclear Ru-bpp compounds, three main regions can be distinguished: one between 200 and 350 nm, in which very intense bands are observed due to intraligand $\pi - \pi^*$ transitions; another between 350 and 550 nm, in which there are mainly broad unsymmetrical Ru(dπ)-bpp/trpy (π^*) metal-to-ligand charge transfer (MLCT) bands; and finally, the region above 550 nm, in which d-d transitions occur. The transition bands in this region of the μ-Cl-, μ-OAc-complex are

Complex	Assignment	$\lambda_{\max}(\mathrm{nm})(\epsilon(\mathrm{M}^{-1}\mathrm{cm}^{-1}))$
15[3+]	$\pi \to \pi^*$	261 (55 000), 304 (59 300)
	$\mathrm{d}\pi \to \pi^*$	355 (18 000), 460 (12 500), 485 (10 500)
16[3+]	$\pi \to \pi^*$	263 (57 800), 305 (57 900)
	$\mathrm{d}\pi \to \pi^*$	354 (18 800), 454 (11 800), 486 (9200)
17[3+]	$\pi \to \pi^*$	225 (52 500), 263 (55 600), 303 (54 300)
	$\mathrm{d}\pi \to \pi^*$	353 (20 600), 465 (12 400), 489 (11 200)
18[3+]	$\pi \to \pi^*$	241 (48 000), 272 (55 300), 308 (47 100)
	$\mathrm{d}\pi \to \pi^*$	357 (20 200), 478 (12 500), 502 (11 500)
19[3+]	$\mathrm{d}\pi \to \pi^*$	360 (13 000), 452 (11 900), 491 (13 600), 545 (8300)
20[3+]	$\pi \to \pi^*$	232 (47 000), 272 (58 200), 310 (52 900)
	$\mathrm{d}\pi \to \pi^*$	358 (20 900), 471 (12 000), 500 (10 800)
21[3+]	$\pi \to \pi^*$	232 (51 300), 273 (61 100), 312 (51 700)
	$\mathrm{d}\pi \to \pi^*$	366 (18 200), 468 (11 800)

Table 2.1.1: UV-vis data for complexes **15**[3+]-**21**[3+], recorded in acetone : CF_3SO_3H (0.1 M) (1:4)

clearly red shifted ($\approx$10 nm and $\approx$20 nm respectively) with regard to the analogous Ru-aqua complex (see ESI). This is in accordance with the capacity of the anionic chlorido/acetato ligand to destabilize $\mathrm{d}\pi$-orbitals, with the effect being slightly higher for the acetato ligand. The MLCT-transitions of the μ-Cl dinuclear compounds **1**[2+]-**7**[2+] are of very high similarity to each other. For the μ-OAc dinuclear compounds **8**[2+]-**14**[2+], only minor bathochromic shifts can be observed by adding electron donating (ED) substituents to the ligand backbone. This can be explained by the relatively similar energies of the trpy and bpp$^-$ π^* orbitals, that might dilute the destabilizing effect associated with substitution on only a single ligand, or by the potential hybridization (*i.e.* covalent mixing) of the $\mathrm{d}\pi$(Ru) and π(trpy and/or bpp$^-$) orbitals.[43]

Noteworthy differences in the MLCT region are observed for the Ru-dinuclear aqua complexes. A general trend is identified concerning the addition of electron donating substituents onto the trpy ligand as shown in Figure 2.1.2 and its inset. Each MeO-group added (1$\times$ complex **20**[3+], 2$\times$ complex **18**[3+]), causes a red shift of about 10
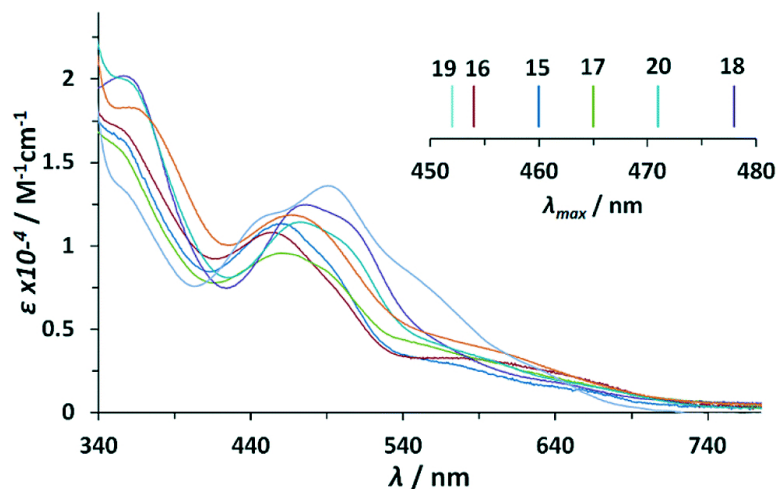
Figure 2.1.2: UV-vis absorption spectra recorded in acetone:CF_3SO_3H (0.1 M) (1:4) of complexes 15^{3+}-21^{3+}. Color code: blue, 15^{3+}; red, 16^{3+}; green, 17^{3+}; violet, 18^{3+}; light blue, 19^{3+}; turquoise 20^{3+}; orange, 21^{3+}. Inset, λ_{max} of the first MLCT transition as a function of substituent.

nm with respect to unsubstituted complex 15^{3+}. The addition of two methyl groups in complex 17^{3+} generates only a shift of about 5 nm, reflecting their less electron-donating character. In sharp contrast, the addition of a methyl group onto the 4'-position of the pyrazole ring bridging ligand in complex 16^{3+}, induces a blue shift of about 8 nm, indicating that the π^*-orbital is strongly affected (destabilized) by ED-substituents on the bpp$^-$ moiety. An even larger blue shift combined with a slightly different absorption pattern can be observed for complex 19^{3+} containing the electron withdrawing NO_2 group. The blue shift can be explained by the large stabilizing effect of the electron withdrawing (EW) nitro-substituent on dπ-orbitals.[43]

The UV-vis spectroscopic properties of the higher oxidation states derived from the Ru-aqua-complex 20^{3+} were investigated *via* spectrophotometric redox titration using Ce(IV) as oxidant and their UV-vis spectra are presented in Figure 2.1.3. As observed previously,[16] the absorption intensity in the visible region decreases with increasing

oxidation state until a broad plain band is observed in the highest accessible stable redox state III,IV. Upon further oxidation to the IV,IV redox state a series of kinetic events is triggered accompanied with the release of molecular oxygen and thus its spectrum was calculated using singular value decomposition (SVD) analysis.
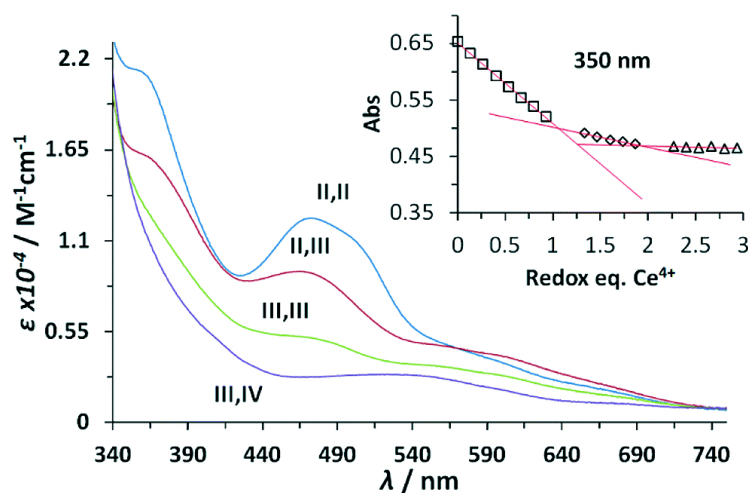
Figure 2.1.3: Absorption spectra (MLCT region) of complex $\mathbf{20}^{3+}$ and its higher oxidation state species in CF_3SO_3H (0.1 M). Oxidation was achieved by consecutive addition of Ce(IV). Inset shows absorption change at 350 nm during each oxidation step (black squares, $Ru_2^{II,II} \rightarrow Ru_2^{II,III}$, diamonds $Ru_2^{II,III} \rightarrow Ru_2^{III,III}$, triangles $Ru_2^{III,III} \rightarrow Ru_2^{III,IV}$), plus the corresponding linear fitting (red lines).

Redox Properties

The redox properties of the complexes described in this work were investigated by means of cyclic voltammetry (CV) and square wave voltammetry (SQWV) using a sodium saturated calomel electrode (SSCE) as a reference electrode, Pt wire as an auxiliary electrode and a glassy carbon disk as a working electrode. All the potentials reported here are *vs*. SSCE. Table 2.1.2 displays a summary of the redox potentials obtained for the first four oxidative processes associated with the transition from $Ru_2^{II,II}$ to $Ru_2^{IV,IV}$ for

Ru-aqua complexes ($\mathbf{15^{3+}}$-$\mathbf{21^{3+}}$). Their voltammograms are shown in Figure 2.1.4 for $\mathbf{20^{3+}}$ and in the ESI for the others. From Table 2.1.2 it can be observed that, in general, electron donating groups decrease redox potentials and electron withdrawing groups increase them as expected, although the overall influence is smaller than expected. The cyclic voltammogram shown in Figure 2.1.4 shows a set of four waves up to 1.3 V that we associate with 4 consecutive one-electron processes. A Pourbaix diagram for $\mathbf{20^{3+}}$ was also built and is displayed in Figure 2.1.5 within the pH range 0-2. At higher pH the low solubility of the complexes prevented further electrochemical analysis. Nevertheless it allowed the full assignment of the degree of oxidation and protonation of the species derived from $\mathbf{20^{3+}}$ from its initial II,II oxidation state. In addition, in the CV for $\mathbf{20^{3+}}$ in Figure 2.1.4, above 1.3 V a large electrocatalytic wave appears associated with the oxidation of water to molecular dioxygen upon reaching the [O=Ru$^\mathrm{V}$Ru$^\mathrm{IV}$=O] oxidation state. The high reactivity of such a [Ru$^\mathrm{V}$=O] moiety has already been described for mononuclear ruthenium compounds and it has also been proposed recently for dinuclear species.[37,48,49] These new findings suggest that an additional redox process should be included in the mechanism previously proposed,[5,6] which is discussed in the following section. Bulk electrolysis experiments were carried out by dissolving complex $\mathbf{20^{3+}}$ (5.4 $\times$ 10^{-5} M) in CF$_3$SO$_3$H (0.1 M). The catalyst produced a total of 23 μmol of O$_2$ at E_app = 1.45 V and 13 μmol at E_app = 1.1 V after 10 hours, corresponding to a final TON of 47 and 27 respectively (see ESI). The results obtained here clearly show that complex $\mathbf{20^{3+}}$ can act as a catalyst both at oxidation state IV,IV and IV,V with the latter being more active.

Complex	$E_{1/2}(1)\Delta E$	$E_{1/2}(2)\Delta E$	$E_{1/2}(3)\Delta E$	$E_{1/2}(4)\Delta E$
15^{3+}	0.56 (80)	0.625 (70)	0.855 (70)	1.07 (60)
16^{3+}	0.50 (60)	0.635 (60)	0.85 (60)	0.96 (60)
17^{3+}	0.51 (60)	0.61 (60)	0.83 (60)	1.06 (60)
18^{3+}	0.50 (60)	0.59 (60)	0.84 (60)	1.02 (60)
19^{3+}	0.74 (60)	0.74 (60)	1.00 (60)	1.10 (60)
20^{3+}	0.50 (60)	0.59 (80)	0.88 (100)	0.98 (80)
21^{3+}	0.48 (60)	0.64 (60)	0.80 (60)	0.97 (80)

Table 2.1.2: Electrochemical data $E_{1/2}(1)$ Ru$^{\text{III,II-II,II}}$, $E_{1/2}(2)$ Ru$_2^{\text{III,III-III,II}}$, $E_{1/2}(3)$ Ru$_2^{\text{IV,III-III,III}}$ and $E_{1/2}(4)$ Ru$_2^{\text{IV,IV-IV,III}}$ ($E_{1/2}$ (V), $\Delta E = E_{\text{p,a}} - E_{\text{p,c}}$ (mV)) for complexes **15**$^{3+}$-**21**$^{3+}$ recorded in acetone:CF$_3$SO$_3$H (0.1 M) (1:4) *vs*. SSCE.

Substitution Kinetics

Whereas it is known that in high oxidation states the kinetics of substitution reactions slow down,[5,6] there is no information on how different substituents on the ligand backbone influence the reaction rates (k_s) in dinuclear systems such as the ones in the present work. Therefore, we measured the substitution kinetics of the aqua ligands by MeCN in CF$_3$SO$_3$H (0.1 M) solution, according to Equations 2.1.1 and 2.1.2, for complexes **19**$^{3+}$ and **20**$^{3+}$ and compared the rate constants with those of the parent complex **15**$^{3+}$.

$$\text{H}_2\text{O-Ru}^{\text{II}}\text{Ru}^{\text{II}}\text{-H}_2\text{O} + \text{MeCN} \rightarrow \text{H}_2\text{O-Ru}^{\text{II}}\text{Ru}^{\text{II}}\text{-NCMe} + \text{H}_2\text{O} \qquad (2.1.1)$$

$$\text{H}_2\text{O-Ru}^{\text{II}}\text{Ru}^{\text{II}}\text{-NCMe} + \text{MeCN} \rightarrow \text{MeCN-Ru}^{\text{II}}\text{Ru}^{\text{II}}\text{-NCMe} + \text{H}_2\text{O} \qquad (2.1.2)$$

Substitution reactions described in Equations 2.1.1 and 2.1.2 generate complexes [Ru(trpy)(H$_2$O)](μ-bpp)[Ru(trpy)(MeCN)]$^{3+}$ and [Ru(trpy)(MeCN)]$_2$(μ-bpp)$^{3+}$ as final products, respectively. Substitution reactions were carried out under pseudo-first-order reaction conditions ([MeCN]/[dinuc] $\geq$ 10) and were monitored by UV-vis spectroscopy. The change in absorption over time for complex **20**$^{3+}$ is shown in the ESI. The resulting rate constants for the first and second substitution reactions are given in Table 2.1.3. As
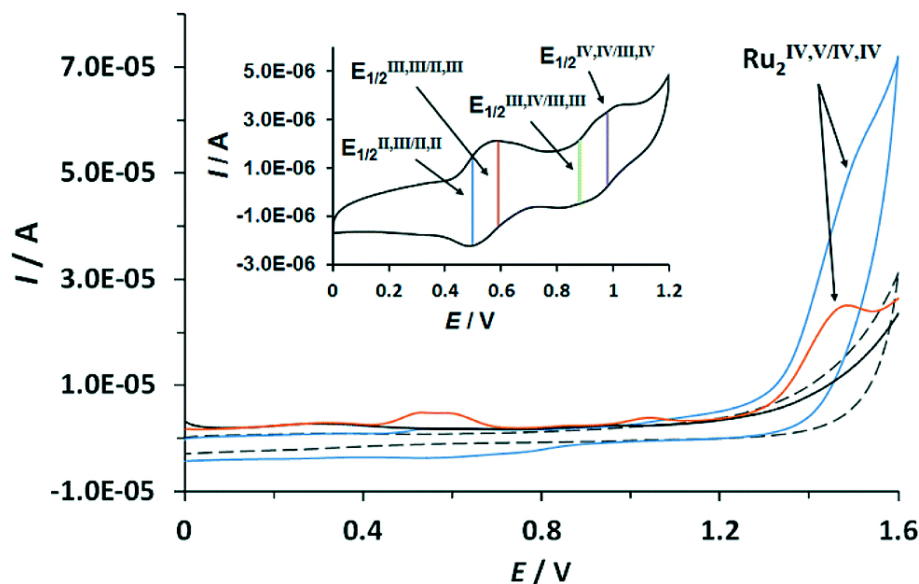
Figure 2.1.4: CV (blue line) and SWV (orange line) of complex 20^{3+} *vs*. SSCE in CF_3SO_3H (0.1 M). Blank CV (dashed grey line) and blank SWV (black line) of pure CF_3SO_3H (0.1 M) is additionally presented. Inset, CV of complex 20^{3+} acetone : CF_3SO_3H (0.1 M) (1:4) at a scan rate of 50 mV s^{-1} with the reverse potential at 1.2 V.

can be observed from the data in Table 2.1.3, the first substitution takes place relatively quickly for oxidation state Ru^{II}-Ru^{II}, with a corresponding half-life of 440 s for complex 19^{3+} and 21 s for complex 20^{3+}. While the rate of substitution for complex 20^{3+} is almost identical to the one obtained for complex 15^{3+}, the one obtained for complex 19^{3+} is more than one order of magnitude slower. Thus suggesting that electron donating substituents practically do not affect the first substitution process at oxidation state II,II whereas the electron withdrawing group sharply slows it down. Concerning the second substitution process, the rate constant for the non-symmetric complex 20^{3+} increases by 24 times with regard to the symmetric 15^{3+}.
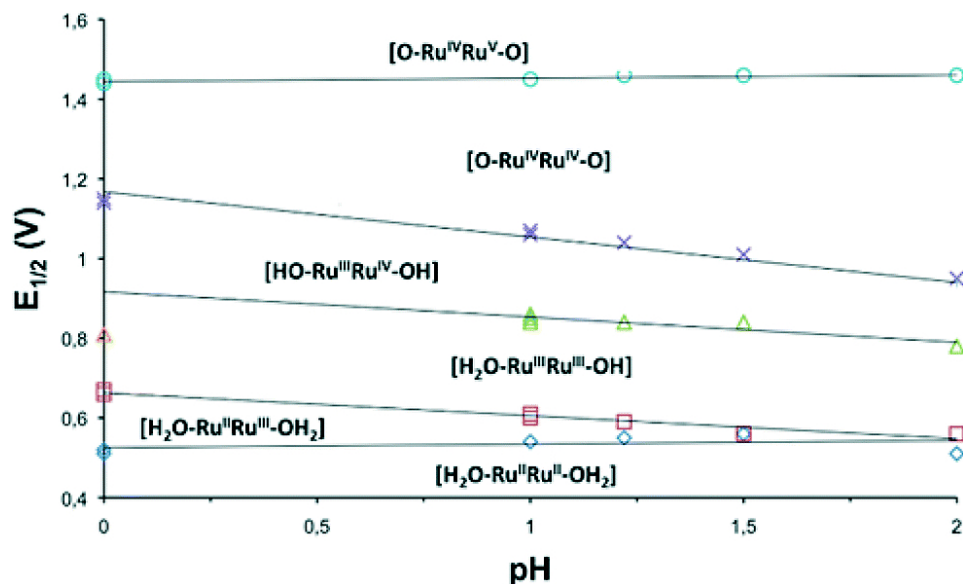
Figure 2.1.5: Pourbaix diagram in the pH range 0-2 for $\mathbf{20}^{3+}$ obtained from square wave voltammetry experiments. The dominant species at the different pH-E zones are indicated.

Water Oxidation Under Stoichiometric Conditions

Kinetic studies on the stepwise oxidation of [H_2O-Ru^{II}Ru^{II}-OH$_2$] to [O=Ru^{IV}Ru^{IV}=O] (see Equation 2.1.3) for complex $\mathbf{20}^{3+}$ were performed in order to determine the influence of the ED groups over the rate constants and were monitored using UV-vis spectroscopy. The same methodology was applied as to the one reported previously for complex $\mathbf{15}^{3+}$.[5,6] After addition of four equivalents of Ce(IV) to the catalyst, a series of kinetic events leads to the formation of molecular oxygen as shown in the upper part of Scheme 2.1.2. Since the system is catalytic, addition of more than four equivalents of Ce(IV) repeats the catalytic cycle. In order to isolate these kinetic events, the experiments at this point were performed up to a 1:4 ratio of complex $\mathbf{20}^{3+}$:Ce(IV). Figure

	First MeCN substitution		Second MeCN substitution	
Complex	$k_{S1}(s^{-1})$	$t_{1/2}(s)$	$k_{S2}(s^{-1})$	$t_{1/2}(s)$
$\mathbf{15}^{3+}$	4.0×10^{-2}	1.7×10^{1}	5.8×10^{-5}	1.2×10^{4}
$\mathbf{19}^{3+}$	1.5×10^{-3}	4.4×10^{2}	–	–
$\mathbf{20}^{3+}$	3.3×10^{-2}	2.1×10^{1}	1.4×10^{-3}	4.8×10^{3}

Table 2.1.3: Rate constants (k) and half-life ($t_{1/2}$) for the first and second substitution processes for dinuclear $Ru_2(H_2O)_2$-complexes measured in CF_3SO_3H (0.1 M) under pseudo-first order conditions ([MeCN/[dinuc] $\geq$ 10) at 25 °C

2.1.6 shows the change in absorption spectra together with the assigned species distribution and calculated absorption spectra (see also ESI). A summary of all the obtained ET- and reaction rate constants, together with the ones for complex $\mathbf{15}^{3+}$ are presented in Table 2.1.4.

	k		$k\mathbf{20}^{3+}$	$\Delta H^{\ddagger}$	$\Delta S^{\ddagger}$	$k\mathbf{15}^{3+\,a}$	$\Delta H^{\ddagger}$	$\Delta S^{\ddagger}$
k_{ETn}	k_{ET1}	Eqn (3a)	$(9.5 \pm 0.2) \times 10^{4}$	36 ± 4	-30 ± 8	8.6×10^{4}	22 ± 1	-84 ± 3
$(M^{-1}s^{-1})$	k_{ET2}	Eqn (3b)	$(6.5 \pm 0.3) \times 10^{4}$	25 ± 3	-70 ± 8	6.8×10^{4}	34 ± 2	-45 ± 7
	k_{ET3}	Eqn (3c)	$(3.9 \pm 0.4) \times 10^{4}$	20 ± 1	-90 ± 4	5.8×10^{4}	29 ± 2	-65 ± 5
	k_{ET4}	Eqn (3d)	$(1.5 \pm 0.1) \times 10^{3}$	21 ± 2	-150 ± 8	9.8×10^{2}	23 ± 3	-122 ± 10
$k(s^{-1})$	k_1	Scheme 2.1.2	$(6.7 \pm 0.1) \times 10^{-3}$	38 ± 5	-157 ± 16	1.7×10^{-3}	53 ± 3	-137 ± 9
	k_{O_2}	Scheme 2.1.2	$(1.5 \pm 0.1) \times 10^{-3}$	78 ± 6	-37 ± 20	5.5×10^{-4}	85 ± 8	-39 ± 27

Table 2.1.4: Rate constants calculated at 25.0 °C, together with the corresponding activation parameters calculated in the 10.0 °C to 40.0 °C range ($\Delta H^{\ddagger}$ in kJ mol^{-1}, $\Delta S^{\ddagger}$ in J mol^{-1} K^{-1}) for the reaction of complex $\mathbf{20}^{3+}$ and $\mathbf{15}^{3+}$ with Ce(IV) in 0.1 M CF_3SO_3H

^{a}Values obtained from ref.[5]

$$\text{H}_2\text{O-Ru}^{II}\text{Ru}^{II}\text{-OH}_2 - 1e^- \xrightarrow{k_{ET1}} \text{H}_2\text{O-Ru}^{III}\text{Ru}^{II}\text{-OH}_2 \qquad (2.1.3)$$

$$\text{H}_2\text{O-Ru}^{III}\text{Ru}^{II}\text{-OH}_2 - 1e^- \xrightarrow{k_{ET2}} \text{HO-Ru}^{III}\text{Ru}^{II}\text{-OH}_2 \qquad (2.1.4)$$

$$\text{HO-Ru}^{III}\text{Ru}^{III}\text{-OH}_2 - 1e^- \xrightarrow{k_{ET3}} \text{HO-Ru}^{IV}\text{Ru}^{III}\text{-OH} \qquad (2.1.5)$$

$$\text{HO-Ru}^{IV}\text{Ru}^{III}\text{-OH} - 1e^- \xrightarrow{k_{ET4}} \text{O=Ru}^{IV}\text{Ru}^{IV}\text{=O} \qquad (2.1.6)$$
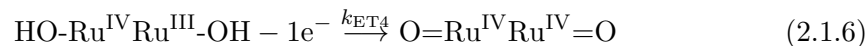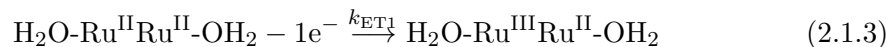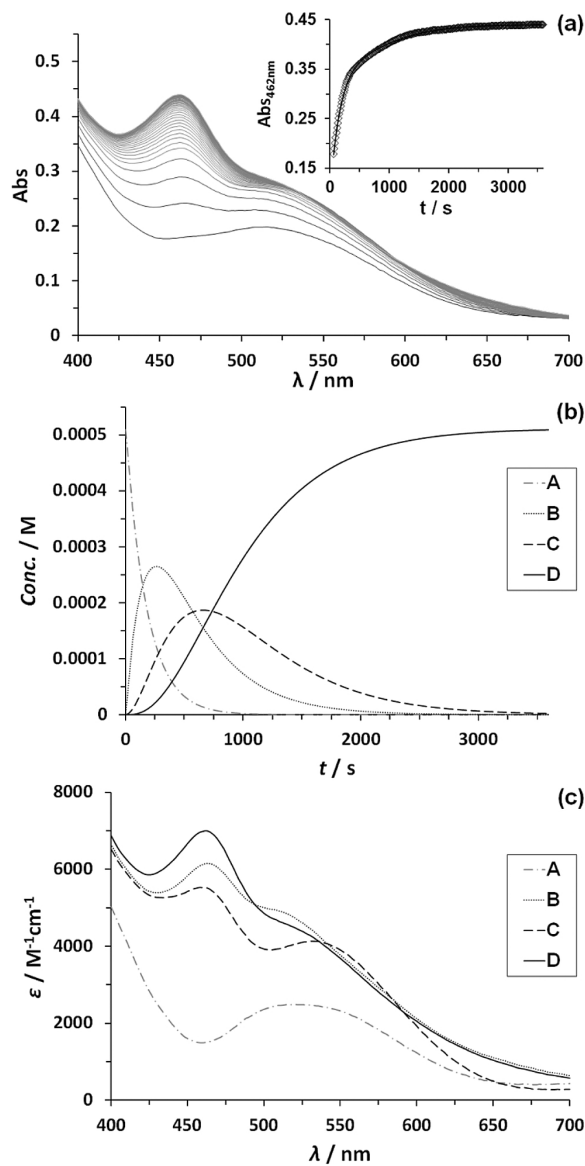
Figure 2.1.6: (a) Change of absorption spectra with time after addition of 4 eq. Ce(IV) to a 5.12×10^{-5} M solution of complex $\mathbf{20}^{3+}$ in CF_3SO_3H (0.1 M) at 25 ± 0.1 °C. Inset shows absorbance change over time at 462 nm (black diamonds) plus its mathematical fit for a reaction model of three consecutive first order reactions (black line). (b) Corresponding species distribution diagram as denoted in Scheme 2.1.2.[5,6] (c) Calculated spectra of participating species. Line code: dashed grey, species A; solid grey, species B; dashed black, species C; solid black, species D, as denoted in Scheme 2.1.2.[5,6]
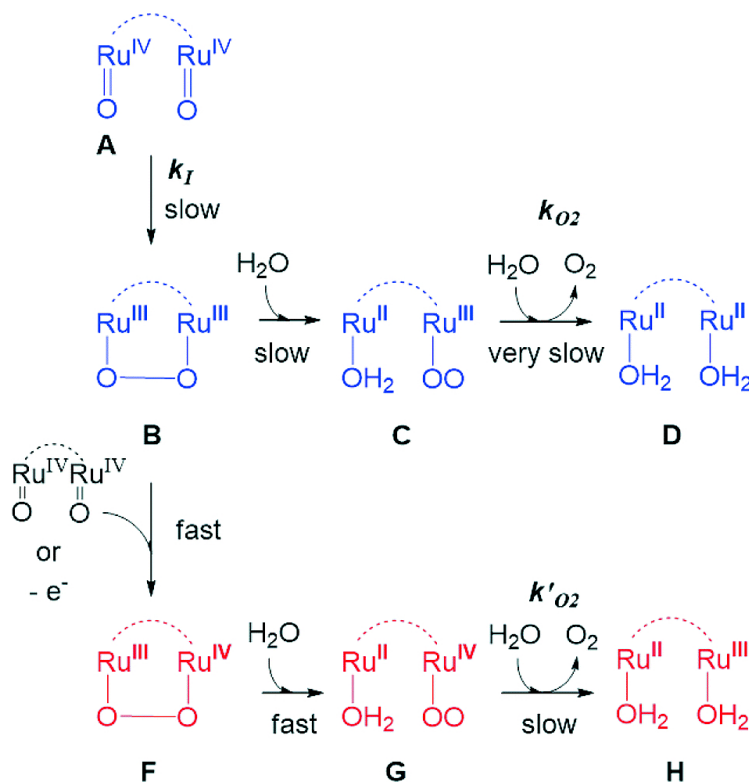
Scheme 2.1.2: Upper part (blue), simplified reaction scheme for oxygen evolution under stoichiometric conditions starting from species $[O=Ru^{IV}Ru^{IV}=O]$, A, through B, C and D. Lower part (red), additional pathways operating under excess Ce(IV) starting from B and involving species F, G and H.

From Table 2.1.4, it can be observed that all ET and reaction rates are larger for complex $\mathbf{20^{3+}}$ compared to $\mathbf{15^{3+}}$ which is attributed to the increase in thermodynamic driving force, since $\mathbf{20^{3+}}$ has lower redox potentials than $\mathbf{15^{3+}}$, and the same oxidant (Ce(IV)) is used. The following steps involve the O-O bond formation (A $\rightarrow$ B, in Scheme 2.1.2), the oxidation of the metal peroxide to superoxide (B $\rightarrow$ C) and finally the dioxygen ejection (C $\rightarrow$ D). For complex $\mathbf{20^{3+}}$ the rate determining step (k_{O_2}) is more than one order of magnitude faster than for complex $\mathbf{15^{3+}}$. This step involves the formal reduction of the complex from III,II to II,II and the substitution of the oxygen

species by water. The fact complex 20^{3+} with lower redox potentials has higher k_{O_2} values, points out that the main factor influencing this constant is the substitution process. This is in perfect agreement with the substitution trends described in the previous section, which highlights the influence of both electronic and symmetry effects (see also theory section later).

Interpretation of activation parameters is a complex issue when highly polar solvents and multiple oxidation states and electron transfer processes are involved in the TS or reaction intermediates. However, some conclusions can be drawn from the data obtained for complexes 20^{3+} and 15^{3+}. The high negative value for the activation entropy calculated for k_I is consistent with electrostriction dominating this step and agrees with the crucial role of water and hydrogen bonding in stabilizing intermediates or transition-state structures. Activation enthalpies for the k_{O_2} step are significantly larger compared to those of k_I. This can be seen as a consequence of breaking/forming more and/or stronger bonds to reach the final release of O_2 than to reach the intermediate step. It is also in agreement with the fact that the inductive effect exerted by the methoxy group in 20^{3+} is responsible for the slightly lower activation enthalpy compared to catalyst 15^{3+}.

Chemically and Photochemically Induced Catalytic Water Oxidation

In order to determine the influence of ED- or EW-substituents on the reactivity towards water oxidation, complexes 15^{3+}-21^{3+} were reacted with an excess of Ce(IV) in CF_3SO_3H (0.1 M) in a ratio 1:100 (1 mM Cat:100 mM Ce(IV)) (see Figure 2.1.7 and the ESI). Oxygen evolution was observed and quantified by manometric measurements and on-line mass-spectrometry. Molecular oxygen was identified as the only product for all dinuclear systems. Modest enhancement of oxygen evolution was observed for complex 20^{3+} compared to complex 15^{3+}, but a much slower rate was observed for complex

19^{3+} bearing the EW nitro-substituent on the bpp$^-$ ligand. The results obtained for **15**$^{3+}$, **19**$^{3+}$ and **20**$^{3+}$ are in agreement with the results found in the stoichiometric conditions. In addition, under excess of Ce(IV) additional pathways can exist involving the oxidation of the peroxo intermediate B to F, as shown in the lower part of Scheme 2.1.2. This will generate the III,II species (H) upon oxygen evolution, which would end up being the initial reactant species of the next catalytic cycle. As in the stoichiometric case the substitution factor at the rds seems to dominate the kinetic barriers, as will be discussed later on in the theory section.
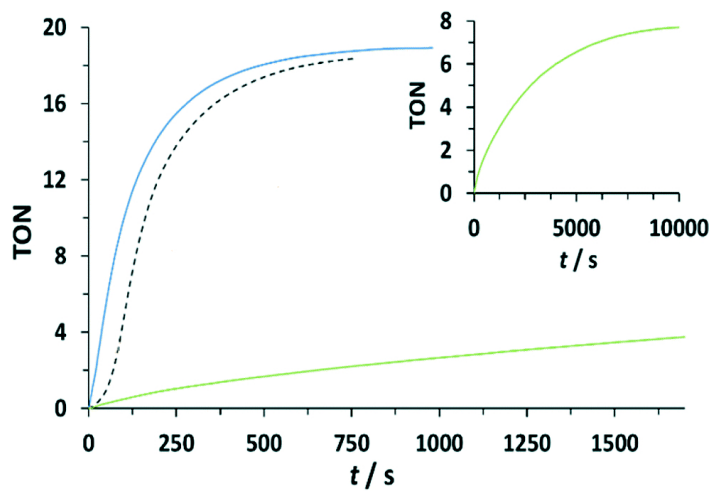
Figure 2.1.7: Catalytic activity of complexes **15**$^{3+}$, **19**$^{3+}$ and **20**$^{3+}$, followed by manometry. Reaction conditions: dinuc:Ce(IV) (1 mM:100 mM) in CF$_3$SO$_3$H (0.1 M). Line code: dashed black, **15**$^{3+}$; green, **19**$^{3+}$; blue **20**$^{3+}$. Inset shows full time span for complex **19**$^{3+}$.

An additional pathway for the water oxidation reaction involves the formation of the [O=Ru(V)Ru(IV)=O] species, as has been shown by CV for complex **20**$^{3+}$ which occurs at 1.40-1.45 V (Figure 2.1.4) with the onset of the wave at 1.30 V. In the case of Ce(IV) the redox potentials are not sufficiently high to enable this pathway ($E_{1/2}$ = 1.20 V at pH = 1; *vs.* SSCE) but oxidants with higher redox potentials such as

$[\mathrm{Ru(debpy)_2(bpy)}]^{2+}$ (debpy is diethyl-[2,2'-bipyridine]-4,4'-dicarboxylate) ($E_{1/2} = 1.38$ V $vs.$ SSCE))[50] could achieve it. For this reason light induced water oxidation was carried out using $[\mathrm{Ru(bpy)_3}]^{2+}$ ($E_{1/2} = 1.03$) and $[\mathrm{Ru(debpy)_2(bpy)}]^{2+}$ ($E_{1/2} = 1.38$ V) complexes as photosensitizers (PS) in combination with Co(III) as sacrificial electron acceptor (SEA) at pH = 7.0 using a phosphate buffer.[32,51,52] Water oxidation catalysts (WOCs) $\mathbf{20}^{3+}$ and $\mathbf{15}^{3+}$ were tested under these conditions using a Clark electrode to monitor the generation of oxygen over time and the results obtained are depicted in Figure 2.1.8.
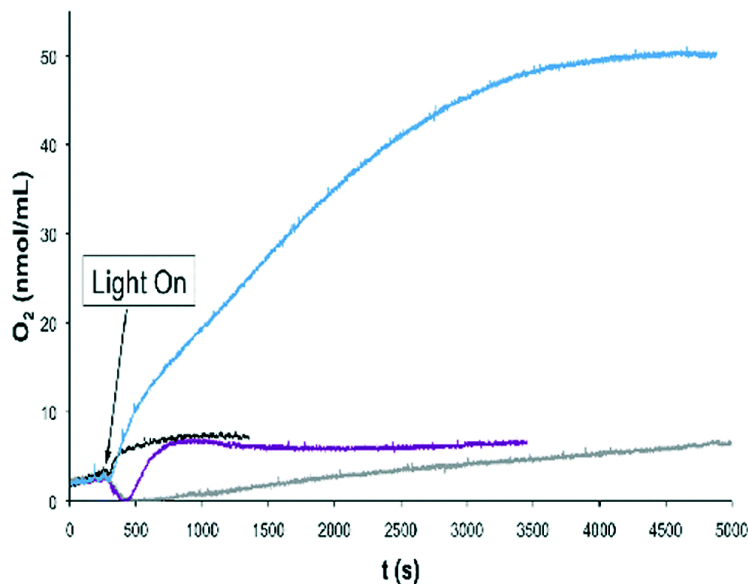
Figure 2.1.8: Oxygen evolution profiles of different catalysts at pH 7.0 in a phosphate buffer solution at 25.0 °C, upon irradiation with a 150 W xenon lamp with a 400 nm cut-off filter. Color code: $\mathbf{20}^{3+}$ and $[\mathrm{Ru(debpy)_2(bpy)}]^{2+}$, blue; $\mathbf{20}^{3+}$ and $[\mathrm{Ru(bpy)_3}]^{2+}$, violet; $\mathbf{15}^{3+}$ and $[\mathrm{Ru(debpy)_2(bpy)}]^{2+}$; black; $[\mathrm{Ru(debpy)_2(bpy)}]^{2+}$ alone gray. $[\mathrm{Co(OTf)(NH_3)_5}](\mathrm{OTf})_2$ was used as a sacrificial electron acceptor in all cases.

Several points can be deduced from the plot: a) the combination of $[\mathrm{Ru(bpy)_3}]^{2+}$ and $\mathbf{20}^{3+}$ generates a very small amount of oxygen, close to the amount generated by a blank

experiment with no catalyst; b) the combination of $\mathbf{20^{3+}}$ and the $[\mathrm{Ru(debpy)_2(bpy)}]^{2+}$ generates a much larger amount of oxygen. This indicates that $[\mathrm{Ru(debpy)_2(bpy)}]^{2+}$ is a sufficiently powerful oxidant to drive the oxygen evolution reaction while regular $[\mathrm{Ru(bpy)_3}]^{2+}$ is not. However, the amount of O_2 generated is relatively low, possibly due to the need for using an even stronger oxidant to perform this job and c) the $\mathbf{15^{3+}}$ catalyst that has slightly higher redox potentials than $\mathbf{20^{3+}}$ does not generate any oxygen at all with $[\mathrm{Ru(bpy)_3}]^{2+}$ but a small amount (again close to base line) was produced with the $[\mathrm{Ru(debpy)_2(bpy)}]^{2+}$. This highlights again the importance of properly matching the redox potentials of the PS and the catalyst in order to build successful systems for light induced water oxidation catalysis. Also note that the observed oxygen consumption at the initial stages of the reaction using $[\mathrm{Ru(bpy)_3}]^{2+}$ as PS and in the blank with $[\mathrm{Ru(debpy)_2(bpy)}]^{2+}$ is likely due to residual oxygen quenching by the $[\mathrm{Ru(bpy)_3}]^{2*}$ excited state as has been reported earlier.[53] Faster oxygen evolution processes such as the ones using $[\mathrm{Ru(debpy)_2(bpy)}]^{2+}$ and $\mathbf{15^{3+}}$ or $\mathbf{20^{3+}}$ preclude the observation of this phenomenon.

Water Oxidation Mechanisms

Density functional theory (DFT) calculations at the M06-L level of theory (see computational methods for details) were carried out in order to examine the water oxidation mechanisms and compare the energetics of the possible catalytic pathways of the parent and substituted Ru-Hbpp complexes. For a substituted complex containing an electron donating (ED) group, $\mathbf{20^{3+}}$ with a methoxy group at the central position of the trpy ligands was chosen while for the case of a complex with an electron withdrawing (EW) group, the analogue of $\mathbf{20^{3+}}$ containing a nitro group, $\{[\mathrm{Ru(NO_2\text{-}trpy)(H_2O)}][\mathrm{Ru(trpy)(H_2O)}](\mu\text{-bpp})\}^{3+}$, $\mathbf{22^{3+}}$ was used. $\mathbf{22^{3+}}$ has not been prepared in this work, but it is useful for direct comparative purposes to assess the effects of

varying substitution at a specific position.

As a first step, we explored both the water nucleophilic attack mechanism and intramolecular O-O bond formation pathways for $\mathbf{15}^{3+}$, starting from the common reactant [O=Ru(IV)Ru(IV)=O] in Figure 2.1.9. The free energy of activation ($\Delta G^{\ddagger}$) associated with the WNA is computed to be 39.0 kcal mol^{-1} in aqueous solution, which is much too high to be consistent with experimental kinetics. The WNA pathway is also not consistent with the available ^{18}O isotope labeling experiments, which demonstrate that the evolved O_2 originates from oxygen atoms of Ru-O units. The intramolecular direct coupling O-O bond formation between the two terminal oxo moieties features a $\Delta G^{\ddagger}$ of just 15.5 kcal mol^{-1} in aqueous solution (23.5 kcal mol^{-1} lower than in the WNA pathway). The optimized transition-state (TS) structure has an O-O distance of 1.71 Å and results in the formation of a μ-peroxo intermediate with O-O distance of 1.39 Å. Next, we considered the steps leading to O_2 evolution from the η^2-peroxo intermediate. The displacement of peroxo by water molecules to generate a η^1-superoxo intermediate and the consequent release of dioxygen are found to require high free energies of activation on the (IV,IV) potential energy surface ($\Delta G^{\ddagger} = 28.6$ and 40.6 kcal mol^{-1} respectively) (Figure 2.1.9). In earlier studies, the role of explicit water molecules in the first solvation shell in stabilizing intermediates or TS structures was investigated. For instance, introduction of an additional water molecule in the transition state structure for generation of the η^1-superoxo intermediate (TS-2) enables optimization of a hydrogen-bonding pattern compatible with the proton transfer to the departing peroxide oxygen. Inclusion of explicit water molecules in the models permits especially favorable microsolvation that is not accounted for in the continuum solvation model (at the cost of additional computational overhead associated with searching for, and averaging over, all possibly relevant microsolvated structures).
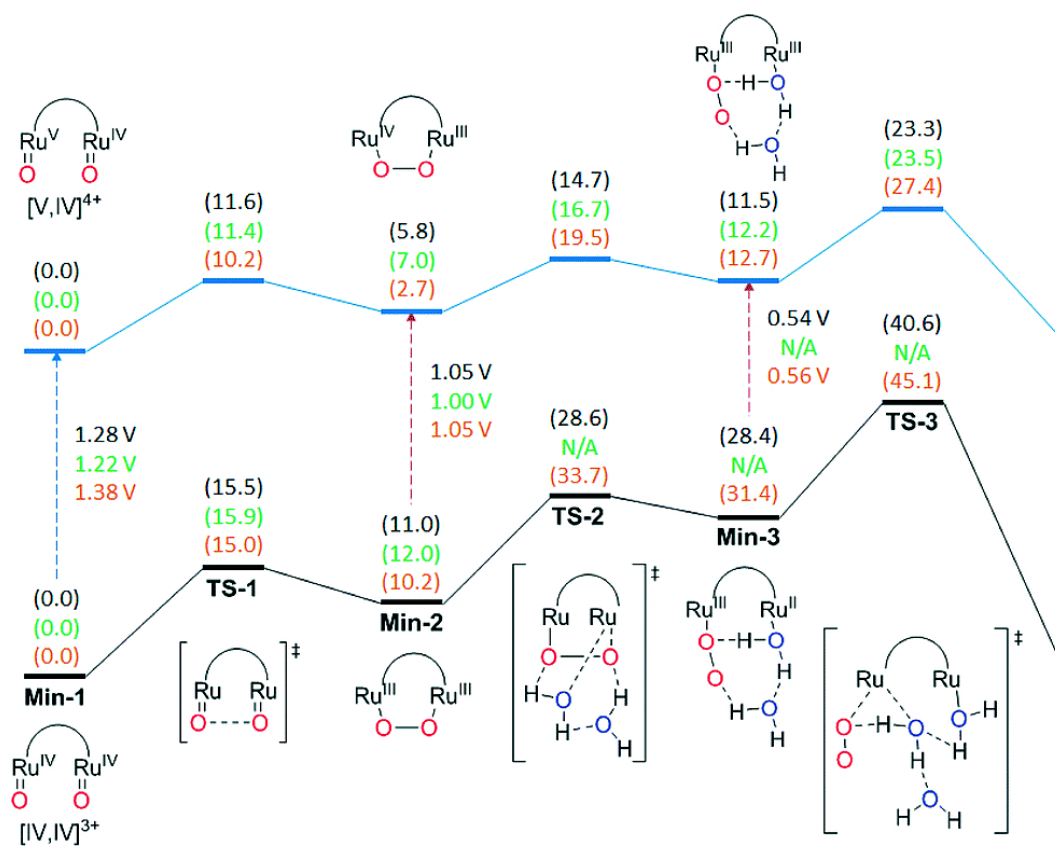
Figure 2.1.9: Previously reported free energies for stationary points relevant to water oxidation in complex 15^{3+} (black text, above) both in the $[IV,IV]^{+3}$ and the $[V,IV]^{+4}$ oxidation state, compared against those of complex 20^{3+} (green text, middle) and complex 22^{3+} (orange text, below). Redox potentials are reported *vs*. NHE.

Next, we investigated the remaining steps in water oxidation pathways for all complexes starting from the [O=Ru(IV)Ru(V)=O] intermediate obtained by one electron oxidization of [O=Ru(IV)Ru(IV)=O], for which the computed redox potential is 1.28 V vs. NHE (Figure 2.1.9). Similar to the [O=Ru(IV)Ru(IV)=O] case, intramolecular O-O bond formation is favored significantly over a WNA pathway for $\mathbf{15}^{3+}$ ($\Delta G^{\ddagger} =$ 11.6 and 27.4 kcal mol^{-1} respectively). Continuing from the mixed valence η^2-peroxo intermediate, the displacement of peroxo by a water molecule to yield the superoxo intermediate and subsequent O$_2$ evolution step was found to proceed with $\Delta G^{\ddagger}$ values of 14.7 and 23.3 kcal mol^{-1} respectively (Figure 2.1.9). It should be noted that in addition to one-electron oxidation of [O=Ru(IV)Ru(IV)=O], the one electron oxidized pathway can also be accessed by oxidation of the peroxide intermediate [Ru(III)(O-O)Ru(III)] to generate [Ru(IV)(O-O)Ru(III)], or oxidation of the superoxide intermediate [(OO-Ru(III)-Ru(II)(H$_2$O)] to generate [(OO-Ru(III)-Ru(III)(H$_2$O)] (Figure 2.1.9). In general for the complexes reported here, the potential at the foot of the catalytic wave for the V,IV/IV,IV redox couple is just at the edge of what may be reached by Ce(IV). However, once the [Ru(III)(O-O)Ru(III)] intermediate is generated then it can more readily access the one-electron-further oxidized pathway, and indeed even under conditions of limited stoichiometry of oxidant, disproportionation reactions may permit access to the most highly oxidized potential energy surface with its lower rate-determining free energy of activation. Direct oxidation of the [O=Ru(IV)Ru(IV)=O] intermediate can, of course, be accomplished either electrochemically or by using more powerful chemical oxidants. Thus, for the parent system $\mathbf{15}^{3+}$, intramolecular O-O bond formation is favored over a WNA mechanism and the rate-determining step is predicted to be the release of oxygen from the mixed valent peroxo intermediate with a free energy of activation of 23.3 kcal mol^{-1} on the potential energy surface for the most highly oxidized species.

Figure 2.1.9 also presents the energetics for the corresponding catalytic pathways involving the trpy-substituted Ru complexes $\mathbf{20}^{3+}$ (methoxy) and $\mathbf{22}^{3+}$ (nitro). For $\mathbf{20}^{3+}$ the free energy of activation of O_2 release is predicted to be very similar (within 0.2 kcal mol^{-1}) to that of unsubstituted $\mathbf{15}^{3+}$, in agreement with the very similar experimental rates obtained under catalytic conditions using Ce(IV) as oxidant. On the other hand, the use of electron withdrawing substituents as in the case of $\mathbf{22}^{3+}$ increases $\Delta G^{\ddagger}$ for this step by 4.1 kcal mol^{-1}, which is in agreement with the experimental observation that nitro-substituted $\mathbf{19}^{3+}$ has a much lower rate of reaction than $\mathbf{15}^{3+}$ or $\mathbf{20}^{3+}$ (see Figure 2.1.7), assuming inductive effects through the bpp ligand to be qualitatively similar to those through the trpy ligand. The fact that for $\mathbf{20}^{3+}$ the rds involves both substitution and reduction clearly indicates that in this case the substitution effect is the dominant factor.

2.1.3 Conclusions

We present a facile microwave based synthetic procedure to obtain symmetric and non-symmetric dinuclear ruthenium complexes, structurally based on the so called "Ru-bpp"-catalyst. The procedure presents an increase in overall yield in combination with a decrease of reaction time and workup steps. The electronic perturbation effects of different substituents on the ligand backbone on electronic transitions are examined and explained. Their effect on metal based redox potentials follows the expected trend of intrinsic electron donating and withdrawing properties. The position of the substituents on the ligand backbone has a major influence on the magnitude of these potentials. We have also analyzed the influence of the substitution kinetics as a function of ED and EW groups and found that while the former enhances substitution kinetics the latter drastically reduces them. This in turn seems to be the major effect for the rds of the water oxidation reactions under stoichiometric conditions analyzed for the case of $\mathbf{20}^{3+}$.

We have also shown that while complex $\mathbf{20}^{3+}$ is an active catalyst at oxidation state IV,IV as previously reported, it is a much better catalyst at the oxidation state IV,V, as shown by its large electrocatalytic wave. Further supporting this point, whilst the IV,IV oxidation state can be accessed with Ce(IV) oxidant, the IV,V can only be accessed electrochemically or with stronger oxidants such as $[Ru(debpy)_2(bpy)]^{2+}$. Indeed, efficient light induced water oxidation is obtained with the PS complex containing the debpy ligand while with regular $[Ru(bpy)_3]^{2+}$ is practically inactive. Finally, DFT calculations nicely complement the experimental results giving a consistent global description of the different reactions pathways that can operate in the water oxidation reactions catalyzed by the complexes described in this work.

2.1.4   Methods

Computational Methods

Density functional theory. Geometry optimizations were performed at M06-L[11] level of density functional theory using the Stuttgart [8s7p6d2f|6s5p3d2f] ECP28MWB contracted pseudopotential basis set[54] on Ru and the 6-31G(d) basis set[55] on all other atoms. Non-analytical integral evaluations made use of a pruned grid having 99 radial shells and 590 angular points per shell and an automatically generated density-fitting basis set was used within the resolution-of-the-identity approximation to speed the evaluation of Coulomb integrals as implemented in Gaussian '09 software package.[56] The nature of all stationary points was verified by analytic computation of vibrational frequencies, which were also used for the computation of zero-point vibrational energies, molecular partition functions (with all frequencies below 50 cm^{-1} replaced by 50 cm^{-1} when computing free energies), and for determining the reactants and products associated with each transition-state structure (by following the normal modes associated with imaginary frequencies). Partition functions were used in the computation of 298 K

thermal contributions to free energy employing the usual ideal-gas, rigid-rotator, harmonic oscillator approximation.[9] Free energy contributions were added to single-point M06-L electronic energies computed with the SDD basis set on ruthenium and the 6-311+G(2df,p) basis set on all other atoms to arrive at final, composite free energies.

Solvation and standard reduction potentials. Solvation effects associated with water as solvent were accounted for using the SMD continuum solvation model.[15] A 1 M standard state was used for all species in aqueous solution except for water itself, for which a 55.6 M standard state was employed. Thus, for all molecules but water, the free energy in aqueous solution is computed as the 1 atm gas-phase free energy, plus an adjustment for the 1 atm to 1 M standard-state concentration change of RTln(24.5), or 1.9 kcal mol^{-1}, plus the 1 M to 1 M transfer (solvation) free energy computed from the SMD model. In the case of water, the 1 atm gas-phase free energy is adjusted by the sum of a 1 atm to 55.6 M standard-state concentration change, or 4.3 kcal mol^{-1}, and the experimental 1 M to 1 M solvation free energy, -6.3 kcal mol^{-1}. The 1 M to 1 M solvation free energy of the proton was taken from experiment as -265.9 kcal mol^{-1}.[57–60]

Standard reduction potentials were calculated for various possible redox couples to assess the energetic accessibility of different intermediates at various oxidation states. For a redox reaction of the form

$$O_{(aq)} + ne^-_{(g)} \rightarrow R_{(aq)}$$
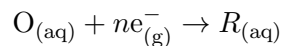
where O and R denote the oxidized and reduced states of the redox couple, respectively, and n is the number of electrons involved in redox reaction, the reduction potential $E^0_{O|R}$ relative to NHE was computed as

$$E^0_{O|R} = \frac{\Delta G^0_{O|R} - \Delta G^0_{NHE}}{nF}$$

where $\Delta G^0_{\text{O|R}}$ is the free energy change associated with the equation below (using Boltzmann statistics for the electron), ΔG^0_{NHE} is the free energy change associated with,

$$\text{H}^-_{(\text{aq})} + \text{e}^-_{(\text{g})} \rightarrow \frac{1}{2}\text{H}_{2(\text{g})}$$
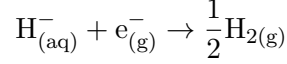
which is -4.28 eV with Boltzmann statistics for the electron,[59,61,62] and F is the Faraday constant.

Non-single-determinantal state energies. Several possible intermediates in the water oxidation mechanism have electronic structures that are not well described by a single determinant. In such instances, standard Kohn-Sham DFT is not directly applicable,[9,63,64] and we adopt the Yamaguchi broken-spin-symmetry (BS) procedure[65,66] to compute the energy of the spin-purified low-spin (LS) state

$$^{\text{LS}}E = \frac{^{\text{BS}}E\left(^{\text{HS}}\langle S^2 \rangle - ^{\text{LS}}\langle S^2 \rangle\right) - ^{\text{HS}}E\left(^{\text{BS}}\langle S^2 \rangle - ^{\text{LS}}\langle S^2 \rangle\right)}{^{\text{HS}}\langle S^2 \rangle - ^{\text{BS}}\langle S^2 \rangle}$$

where HS refers to the single-determinantal high-spin coupled state that is related to the low-spin state by spin flip(s) and $\langle S^2 \rangle$ is the expectation value of the total spin operator applied to the appropriate determinant. This broken-symmetry DFT approach has routinely proven effective for the prediction of state-energy splittings in metal coordination compounds.[64,67–70]

2.1.5 Acknowledgements

2.2 Mechanisms and Factors Controlling Photoisomerization Equilibria, Ligand Exchange, and Water Oxidation Catalysis Capabilities of Mononuclear Ruthenium(II) Complexes

2.2.1 Introduction

Polypyridyl ruthenium(II) complexes are well known to undergo photoluminescence,[71–73] photoredox,[74,75] photosubstitution,[76–78] and photoisomerization,[79–83] reactions, typically involving photoexcited triplet metal-to-ligand charge transfer (^{3}MLCT). We recently reported the irreversible and stoichiometric photoisomerization of *distal*-[Ru(tpy)(pynp)OH$_2$]$^{2+}$[a]   [tpy = 2,2';6',2"-terpyridine, pynp = 2-(2-pyridyl)-1,8-naphthyridine] to *proximal*-[Ru(tpy)(pynp)OH$_2$]$^{2+}$[17,81] (Scheme 2.2.1), which had not previously been characterized for polypyridyl ruthenium(II) aquo complexes. The photoisomerization of *cis*-[Ru(bpy)$_2$(OH$_2$)$_2$]$^{2+}$ (bpy = 2,2'-bipyridine) to the *trans* form – present as part of a photostationary state – in water was reported, but the *trans* form slowly reverts to the original *cis* form through a thermal reaction.[79] Polypyridyl ruthenium(II) aquo complexes have recently attracted much attention as active water oxidation catalysts; such catalysts are essential for devices designed to effect practical artificial photosynthesis.[16,31,33,49,84–89] Although water oxidation catalysts should be active in the context of photochemical systems (and ultimately in artificial photosynthesis), there are only a few reports of photochemical reactions of ruthenium(II) aquo complexes that are active for water oxidation catalysis.[81,82] Our recent report showed

---

[a]   The *proximal/distal* isomers were defined by the structural configuration between the naphthyridine moiety of pynp and the aquo ligand.

that the observed catalytic activity of *distal*-[Ru(tpy)(pynp)OH$_2$]$^{2+}$ for water oxidation significantly changes upon visible light irradiation, owing to photoisomerization to *proximal*-[Ru(tpy)(pynp)OH$_2$]$^{2+}$, in water; the catalytic activity of the *distal* isomer is higher than that of the *proximal* isomer by one order of magnitude.[17,81] The higher catalytic activity of *distal*-[Ru(tpy)(pynp)OH$_2$]$^{2+}$ was also confirmed in a subsequent report by Boyer *et al.*[89]
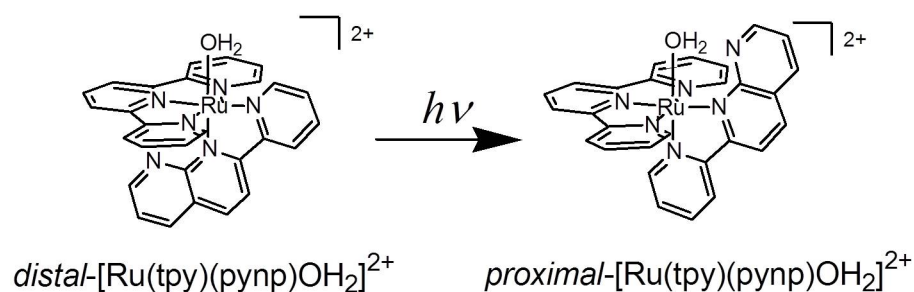
Scheme 2.2.1: Photoisomerization of *distal*-[Ru(tpy)(pynp)OH$_2$]$^{2+}$ to the *proximal* isomer.

Quantum chemical calculations undertaken to provide mechanistic insight into the photoisomerization of *distal*-[Ru(tpy)(pynp)OH$_2$]$^{2+}$ to *proximal*-[Ru(tpy)(pynp)OH$_2$]$^{2+}$ and into water oxidation catalysis by both isomers suggested that in the case of the photoisomerization, photodissociation of an aquo ligand on the *distal*-[Ru(tpy)(pynp)OH$_2$]$^{2+}$ occurs *via* the ^{3}MLCT state to give a pentacoordinate [Ru(tpy)(pynp)]$^{2+}$ intermediate.[17] We determined a pathway for conversion from this pentacoordinate [Ru(tpy)(pynp)]$^{2+}$ (*distal*-penta) intermediate [reflecting the structure (interatomic distances and angles) of the distal isomer] to a *proximal*-penta intermediate, reflecting the structure of the *proximal* isomer. Recoordination of a water molecule after this conversion produces the *proximal* isomer.[17]

The calculations also suggested that the photodissociation of an aquo ligand could be

suppressed by the intramolecular hydrogen bond (O-H$\cdots$N) between one hydrogen of an aquo ligand and an uncoordinated nitrogen of the naphthyridine moiety of pynp, thereby preventing the *proximal* isomer from undergoing a reverse photoisomerization to the *distal* isomer.[17,81] The quantum chemical calculations also provided an explanation for the different activity with respect to water oxidation catalysis between the *distal* and *proximal* isomers. The calculations showed that nucleophilic attack by water on distal-Ru(V)=O (the ruthenyl oxo species derived from *distal*-[Ru(tpy)(pynp)OH$_2$]$^{2+}$, calculated $\Delta G^{\ddagger}$ of 87.9kJmol^{-1} is favored over that on *proximal*-[Ru(tpy)(pynp)OH$_2$]$^{2+}$ (calculated $\Delta G^{\ddagger}$ of 104.6kJmol^{-1}) for O-O bond formation. Examination of the lowest unoccupied molecular orbitals in *distal*- and *proximal*-Ru(V)=O indicated that more orbital amplitude is concentrated on the Ru-O unit in the case of the *distal* isomer than in the case of the *proximal* isomer, in which some of the amplitude is instead delocalized over the pynp ligand, making the *proximal* isomer less electrophilic.

These experimental and theoretical results encouraged us to synthesize new derivatives – *distal*-/*proximal*-[Ru(tpy)(pyqu)OH$_2$]$^{2+}$ (*d*-/*p*-RuH$_2$O), with a 2-(2'-pyridyl)quinoline (pyqu) ligand instead of a pynp ligand – in order to clarify the influence of the interaction between the aquo ligand and the bidentate ancillary ligand on the photoisomerization and water oxidation catalysis. Here we report on the photoisomerization equilibrium between the *d*- and *p*-RuH$_2$O isomers and reveal the mechanisms and factors controlling the photoisomerization and water oxidation catalysis. The *distal*- and *proximal*-[Ru(tpy)(pyqu)Cl]$^{+}$ (*d*- and *p*-RuCl) isomers were isolated, as well as the *d*- and *p*-RuH$_2$O isomers, thus enabling comprehensive studies on the geometric structures, ligand exchange and redox reactions, and water oxidation catalysis of both isomers.

2.2.2   Results and Discussion

Synthesis of Ru Complexes

p-RuCl is predominantly formed, with respect to the *distal* isomer, in a thermal reaction between [Ru(tpy)Cl$_3$] and pyqu (49% yield), in contrast to the selective formation of *distal*-[Ru(tpy)(pynp)Cl]$^+$ by a similar thermal reaction between [Ru(tpy)Cl$_3$] and pynp.[17,81] The predominant formation of the p-RuCl isomer could be the result of more significant steric repulsion between the 8-proton on the quinoline moiety and the tpy ligand in the case of the *distal* isomer than between the 8-proton and the chloro ligand in the case of the *proximal* isomer, as seen in a similar ruthenium complex with a quinoline-2-carboxylate ligand.[90] The ^{1}H NMR spectrum of p-RuCl in CDCl$_3$ exhibited a doublet at $\delta = 10.35$ ppm (Figure S1A in the supporting information), which did not change for several days. However, these peaks assigned to p-RuCl were no longer observed immediately after p-RuCl was dissolved in D$_2$O; instead, a doublet at $\delta = 8.94$ ppm assigned to p-RuH$_2$O was observed. (Figure S2A in the supporting information). Thus, p-RuCl rapidly converts into p-RuH$_2$O by exchange of the chloro ligand with solvent water. d-[RuH$_2$O](PF$_6$)$_2$ was successfully isolated as a PF$_6$ salt by addition of NH$_4$PF$_6$ to the solution.

When p-RuD$_2$O in D$_2$O was irradiated with visible light, the peak area at $\delta = 8.94$ ppm in the ^{1}H NMR spectrum decreased, with an increase in that of a doublet at $\delta = 9.46$ ppm assigned to d-RuD$_2$O (Figure 2.2.1, left). The ^{1}H NMR spectral change was complete in 5 min, but the peak at $\delta = 8.94$ ppm did not disappear completely, suggesting that a photostationary equilibrium is reached in the photoisomerization of p-RuD$_2$O to d-RuD$_2$O in D$_2$O. The equilibrated concentration ratio of p-RuD$_2$O/d-RuD$_2$O was calculated to be 76:24 from the integrated peak areas at $\delta = 8.94$ and 9.46 ppm, respectively (Figure 2.2.1, right). The equilibrated solution was concentrated to

dryness, and the residual solid, redissolved in methanol containing 0.1 M NaCl, was subjected to gel permeation chromatography. In the chromatogram, two peaks were observed at 65 min and 44 min (Figure S5 in the supporting information). They showed an area ratio of 76:24, which is the same as the equilibrated concentration ratio of p-RuD$_2$O and d-RuD$_2$O in the photoisomerization reaction.[b]   The fractions at 65 min and 44 min were confirmed to be the corresponding p-RuCl and d-RuCl isomers by ESI-MS and ^{1}H NMR spectroscopic data (Figures S1 and S3 in the supporting information). This indicates that the aquo ligands on p-RuH$_2$O and d-RuH$_2$O were exchanged with chloride ions in solution to allow recovery of p-RuCl and d-RuCl stoichiometrically after removal of solvent.
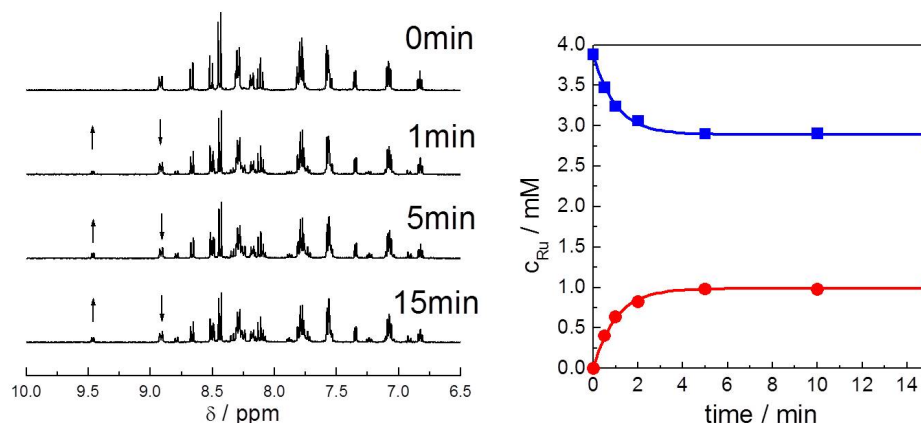
Figure 2.2.1: Left: ^{1}H NMR spectral change of p-RuD$_2$O (3.9 mM, pD = 8.4) during light irradiation ($\lambda > 420$ nm, 180 mWcm^{-2}) in D$_2$O at 298 K. Right: Kinetic profiles of p-RuD$_2$O ($\delta = 8.94$ ppm) (blue squares) and d-RuD$_2$O ($\delta = 9.46$ ppm) (red circles).

When d-RuCl was dissolved in D$_2$O, a peak area at $\delta = 9.90$ ppm for d-RuCl gradually decreased, together with an increase in a peak at $\delta = 9.46$ ppm assigned to d-RuD$_2$O

---

[b] The molar absorptivities of the complexes employed at the detection wavelength (500 nm) for the chromatogram are within $7.1\pm0.6\times10^3$M^{-1}cm^{-1} (see UV/visible absorption spectra in Figure 2.2.2).

(Figure S6 in the supporting information), showing that d-RuD$_2$O is stoichiometrically formed from d-RuCl by exchange of a chloro ligand with solvent water. The observed rate constant of aquation of d-RuCl to d-RuD$_2$O in D$_2$O was found to be 1.7×10^{-5}s^{-1} at 3.9 mM and 298 K (Figure S6 in the supporting information). The ligand exchange reactions and photoisomerization equilibrium of the p- and d-RuD$_2$O isomers are summarized in Scheme 2.2.2.
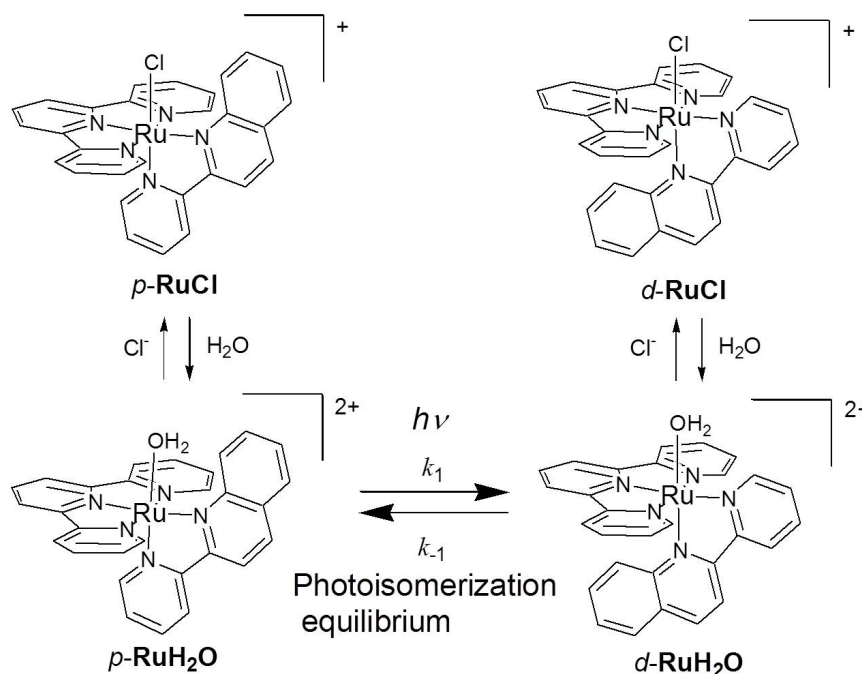
Scheme 2.2.2: Reaction schemes for ligand exchange and photoisomerization equilibria of p- and d-RuH$_2$O.

The UV/Vis absorption spectra of p-/d-RuCl and p-/d-RuH$_2$O isomers are shown in Figure 2.2.2, and the characters of the ^{3}MLCT absorption bands are summarized in Table 2.2.1, including those of $distal$-[Ru(tpy)(pynp)Cl]$^+$ and $proximal$-/$distal$-[Ru(tpy)(pynp)OH$_2$]$^{2+}$ isomers.[17,81] The p-/d-RuCl isomers exhibit maximum absorption wavelengths ($\lambda_{\max}$ = 527 and 526 nm) longer than those ($\lambda_{\max}$ = 502 and 501

nm) of the p-/d-RuH$_2$O isomers, due to a stronger ligand field of an aquo ligand relative to a chloro ligand. The absorption spectra of p-RuH$_2$O (λ_{max} = 502 nm) and d-RuH$_2$O (λ_{max} = 501 nm) are almost identical, indicating that the electronic structures of the isomer complexes are quite similar, as is also the case for *proximal-/distal-*[Ru(tpy)(pynp)OH$_2$]$^{2+}$ isomers. The λ_{max} values of p-/d-RuH$_2$O are shifted to blue relative to those of *distal-/proximal-*[Ru(tpy)(pynp)OH$_2$]$^{2+}$,[17,81] due to the destabilized $\pi \rightarrow \pi^*$ gap of pyqu relative to pynp.
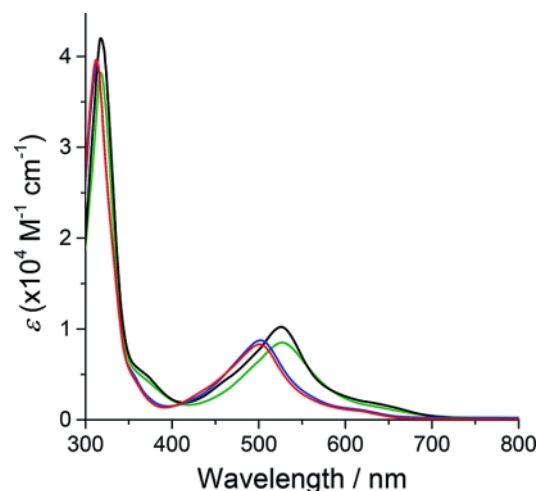
Figure 2.2.2: Absorption spectra of p-RuCl (green) and d-RuCl (black) in ethanol and of p-RuH$_2$O (blue) and d-RuH$_2$O (red) in water.

X-ray Crystallographic Analysis

ORTEP views of the isolated p-RuCl and p- and d-RuH$_2$O isomers are shown in Figure 2.2.3. The X-ray crystallographic data and selected interatomic distances and angles are shown in Tables S1 and S2, respectively, in the supporting information. The Ru1-N2 (center nitrogen of tpy) distances in p-RuCl and in the p- and d-RuH$_2$O isomers are *ca.* 0.1 Å shorter than the other Ru-N distances in the tpy ligand, similarly to the case

Complexes	Solvent	$\lambda_{\max}$ [nm]	ϵ $[10^3\mathrm{mol}^{-1}\mathrm{Lcm}^{-1}]$
p-RuCl	ethanol	527	8.5
d-RuCl	ethanol	526	10.2
p-RuH$_2$O	water	502	8.7
d-RuH$_2$O	water	501	8.3
$distal$-[Ru(tpy)(pynp)Cl]$^+$[81]	water	542[17,81]	8.6
$proximal$-[Ru(tpy)(pynp)OH$_2$]$^{2+}$[81]	water	527	9.3
$distal$-[Ru(tpy)(pynp)OH$_2$]$^{2+}$[81]	water	524	9.3

Table 2.2.1: Summary of maximum absorption wavelengths ($\lambda_{\max}$) and molar adsorption coefficients (ϵ) of ^{3}MLCT bands of p-/d-RuCl, p-/d-RuH$_2$O, $distal$-[Ru(tpy)(pynp)Cl]$^+$, and $proximal$-/$distal$-[Ru(tpy)(pynp)OH$_2$]$^{2+}$ isomers.

in [Ru(tpy)(bpy)Cl]$^+$ (bpy = 2,2'-bipyridine)[41,91,92] and [Ru(tpy)(bpy)OH$_2$]$^{2+}$ derivatives.[81,93–99] The Ru1-O1 distance [2.137(8) Å] in p-RuH$_2$O is close to that [2.132(5) Å] in d-RuH$_2$O. The distance between O1 and C28 in p-RuH$_2$O is 2.980 Å, suggesting an intramolecular hydrogen bond (O$\cdots$H-C) between the oxygen of an aquo ligand and H28 (on C28) at the 8-position of the quinoline moiety. Nevertheless, the O1-Ru1-N5 (a nitrogen of the quinoline moiety, being on a tpy plane) bond angle [105.1(3)°] in p-RuH$_2$O is larger (by 6.5-14.6°) than in any other reported ruthenium(II) aquo complex with a tridentate and a bidentate ligand,[81] owing to the steric repulsion between the aquo ligand and H28 on the quinoline moiety. Conversely, in d-RuH$_2$O the angle [105.0(2)°] along N2-Ru1-N5 (N2 is in the central pyridine of tpy; N5 is in the quinoline moiety, out of the tpy plane) is 4.8-9.9° wider than the corresponding angles in [Ru(tpy)(bpy)OH$_2$]$^{2+}$ derivatives, due to steric repulsion between H28 on the quinoline moiety and a tpy ligand.[81] In the case of p-RuCl, the Ru1-Cl1 length [2.464(2) Å] is slightly longer and the Cl1-Ru1-N5 (a nitrogen of the quinoline moiety, lying in the tpy plane) bond angle (105.20°) is larger than the corresponding vales in related mononuclear ruthenium complexes owing to the steric repulsion between Cl1 and H28.

This steric repulsion results in significantly larger Cl1-Ru1-N5-C29 (21.28°) and N4-C20-C21-N5 (8.77°) torsion angles for p-RuCl than for p-RuH$_2$O (corresponding angles O1-Ru1-N5-C29, 4.80° and N4-C20-C21-N5, 5.03°). This indicates that the steric repulsion between Cl1 and H28 in p-RuCl is more consequential than that between the aquo ligand and H28, owing not only to the larger size of the chloro ligand relative to the aquo ligand, but also to the intramolecular hydrogen bond (O$\cdots$H-C) between the aquo ligand and H28 in p-RuH$_2$O.

Aquation of p- and d-RuCl Isomers

The aquation rates of d-/p-RuCl were compared by a UV/Vis absorption spectroscopic technique (Figure S7 in the supporting information) because the aquation rate of p-RuCl is too fast to be measured with confidence by an NMR technique. The observed aquation rate constant of d-RuCl was $5.4 \times 10^{-5} \text{s}^{-1}$ (63 μM) at 298 K, which is consistent with the less certain observed rate constant ($1.7 \times 10^{-5} \text{s}^{-1}$, 3.9 mM) given by NMR measurements (Figure S6 in the supporting information). This value is comparable to that ($5.7 \times 10^{-5} \text{s}^{-1}$, 3.9 mM) of $distal$-[Ru(tpy)(pynp)Cl]$^{2+}$[17] and those ($3 \approx 10 \times 10^{-5} \text{s}^{-1}$) of reported chloro ruthenium complexes containing polypyridyl ligands.[100] The observed aquation rate constant of p-RuCl was $9.2 \times 10^{-2} \text{s}^{-1}$ (40 μM) at 298 K, 1700 times higher than that ($5.4 \times 10^{-5} \text{s}^{-1}$, 63 μM) of d-RuCl under similar conditions. The remarkably fast aquation of p-RuCl can be attributed to the enhanced steric repulsion between the chloro ligand and the quinoline moiety, as reported for the ruthenium complex with a dipyrazole ligand.[101]
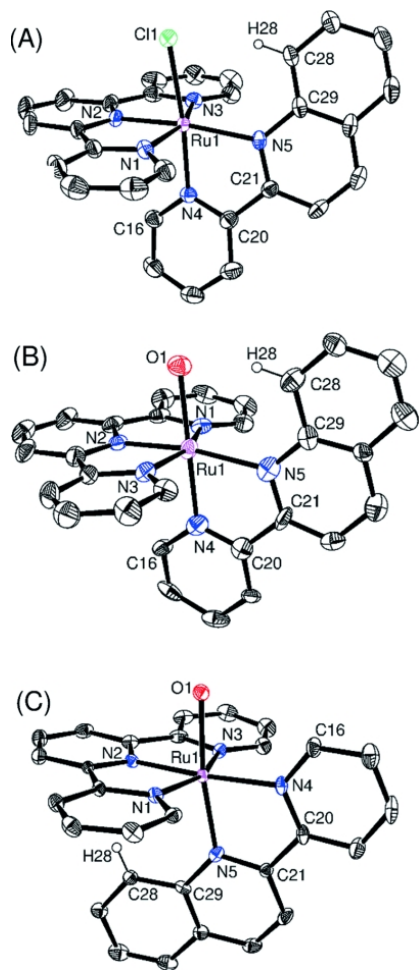
Figure 2.2.3: ORTEP views of (A) p-[RuCl](ClO$_4$), (B) p-[RuH$_2$O](ClO$_4$)$_2$, and (C) d-[RuH$_2$O](PF$_6$)$_2$ (30% probability). Counter anions and solvents are omitted for clarity.

Photoisomerization Equilibrium between p- and d-RuH$_2$O

The kinetic profiles of the photoisomerization of p-RuH$_2$O to d-RuH$_2$O in Figure 2.2.1 (right) were analyzed by use of a reversible reaction model (see the supporting information), and the best fit was obtained when the observed rate constants of the forward reaction [$proximal$ to $distal$, $(k_1)_{\text{obs}}$s^{-1}], the back reaction [distal to proximal, $(k_{-1})_{\text{obs}}$s^{-1}], and the observed equilibrium constant are taken to be $(k_1)_{\text{obs}}$ = 4.3±0.1×10^{-3}s^{-1}, $(k_{-1})_{\text{obs}}$ = 1.2±0.03×10^{-2}s^{-1}, and K_{obs} [= $(k_1)_{\text{obs}}/(k_{-1})_{\text{obs}}$] = 0.34±0.01 under the conditions employed. This establishes a photoisomerization equilibrium between p- and d-RuH$_2$O isomers (Scheme 2.2.2), in contrast to the previously reported $irreversible$ photoisomerization from $distal$-[Ru(tpy)(pynp)OH$_2$]$^{2+}$ to the proximal isomer (Scheme 2.2.1).[81] Both k_1 and k_{-1} increased linearly with the light intensity up to 180 mWcm^{-2} (Figure S8 in the supporting information). This result suggests that photoexcited states of the isomers are involved for both the forward and the back reactions. When the photoisomerization reaction was examined with d-RuH$_2$O instead of p-RuH$_2$O under the same conditions, nearly identical $(k_1)_{\text{obs}}$ (4.6±0.2×10^{-3}s^{-1}) and $(k_{-1})_{\text{obs}}$ (1.1±0.04×10^{-2}s^{-1}) values were obtained, showing that photoisomerization reactions of d-RuH$_2$O and p-RuH$_2$O are not influenced by the concentrations of each other under the conditions employed. The internal quantum yields for the forward and back photoisomerization reactions were assessed to be 0.34% and 1.1% (3.9 mM) from the experiment using monochromatic light (520 nm, 26.4 mWcm^{-2}; see the supporting information), the latter ($distal$ to $proximal$) being higher than that (0.31%) for the photoisomerization from $distal$-[Ru(tpy)(pynp)OH$_2$]$^{2+}$ to the proximal isomer at the same concentration.[c] The products and reaction aspects of the photoisomerization are the same as those involving the use of visible light (>420 nm), showing that

---

[c] The internal quantum yield was measured to be 1.5% at 92 m by a UV/Vis absorption technique in the earlier report.[81]

the possibility of reactions based on multiple transitions is excluded.

The photoisomerization reactions were examined under various pD conditions. (Figure 2.2.4). At pD < 8, $(k_1)_{\text{obs}}$ and $(k_{-1})_{\text{obs}}$ were independent of pD. With increasing pD, both $(k_1)_{\text{obs}}$ and $(k_{-1})_{\text{obs}}$ decreased, and any photoisomerization reaction did not proceed at all above pD = 12. We therefore conclude that both hydroxo isomers, p- and d-[Ru(tpy)(pyqu)OD]$^+$ (p- and d-RuOD), are inert for the forward and backward photoisomerization reactions, and that $(k_1)_{\text{obs}}$ and $(k_{-1})_{\text{obs}}$ are represented by Equations 2.2.1 and 2.2.2, respectively:

$$(k_1)_{\text{obs}} = k_1 \left[\frac{(p - \text{RuH}_2\text{O})}{(p - \text{RuH}_2\text{O}) + (p - \text{RuOH})} \right] \qquad (2.2.1)$$

$$(k_{-1})_{\text{obs}} = k_{-1} \left[\frac{(d - \text{RuH}_2\text{O})}{(d - \text{RuH}_2\text{O}) + (d - \text{RuOH})} \right] \qquad (2.2.2)$$

where k_1 (s^{-1}) and k$_{-1}$ (s^{-1}) are the rate constants$^{\text{d}}$ of the forward reaction (*proximal* to *distal*) and the back reaction (*distal* to *proximal*), respectively, and the square brackets represent concentrations of the indicated species. These are transformed into Equations 2.2.3 and 2.2.4, respectively, by means of a modified Henderson-Hasselbach equation:

$$(k_1)_{\text{obs}} = \frac{k_1}{1 + 10^{n'(\text{pD - p}K_{\text{a'}})}} \qquad (2.2.3)$$

$$(k_{-1})_{\text{obs}} = \frac{k_{-1}}{1 + 10^{n'(\text{pD - p}K_{\text{a'}})}} \qquad (2.2.4)$$

where n and pK_{a} are a Hill coefficient and acid dissociation constant of the aquo ligand of p-RuH$_2$O, respectively. The prime mark denotes those corresponding to d-RuH$_2$O in Equation 2.2.4. Equations 2.2.3 and 2.2.4 were applied to the experimental data used to obtain $(k_1)_{\text{obs}}$ and $(k_{-1})_{\text{obs}}$. The best fit was achieved with $k_1 = 4.3\pm0.3\times10^{-3}\text{s}^{-1}$, $n = 0.47\pm0.08$, and p$K_{\text{a}} = 10.5\pm0.2$ for $(k_1)_{\text{app}}$ data, and k$_{-1} = 1.3\pm0.1\times10^{-2}\text{s}^{-1}$, n' $= 0.66\pm0.09$, and p$K_{\text{a'}} = 9.8\pm0.1$ for $(k_{-1})_{\text{app}}$ data. Comparison between k_{-1} and k_1

$^{\text{d}}$ The k_1 and k_{-1} values are not real rate constants, but apparent ones, because they are dependent on the light intensity.

shows that the back reaction is 3.0 times faster than the forward reaction. The k_{-1} value
$(1.3 \times 10^{-2} \mathrm{s}^{-1})$ is 3.2 times higher than that $(4.1 \times 10^{-3} \mathrm{s}^{-1})$ for the photoisomerization of
$distal$-$[\mathrm{Ru(tpy)(pynp)OD_2}]^{2+}$ to the $proximal$ isomer under the same conditions, which
could be ascribable to the dominant steric repulsion between H28 on pyqu and the tpy
ligand for d-$\mathrm{RuD_2O}$, in comparison with that between the uncoordinated nitrogen in
the naphthyridine moiety of pynp and the tpy ligand for $distal$-$[\mathrm{Ru(tpy)(pynp)OD_2}]^{2+}$.
The $\mathrm{p}K_\mathrm{a}$ (10.5) and $\mathrm{p}K_\mathrm{a'}$ (9.8) values for the forward and back reactions are close to the
$\mathrm{p}K_\mathrm{a}$ values of p-$\mathrm{RuD_2O}$ ($\mathrm{p}K_\mathrm{a} = 10.5$) and d-$\mathrm{RuD_2O}$ ($\mathrm{p}K_\mathrm{a} = 9.4$) determined from the
^{1}H NMR chemical shifts of protons sensitive to ionization of the aquo ligands (Figure
S9 in the supporting information). This result indicates that both p- and d-RuOD
are inert to the photoisomerization, as is the case for $distal$-$[\mathrm{Ru(tpy)(pynp)OD_2}]^{2+}$ in
the earlier report.[81] The slight difference in $\mathrm{p}K_\mathrm{a}$ values (1.1) between p-and d-$\mathrm{RuD_2O}$
isomers results in a markedly pD-dependent K_obs value, as shown in the inset of Figure
2.2.4; K_obs increases above pH 9, reaching its maximum value ($K_\mathrm{obs} = 2.5$) at pH 12.
This is consistent with the observation that the yield of d-$\mathrm{RuD_2O}$ generated in the
photoisomerization increases from 26% to 65% on going from pH 5.7 to pH 12.

The temperature dependence of $(k_1)_\mathrm{obs}$ and $(k_{-1})_\mathrm{obs}$ provides 30.6±2.9 and
23.3±2.1kJmol^{-1} for the activation energies (E_a) of the forward and backward reac-
tions, respectively (Figure S10 in the supporting information). The higher E_a for the
forward reaction than for the backward reaction is attributed to the unfavorable loss of
the hydrogen bond (O$\cdots$H-C) between the oxygen atom of the aquo ligand and H28
of the pyqu ($vide\ supra$) upon loss of water. The van't Hoff plots for K_obs gave ΔH
$= 7.7 \pm 2.7 \mathrm{kJmol}^{-1}$ (Figure S10 in the supporting information), which is very close to
the hydrogen bond enthalpy (5.4kJmol^{-1}) of O$\cdots$H-C in the water-benzene complex.[102]
The fact that k_{-1} $(1.3 \times 10^{-2} \mathrm{s}^{-1})$ is higher than k_1 $(4.3 \times 10^{-3} \mathrm{s}^{-1})$ could be explained in
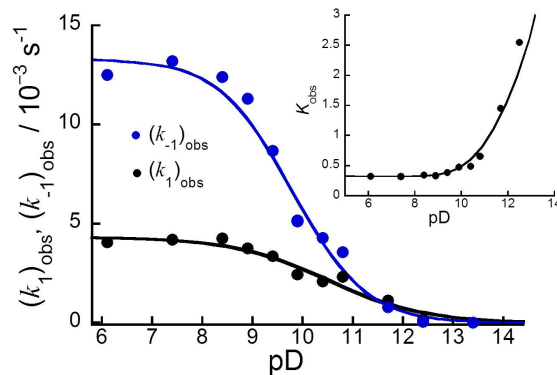
Figure 2.2.4: Plots of observed rate constants $[(k_1)_\text{obs}$ and $(k_{-1})_\text{obs}]$ *versus* pD for the photoisomerization reactions shown in Scheme 2.2.2. Visible light ($\lambda > 420$ nm, 180 mWcm^{-2}) was used to irradiate the p-RuD$_2$O solution (3.9 mM) in D$_2$O at 298 K. The solid lines show simulated curves based on Equations (2.2.3) and (2.2.4). Inset shows plots of observed equilibrium constants K_obs *versus* pD.

terms of a combination of the hydrogen bond (O$\cdots$H-C) enthalpy for p-RuD$_2$O (lowered k_1) and the dominant steric repulsion between the H28 on pyqu and the tpy plane for d-RuD$_2$O (enhanced k_{-1}). The van't Hoff plot shows that the photoisomerization of p-RuD$_2$O to d-RuD$_2$O proceeds endothermically, which is consistent with the yield (35%) of d-RuD$_2$O in the photoisomerization at 70 °C being higher than that (26%) at 25 °C under the neutral pD conditions.

Investigation of the Photoisomerization Equilibrium by DFT

DFT calculations were carried out by methods similar to those that we have previously reported for [Ru(tpy)(pynp)OH$_2$]$^{2+}$.[17] (see Computational Methods) Only M06//M06-L energies are discussed here, although M06-2X, B3LYP*, and M11-L energies are included in Figure S11 and S12 in the supporting information and are for the most part in qualitative agreement with those provided here.

Upon absorption of a photon, d-RuH$_2$O undergoes a transition to a singlet excited

state (Figure 2.2.5), followed by spin-orbit-facilitated intersystem crossing to the triplet surface. On the triplet surface, the ruthenium-aquo interaction becomes much less attractive, and release of bound water to form a pentacoordinate intermediate (d-Ru-penta) maintaining the otherwise octahedral structure of d-RuH$_2$O is less endergonic, by 36.1kJmol^{-1}, than the same process on the ground-state potential energy surface. This process could additionally involve some energy barrier associated with reorganization of the solvation shell, but we have not attempted to identify any sort of supermolecular transition state. d-Ru-penta then converts into p-Ru-penta (*i.e.*, a pentacoordinate intermediate reflecting the otherwise octahedral structure of p-RuH$_2$O). We calculated the energy of the relevant transition-state structures (TS-penta) on both the triplet and singlet surfaces. The activation energy for the transition (4.9 kJmol^{-1}) from d-Ru-penta to p-Ru-penta on the triplet surface is lowered by 50.2 kJmol^{-1} relative to that (55.1 kJmol^{-1}) on the singlet ground-state surface.

These energetics overall suggest that the conversion of d-Ru-penta into p-Ru-penta occurs predominantly on the triplet surface. The p-Ru-penta structure can then relax to its ground-state singlet analogue, coordination of a water molecule to which is thermodynamically favorable. The proximal-to-distal photoisomerization is predicted to occur in much the same way, with the minor difference that upon relaxation from the excited-state singlet to the triplet state, p-RuH$_2$O dissociates coordinated water through a barrierless process to become p-Ru-penta: that is, the triplet excited state of p-RuH$_2$O is predicted to be unstable as a hexacoordinate structure. This is consistent with the significant steric repulsion between the aquo ligand and H28 on the quinoline moiety, as indicated by X-ray crystallographic data for the ground-state species (Figure 2.2.3, Tables S1 and S2 in the supporting information). The lower barrier for conversion of p-Ru-penta into d-Ru-penta on the triplet surface (8.9 kJmol^{-1}) than on the singlet (net 113.0 kJmol^{-1}) suggests that the conversion of p-Ru-penta into d-Ru-penta also
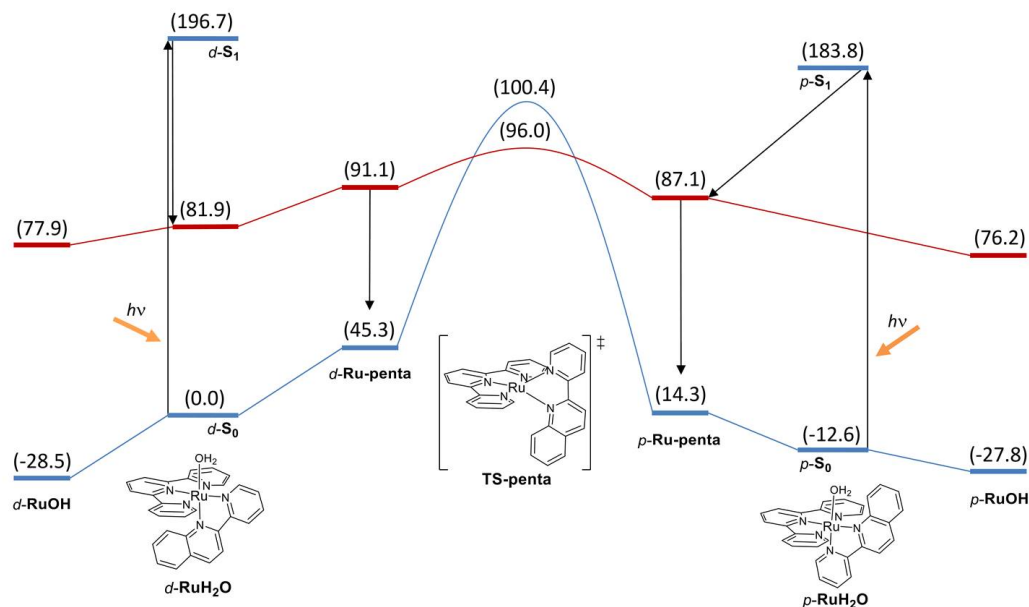
Figure 2.2.5: Plot of the energetics (M06//M06-L values in kJmol^{-1}, relative to d-RuH$_2$O at a pH of 14) for the proposed photoisomerization mechanism. Curves in blue represent singlet states, whereas curves in red represent triplets.

occurs for the former spin state. Finally, as determined from the experimentally derived van't Hoff plot, the isomerization of p-RuH$_2$O to d-RuH$_2$O is predicted to be endergonic on the ground-state surface.

However, in spite of the good performance of this level of theory for the ground-state singlet energetics, and the similarly good performance when compared with observed experimental behavior in the earlier pynp system,[17] there are some significant discrepancies that remain in the present case. Firstly, the predicted activation energies on the triplet surface here are considerably lower than those determined experimentally. Secondly, Figure 2.2.5 would predict that *proximal*-to-*distal* isomerization (again, on the triplet surface) should proceed more rapidly than *distal*-to-*proximal* isomerization, which again is contrary to observation. Possible explanations for this behavior include

(i) involvement of the counterion in the reaction coordinate, (ii) involvement of the local solvation shell in the reaction coordinate, and (iii) temperature-dependent changes in nonradiative relaxation rates from triplet intermediates to the ground-state singlet leading to a more complex kinetic model than that described above. We have not attempted to assess any of these, however, because the computational resources required ultimately to achieve such accurate agreement with experiment would be substantial with respect to any remaining insight gained.

DFT calculations were also undertaken to determine the energies of the singlet and triplet states of the deprotonated p- and d-RuOH isomers, as also shown in Figure 2.2.5. The energy differences between the p- and d-RuOH isomers are small: -0.6 and +1.6 kJmol^{-1} in the singlet and triplet states, respectively. We predict that all RuOH species will be thermodynamically favored at pH 14 relative to their RuH$_2$O and Ru-penta counterparts, which is consistent with the photoisomerization being increasingly quenched at high pH values.

Proton-Coupled Electron-Transfer (PCET) Reactions of p- and d-RuH$_2$O Isomers

The cyclic voltammogram (CV) of p-RuH$_2$O in aqueous solution at pH 6.9 exhibits a redox wave at 0.57 V (vs. SCE), which is pH-dependent over a wide range (pH = 2-13, Figure S13A in the supporting information) The Pourbaix diagram (Figure S14A in the supporting information) of p-RuH$_2$O suggests a one-step reaction consisting of a two-proton-coupled two-electron reaction of a Ru(II)-OH$_2$/Ru(IV)=O redox couple at pH = 2-10 (slope of 56 mV/pH), and a one-proton-coupled two-electron reaction of a Ru(II)-OH/Ru(IV)=O redox couple at pH = 10-13 (slope of 32 mV/pH). Under acidic conditions (below pH = 2), Ru(IV)=O is formed by a two-step reaction consisting of

a one-electron reaction of a Ru(II)OH$_2$/Ru(III)OH$_2$ redox couple and a two-proton-coupled one-electron reaction of a Ru(III)OH$_2$/Ru(IV)=O redox couple.

The CV of d-RuH$_2$O in an aqueous solution, however, exhibits two redox waves, at 0.49 V and 0.65 V (vs. SCE) at pH 6.6 (Figure S13B in the supporting information). These are also pH-dependent (slopes of 55 mV and 59 mV/pH, respectively), thus suggesting that a two-step reaction consisting of one-proton-coupled one-electron reactions of Ru(II)-OH$_2$/Ru(III)-OH and Ru(III)-OH/Ru(IV)=O redox couples occurs over a range of pH = 2-9 (Figure S14B in the supporting information), in contrast to the one-step reaction of the Ru(II)-OH$_2$/Ru(IV)=O redox couple for p-RuH$_2$O at the same pH region. An unfamiliar redox wave was observed at 0.70 V (vs. SCE) at pH 8.8 (Figure S13C in the supporting information), being pH-independent over the pH range 8-13 (Figure S14B in the supporting information). This redox response might be due to slow proton transfer in proton-coupled electron transfer of Ru(III)-OH/Ru(IV)=O couples, as reported in electrochemical reactions of [Ru(tpy)((4,4'-PO$_3$H$_2$)$_2$bpy)]$^{2+}$ (bpy = 2,2'-bipyridine) on ITO electrode.[103] We do not focus on the unfamiliar redox response in this report.

Water Oxidation Catalysis (WOC) by p- and d-RuH$_2$O Isomers

The catalytic activities of both p- and d-RuH$_2$O isomers with respect to water oxidation were examined with use of cerium(IV) ammonium nitrate as an oxidant, and the amounts of oxygen evolved were measured with a gas chromatograph. O$_2$ was evolved after p- or d-RuH2O was mixed with a Ce(IV) oxidant in water. The initial O$_2$ evolution rate increased linearly with the amount of p- or d-RuH$_2$O, and their turnover frequencies (TOFs) were determined from the slopes of the lines (Figure S15 in the supporting information). The TOF $(1.7\times10^{-3}s^{-1})$ of p-RuH$_2$O was 1.7 times higher than that $(1.0\times10^{-3}s^{-1})$ of d-RuH$_2$O, as summarized in Table 2.2.2. This result

is in contrast to the earlier $[\text{Ru(tpy)(pynp)OH}_2]^{2+}$ isomer system, in which the TOF of the distal isomer is higher than that of the proximal one by one order of magnitude.[81,89] The TOF value of p-RuH$_2$O is 3.5 times higher than that $(4.8{\times}10^{-4}\text{s}^{-1})$ of $proximal$-$[\text{Ru(tpy)(pynp)OH}_2]^{2+}$, though that of d-RuH$_2$O is 3.8 times lower than that $(3.8{\times}10^{-3}\text{s}^{-1})$ of $distal$-$[\text{Ru(tpy)(pynp)OH}_2]^{2+}$ under the same conditions.

Complexes	TOF[s^{-1}]	k_{rel} (expt.)	k_{rel} (theor.)^a
p-RuH$_2$O	1.7×10^{-3}	4	80
d-RuH$_2$O	1.0×10^{-3}	2	3×10^4
$proximal$-$[\text{Ru(tpy)(pynp)OH}_2]^{2+81}$	4.8×10^{-481}	1	1
$distal$-$[\text{Ru(tpy)(pynp)OH}_2]^{2+81}$	3.8×10^{-381}	8	800

Table 2.2.2: Summary of turnover frequencies (TOFs) of p-/d-RuH$_2$O and $proximal$-/$distal$-$[\text{Ru(tpy)(pynp)OH}_2]^{2+}$ isomers for water oxidation catalysis, and comparison of the relative rates of reaction between experimental [k_{rel} (exp.)] measurements and theory [k_{rel} (theor.)].

^{a}Theoretical values are based on $\Delta G^{\ddagger}$ values of water nucleophilic attack $\{87.9$ and 104.6 kJmol^{-1} were used for k_{rel} (theor.) of $distal$-$/proximal$-$[\text{Ru(tpy)(pynp)OH}_2]^{2+}\}$.[17]

Investigation of PCET and WOC Reactions Based on DFT Calculation

Energetics predicted from DFT calculations for the proposed mechanisms of PCET and WOC by d-/p-RuH$_2$O are shown in Figure 2.2.6, and the potentials (given at pH 0, relative to the NHE) and pK_a values are indicated in the corresponding steps. The proposed mechanism for water oxidation catalysis by both congeners is identical to that of $[\text{Ru(tpy)(pynp)OH}_2]^{2+}$, and begins with the transfer of two protons and two electrons from Ru(II)-OH$_2$ to generate the Ru(IV)=O state for both the $distal$ and the $proximal$ isomers. In d-RuH$_2$O this occurs through two consecutive PCET steps of Ru(II)-OH$_2$/Ru(III)-OH at 0.68 V and Ru(III)-OH/Ru(IV)=O at 0.94 V ($vs.$

NHE), which are then 0.29 and 0.55 V when adjusted to pH 6.6 (Table 2.2.3). In p-RuH$_2$O the potentials for the same two steps are 0.83 V and 0.91 V (*vs.* NHE), which become 0.42 and 0.50 V when adjusted to pH 6.9; these potentials are close enough possibly to lead to a two-electron CV wave depending on scan rate. The calculated potentials underestimate experiment by 100-200 mV, but are in good agreement with the observed isomeric trends (Table 2.2.3). DFT calculations predict pK_a values as indicated in Figure 2.2.6 and Table 2.2.3 and in general show good agreement with experiment, correctly predicting the greater acidity of the *distal* isomer, albeit somewhat overestimated.

Complexes	$E_{1/2}$ [V] vs. NHE				pK_a	
	Ru(II)-OH$_2$/		Ru(III)-OH/			
	Ru(III)-OH		Ru(IV)=O/			
	Exp.	Theor.	Exp.	Theor.	Exp.	Theor.^{a}
d-RuH$_2$O	0.49	0.29	0.65	0.55	9.4	10.6
(pH = 6.6)						
p-RuH$_2$O	0.57^b	0.42	0.57^b	0.50	10.5	13.0
(pH = 6.6)						

Table 2.2.3: Summary of $E_{1/2}$ and pK_a values of d-RuH$_2$O and p-RuH$_2$O.

^{a}The equivalent values implicit in the energetics in Figure 2.2.5 (computed with a somewhat smaller basis set to be consistent with the TD DFT calculations) are 9.0 and 11.3 for d-RuH$_2$O and p-RuH$_2$O, respectively.

^{b} The redox reaction was observed as a 2e$^-$/2H$^+$ process of Ru(II)-OH$_2$/Ru(IV)=O.

Oxidation from Ru(IV)=O to Ru(V)=O occurs at potentials of 1.56 and 1.50 V, respectively, for the *distal* and *proximal* isomers. Subsequently, concerted water nucleophilic attack (WNA) and proton loss occur, resulting in the conversion of the oxo ligands into hydroperoxo moieties. Superoxo species can form through either stepwise or concerted proton and electron transfer, and molecular oxygen can then be displaced by water to reform the starting compounds. As with [Ru(tpy)(pynp)OH$_2$]$^{2+}$, we predict WNA to be the rate-limiting step for water oxidation catalysis by
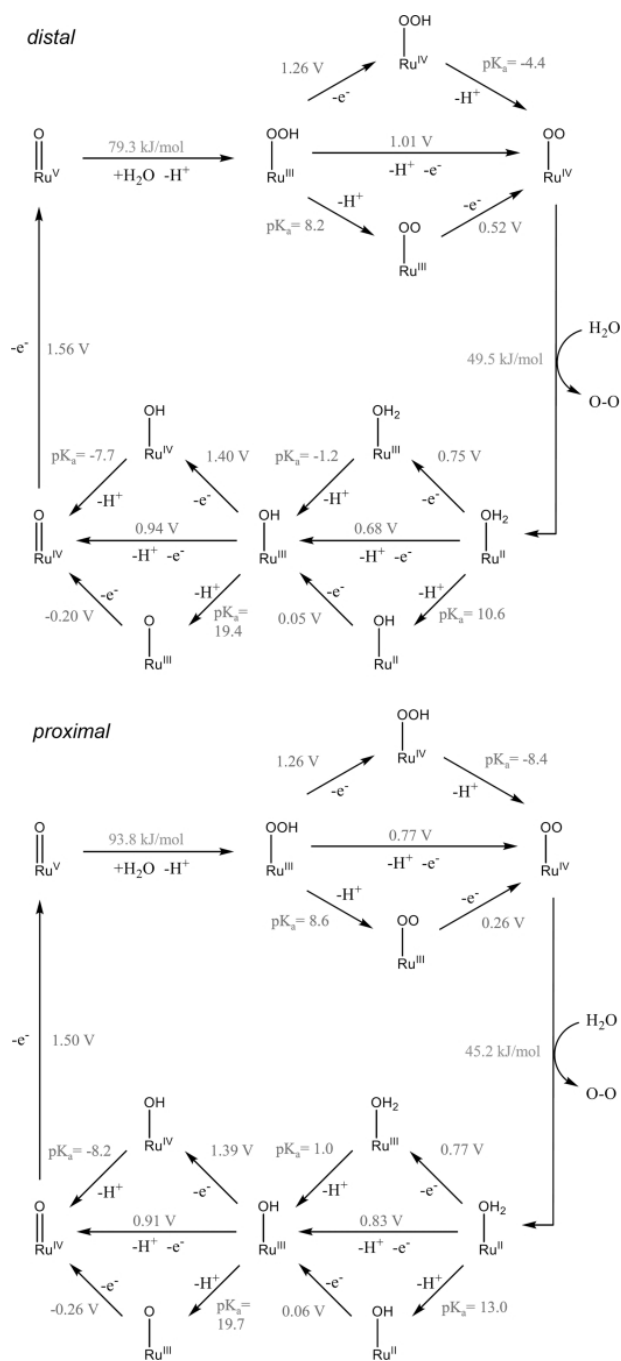
Figure 2.2.6: Plot of the energetics (M06-L//M06-L values) for the proposed water oxidation mechanisms of the *distal* and *proximal* isomers. Potentials are given at pH = 0, relative to the NHE.

$[Ru(tpy)(pyqu)OH_2]^{2+}$. Also as in the pynp case, the transition-state (TS) structures for the *distal* and *proximal* isomers required the inclusion of three and four explicit water molecules, respectively, to describe adequately the concomitant proton transfer (Figure 2.2.7). In d-RuH$_2$O, only one proton is transferred, whereas two proton transfers take place in the transition state for p-RuH$_2$O to generate the hydronium ion at the end of the water chain. The free energies ($\Delta G^{\ddagger}$) of activation for O-O formation by WNA on Ru(V)=O were calculated to be 79.3 and 93.8 kJmol^{-1} for the *distal* and *proximal* isomers, respectively. This is inconsistent with the experimentally observed higher TOF value of the *proximal* isomer in relation to the *distal* isomer. However, small variations in rate are very difficult to predict when the transition state includes such significant participation of the local solvent shell (Figure 2.2.7). A proper statistical mechanical average over the many TS structures potentially accessed with variations in the surrounding solvent shell would require demanding simulations that we have not attempted to undertake here.
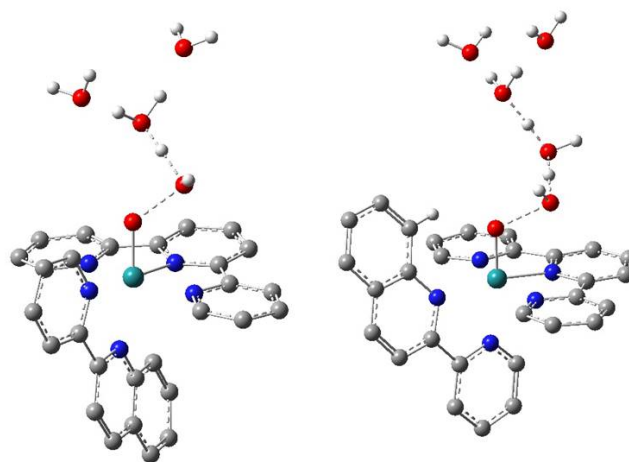
Figure 2.2.7: Pentamolecular *distal* (left) and hexamolecular *proximal* (right) M06-L-optimized WNA transition state structures. Ligand hydrogen atoms (aside from H28 on the *proximal* structure) are omitted for clarity.

Considering an orbital explanation for observed trends in reactivity, we note that for the pynp complex, the electron density of the LUMO of the Ru(V)=O species is delocalized onto the pynp ligand only in the case of the *proximal*-pynp complex, whereas it is delocalized on the quinoline moiety for both *d*- and *p*-RuH$_2$O (Figure 2.2.8). *distal*-[Ru(tpy)(pynp)OH$_2$]$^{2+}$, the TOF of which is the highest among these four complexes, does not show delocalization onto the pynp moiety. As discussed previously,[17] this delocalization leads to decreased orbital amplitude on the oxygen, which in turn increases the energy required for WNA and makes the ligand vulnerable to degradation. This offers insight into why *distal*-[Ru(tpy)(pynp)OH$_2$]$^{2+}$ is predicted and observed to catalyze water oxidation with the highest efficacy of the four complexes under scrutiny.

2.2.3   Conclusions

Photoisomerization between *d*- and *p*-RuH$_2$O is reversible, in contrast with the irreversible photoisomerization of *distal*-[Ru(tpy)(pynp)OH$_2$]$^{2+}$ to its *proximal* isomer. The kinetic analysis suggests a photoisomerization equilibrium between *d*- and *p*-RuH$_2$O, and the pD-dependent photoisomerization shows that both the hydroxo isomers – *proximal*- and *distal*-[Ru(tpy)(pyqu)OH]$^+$ – are inert to photoisomerization. The aquo ligand on *p*-RuH$_2$O is a hydrogen acceptor for the intramolecular hydrogen bond (O$\cdots$H-C) between the oxygen of the aquo ligand and H28 on the quinoline moiety, as suggested by the crystallographic structure of *p*-RuH$_2$O. In contrast, the aquo ligand in *proximal*-[Ru(tpy)(pynp)OH$_2$]$^{2+}$ is a hydrogen donor, and DFT calculations previously suggested that that situation in this last molecule could give a hydroxo-like ligand rather an aquo ligand, rendering it inert to photoisomerization.

Distortion with large angles for N5-Ru1-O1 (and -Cl1) is noteworthy for *p*-RuH$_2$O (and *p*-RuCl), due to steric repulsion between H28 on the quinoline moiety and the axial ligand. This could lead to the value of the observed aquation rate constant $(9.2 \times 10^{-2} \mathrm{s}^{-1}$

LUMO 1 (127 α)   LUMO 1 (126 β)

distal-[Ru^V(tpy)(pyqu)(O)]$^{3+}$

LUMO 1 (127 α)   LUMO 1 (126 β)

proximal-[Ru^V(tpy)(pyqu)(O)]$^{3+}$
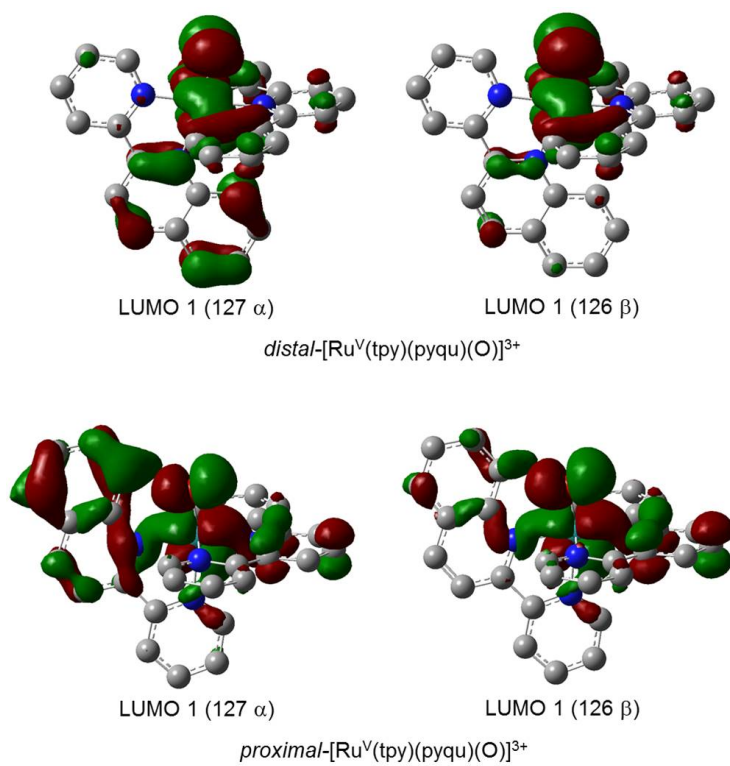
Figure 2.2.8: Lowest unoccupied molecular orbitals (LUMOs) of *distal-* and *proximal-* Ru(V)=O. Hydrogen atoms have been removed for clarity.

at 40 μM) of p-RuCl being 1700 times higher than that (5.4×10^{-5}s^{-1} at 63 μM) of

d-RuCl at 298 K. d-RuH$_2$O also showed an unusual distortion with a large angle of

N2-Ru1-N5, indicating that steric repulsion between H28 on the quinoline moiety and

the planar tpy system is significant for d-RuH$_2$O. This could explain the dominant

formation of p-RuCl in the reaction between [Ru(tpy)Cl$_3$] and pyqu, as well as faster

photoisomerization of d-RuH$_2$O than of $distal$-[Ru(tpy)(pynp)OH$_2$]$^{2+}$. The turnover

frequency (TOF $= 1.7\times10^{-3}$s^{-1}) of p-RuH$_2$O for catalytic water oxidation is 1.7 times

higher than that (1.0×10^{-3}s^{-1}) of d-RuH$_2$O. The influence of the ligand structure and

steric configuration of the complex on the catalytic activities should prove useful in the

design of efficient molecular catalysts for water oxidation.

2.2.4 Methods

Computational Methods

Density functional theory and TDDFT. All structures were optimized in the Gaussian '09 software package[56] at the M06-L level of theory,[11, 104, 105] with the 6-31G(d) basis set for non-metal atoms[55] and SDD-ECP28MWB [8s7p6d2f/6s5p3d2f] for Ru.[54] For numerical integrations, an ultrafine grid was used. A resolution of the identity procedure was employed, utilizing a fitting basis set automatically generated by the software. Frequency calculations were performed at the same level of theory in order to verify the nature of each stationary point and to obtain thermal contributions to the free energy of each structure. Because low frequency modes tend to be poorly described under the ideal-gas, rigid-rotator, harmonic-oscillator approximation, thermal contributions from frequencies below 50 cm^{-1} were replaced in each case with those predicted for a frequency of 50 cm^{-1}. For photoisomerization reactions, single-point calculations were performed by use of the M06, M06-2X, M11-L, and B3LYP* (* $= 15\%$ Hartree-Fock exchange) functionals,[95, 106, 107] with the 6-311+G(d) basis set for non-metal atoms[96] and

SDD for Ru. For water oxidation mechanisms, single-point calculations were performed by use of the M06-L and B3LYP* functionals with the 6-311+G(2df,p) basis set for non-metal atoms[96] and the SDD basis set for Ru. Time-dependent density-functional theory (TDDFT) calculations were also performed in Gaussian '09 to compute energies for electronic excited states. As in the single-point calculations for the photoisomerization reactions, the 6-311+G(d) basis set was used for non-metal atoms and SDD for Ru. The SMD continuum aqueous solvation model[15] was also employed for ground- and excited-state calculations, the latter with employment of a linear response formalism in conjunction with TD DFT.

Solvation, Standard Reduction Potentials, and Spin Purification. All single-point calculations, in addition to using the SMD continuum water model, also included a standard-state correction to 1 M concentrations for all species except water. For water, a standard-state adjustment from 1 atm to 55.6 M was used, as well as the experimentally determined 1 M to 1 M self-solvation free energy (-26 kJmol^{-1}). The proton gas-phase and solvation free energies were taken from experiment as -26 and -1113 kJmol^{-1}, respectively.[57–60] Redox potentials were calculated *versus* the standard hydrogen electrode (taken to have an absolute potential of 4.28 V). For geometries with multi-determinantal electronic structures, the Yamaguchi spin-purification procedure was employed to obtain the energies of low-spin states from spin-contaminated single-determinantal self-consistent-field solutions.[65, 66]

2.2.5   Acknowledgments

Chapter 3

Supramolecular Cages as a Source of Enzyme-Mimetic Shape Recognition

3.1 Empirical and Theoretical Insights into the Structural Features and Host-Guest Chemistry of M_8L_4 Tube Architectures

3.1.1 Introduction

Metal-organic container molecules[19, 21, 108–112] have attracted interest due to their ability to isolate guest molecules in the microenvironments provided by their internal cavities. Encapsulation may alter the chemical behavior of a guest,[113] leading to applications in catalysis,[114–119] sensing,[120–125] stabilization,[126–130] and transport.[131–134] Subcomponent self-assembly, wherein dynamic-covalent $C=N$[135, 136] and coordinative $M \rightarrow L$ bonds are formed during the same overall process,[137–140] has proven particularly useful for the synthesis of metal-organic hosts.[141] The first such hosts had tetrahedral[1, 142–145] or cubic[2, 146–149] structures, with approximately spherical cavities suitable for binding compact anions and small molecules.

Newer subcomponent-self-assembled hosts have been prepared that have yet more complex structures, including pseudoicosahedra,[150] hexagonal[151, 152] and pentagonal[3] prisms, twisted cubes,[153] asymmetric structures,[154] and tubular architectures.[155] Tubes represent interesting research targets due to their potential biomimetic function as molecular channels for selective transportation of ions and molecules, and as hosts for linear guests. Although many tubular organic systems have been reported,[156–161] the structural properties and host-guest chemistries of discrete metal-organic tubes have been less well-studied.[162, 163]

Recently, we have reported the assembly of M_8L_4 tubular capsule **1a** from the reaction of tetraamine **A**, 6-methyl-2-formylpyridine **1** and $[Cu(MeCN)_4]BF_4$ (Scheme

3.1.1).[155] This tube is able to transform $Au(CN)_2^-$ into a linear complex anion NC-Au-CN-Cu-NC-Au-CN$^-$, which was not independently observed, as the optimal guest for encapsulation. Building upon our previous work on tube **1a**, we demonstrate how the length, shape and substituents of the ligands, the counteranions and metals can influence the stereochemistry and host-guest chemistry of the tubular complexes. Insights into the nature and origin of some of these processes are provided by density functional theory (DFT) analysis.

3.1.2 Results and Discussion

Synthesis and Stereochemistry

A M_8L_4 tubular complex can be constructed as the uniquely observed product using elongated tetraamine **A**, **B**, or **C** (4 equiv), 2-pyridine-carboxaldehyde derivatives (16 equiv), and a suitable salt of Cu(I) or Ag(I) (8 equiv) in acetonitrile, as depicted in Scheme 3.1.1. Depending on the orientation of the bidentate iminopyridine binding sites, the M_8L_4 tube can adopt approximate $D_{2d}(/D_2)$ or D_4 point symmetries where the metal ions define the vertices of a cuboid. As we observed earlier,[155] in the crystal structures of tube **1a**·BF$_4$, the D_{2d} isomer has isosceles trapezoids as the long faces of the cuboid, with the shorter faces forming rectangles, whereas in the D_4 isomer the cuboid approximates a right square prism in which one of the square faces is twisted with respect to the other. The D_4 isomer possesses a narrow linear channel that is capable of trapping two acetonitrile molecules inside. The difference in the symmetry of the two diastereomers led to characteristic NMR peak multiplicities, allowing them to be distinguished by ^{1}H NMR. The population of the two isomers in solution reflects their relative thermodynamic stability, which can be tuned in several ways, as summarized in Table 3.1.1.
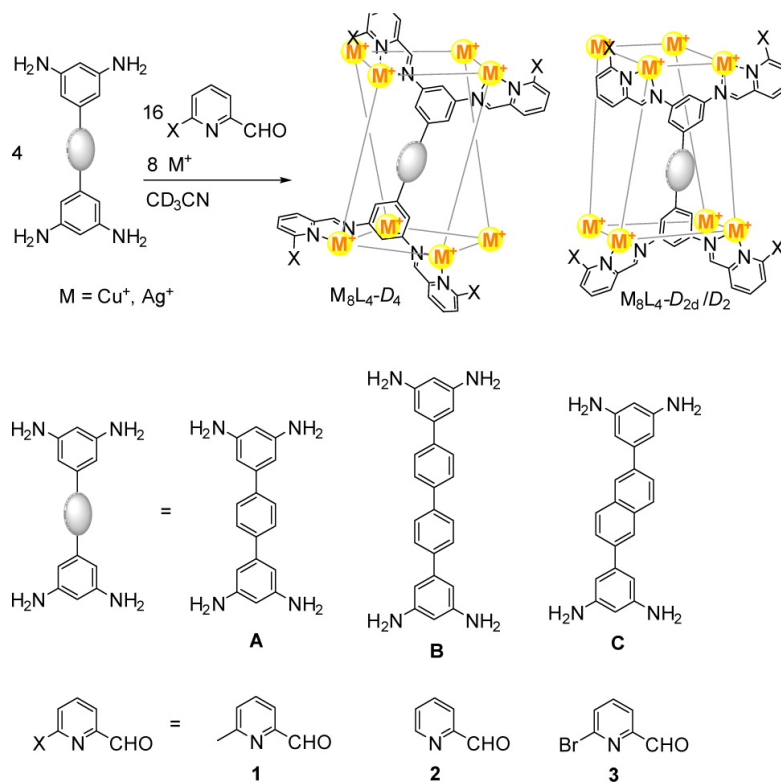
Scheme 3.1.1: General synthesis of M_8L_4 tubes

The substituent on the aldehyde subcomponent was observed to influence the stability of the tube isomers. Replacing a methyl group with a proton (aldehyde **2**) or a bromine (aldehyde **3**) at the 6 position of pyridine-2-carboxaldehyde resulted in the relative destabilization of the D_4-symmetric isomer, so that in the cases of **2a**·BF$_4$, **3a**, and **1c**·BF$_4$, the D_4 isomer did not form in solution.

In most cases, both BF_4^- and PF_6^- counterions allow the formation of M_8L_4 tubes, and the formation of the D_4 isomer is preferred when PF_6^- is present. The crystal structure of **2a**-D_4·PF$_6$ (Figure 3.1.1) reveals that one PF_6^- anion is located at each end of the tube with one fluorine atom pointing directly into the channel, and four such anions associate at the junctions between two neighboring terphenyl ligands, which are

| complex | tetraamine | aldehyde | counter ion | |
			BF_4^-	PF_6^-
1a	**A**	**1**	$D_4{:}D_{2d}$ 90 : 10%	D_4 only
2a	**A**	**2**	D_{2d} only	$D_4{:}D_{2d}$ 52 : 48%
3a	**A**	**3**	D_{2d} only	unstable
1b	**B**	**1**	$D_4{:}D_{2d}$ 1 : 99%	$D_4{:}D_{2d}$ 24 : 76%
1c	**C**	**1**	D_2 only	$D_4{:}D_2$ 6 : 94%

Table 3.1.1: Summary of isomers formed in acetonitrile upon the variation of tetraamine, aldehyde, and counter ion for Cu_8L_4 tubes

also sandwiched between two pyridine residues. For all these anions, short contacts (2.3-2.8 Å) are observed between fluorine atoms and protons of the complex, which may account for the extra stabilization effect brought by the PF_6^- anion.[164, 165]

Host **2a**·PF_6 has an approximately equal distribution of both isomers in solution. The interconversion between **2a**-D_4·PF_6 and **2a**-D_{2d}·PF_6 could be followed by ^{1}H NMR spectroscopy as the temperature was varied. Kinetic studies (described in the supporting information) revealed $\Delta H^{\ddagger} = 108 \pm 7$ kJ mol^{-1} and $\Delta S^{\ddagger} = 71 \pm 24$ J K^{-1} mol^{-1} for the isomerization from **2a**-D_4·PF_6 to **2a**-D_{2d}·PF_6, and $\Delta H^{\ddagger} = 58 \pm 8$ kJ mol^{-1}, and $\Delta S^{\ddagger} = -104 \pm 24$ J K^{-1} mol^{-1} for the reverse transformation (from **2a**-D_{2d}·PF_6 to **2a**-D_4·PF_6), which appears more entropically disfavored compared to the same process for the terphenyl congener **1a**·BF_4 ($\Delta S = -62 \pm 21$ J K^{-1} mol^{-1}).[155] The rate constants for both transformations were identical at 283 K, marking **2a**-D_4 as the dominant species in solution below this temperature, and **2a**-D_{2d} above.

Since the choice of counterions has been shown to have a measurable but small impact on the stereochemistry of almost all of the complexes listed in Table 3.1.1, a computational study was undertaken to determine the differential effect of including two PF_6^- counterions at the ends of the empty D_4 *versus* the D_{2d} isomers of **1a**. A relative stabilization of the D_{2d} isomer by only 4.1 kJ mol^{-1} was computed (see Computational
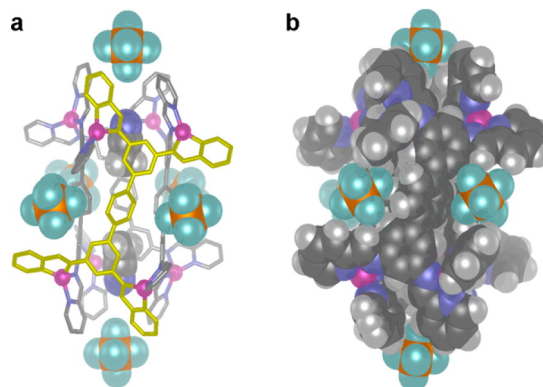
Figure 3.1.1: Crystal structure of **2a**-D_4·PF$_6$. (a) Representation of the complex with one ligand highlighted in yellow (hydrogen atoms not shown). (b) CPK representation showing the proximity between PF$_6^-$ anions and ligand hydrogens.

Methods section for theory details), a value commensurate with the small energy changes associated with the variations in isomeric ratios discussed above.

Longer ligands also disfavored the D_4 isomer: the reaction between tetraamine **B** or **C**, 6-methyl-2-pyridine-carboxaldehyde **1** and [Cu(MeCN)$_4$]BF$_4$ in acetonitrile produced **1b**-D_{2d} and **1c**-D_2 as the predominant isomers, respectively (Figures S27 and S33, supporting information). The hexafluorophosphate anion was again found to slightly stabilize the D_4 isomer; when copper(I) hexafluorophosphate was used in place of the tetrafluoroborate, the equilibrium ratios were found to be 24:76% and 6:94% for complexes **1b**-D_4:**1b**-D_{2d} and **1c**-D_4:**1c**-D_2, respectively, as revealed by their ^{1}H NMR spectra (Figures S21 and S30, supporting information). Models suggested that the D_4-symmetric tubes constructed from tetraamine **B** or **C** are not long enough to accommodate a third acetonitrile molecule inside the channel, leaving instead additional empty space, and incurring an energetic penalty for doing so. Single crystals of **1b**·BF$_4$ and **1c**·PF$_6$ were isolated by vapor diffusion of diethyl ether (or diisopropyl ether) into
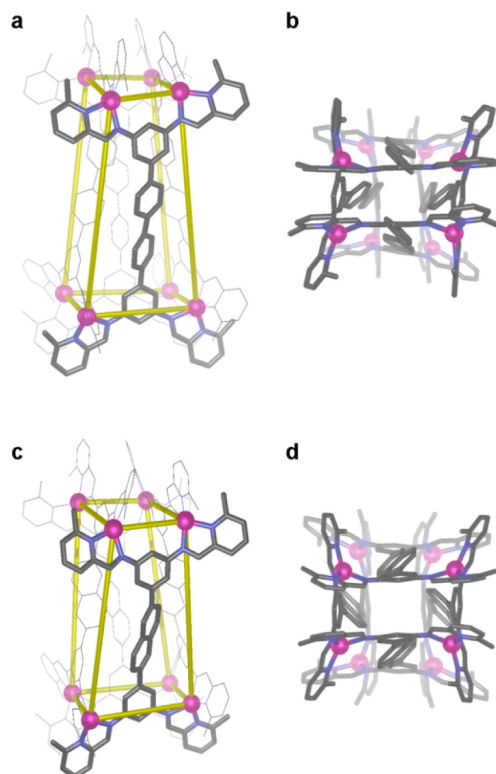
Figure 3.1.2: Crystal structures of **1b**-D_{2d}·BF$_4$ (a,b) and **1c**-D_2·PF$_6$ (c,d).[7] (a,c) Side view; (b,d) top view. Hydrogen atoms, solvent molecules, and counterions are omitted for clarity.

an acetonitrile solution of the respective complexes. X-ray analyses revealed the presence of **1b**-D_{2d} (Figure 3.1.2a,b) and **1c**-D_2 (Figure 3.1.2c,d), whose structures resemble that of **1a**-D_{2d}. For **1b**-D_{2d} the elongation of the ligand backbone from terphenylene to quaterphenylene did not result in an increase of the width of the tube channel, but rather narrows it. The shorter faces (Figure 3.1.2b) are slightly distorted from a rectangular geometry. The average Cu-Cu distance of the shorter edge of the top and bottom faces was 5.3 Å, 0.1 Å shorter than in **1a**-D_{2d}. For **1c**-D_2 the presence of a naphthalene spacer reduces the symmetry of the complex by removing the mirror plane that

bisects the ligand. The naphthalene spacer also introduces an offset between the two terminal phenyl rings, which slightly widens the tube channel. The shorter edge of the rectangular face in $1c$-D_2 (5.6 Å) is 0.2 Å longer than that in $1a$-D_{2d}.

Ag(I) can also be used in place of Cu(I) to form an M_8L_4 tube. The reaction between tetraamine **A**, 6-methyl-2-pyridine-carboxaldehyde **1** and AgBF$_4$ in acetonitrile produced 4-D_{2d} as the only observed product in solution, as verified by ^{1}H NMR and MALDI-MS. Doublets were observed for the two symmetry-independent imine protons, with $J = 5.9$ and 7.8 Hz due to the coupling between $^{107/109}$Ag and the imine protons. Vapor diffusion of diethyl ether into an acetonitrile solution of 4-$D_{2d}\cdot$BF$_4$ allowed the isolation of single crystals suitable for X-ray analysis. The solid state structure reveals an approximate D_{2d}-symmetric M_8L_4 topology, consistent with solution observations (Figure 3.1.3). Compared to analogous Cu(I) tubes ($1a$-D_{2d}, $1b$-D_{2d} and $1c$-D_2) 4-$D_{2d}\cdot$BF$_4$ is more distorted: the top view of 4-$D_{2d}\cdot$BF$_4$ shows that the shorter faces of the complex form a parallelogram (Figure 3.1.3b), whereas those in the Cu(I) tubes approximate a rectangle. Furthermore the Ag(I) centers in 4-$D_{2d}\cdot$BF$_4$ show a greater degree of distortion from idealized tetrahedral geometry compared to the Cu(I) centers in $1a$-$D_{2d}\cdot$BF$_4$ with N-Ag-N angles in the range 72-154° compared N-Cu-N angles of 79-138° in its Cu(I) analogue.

Host-Guest Chemistry

In previous work, we demonstrated that tube $1a$-$D_4\cdot$BF$_4$ is capable of binding the complex anion Cu(Au(CN)$_2$)$_2^-$. The Cu(I) ion bridges the two NC-Au-CN$^-$, and it could be substituted by Ag(I) to give the Ag(Au(CN)$_2$)$_2^-$ adduct of $1a$-$D_4\cdot$BF$_4$.

We have since determined DFT binding energies for these guests, and for every analogous guest with a different combination of central group-11 metal and dicyano group-11-metalate, inside of **1a** in acetonitrile continuum solvent. The results are shown
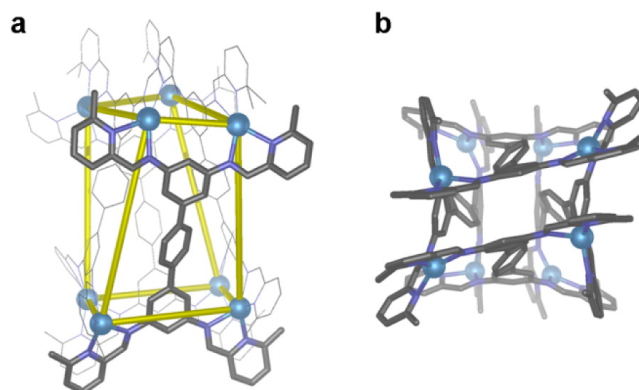
Figure 3.1.3: Crystal structure of Ag(I) complex $\mathbf{4}$-D_{2d}·BF$_4$. (a) Side view highlighting one ligand in thicker stick presentation. (b) Top view showing the distortion at the Ag(I) centers.

in Table 3.1.2. Counterions were not included. Because of the high computational cost of optimizing the geometry of the large host-guest complexes, energies were not computed for the experimentally unobserved binding of the dicyanoargentate and dicyanocuprate guests in the D_{2d} host isomer.

Binding energies were calculated by determining the difference in energy between each host-guest complex and its corresponding separated starting compounds and acetonitrile-filled D_4 host isomer at 5 μM concentrations of the host-guest complexes. For consistency with the experimental conditions employed (*vide infra*), free Au(I) was modeled as the cationic moiety of the salt Au(tmbn)$_2$SbF$_6$ (tmbn = 2,4,6-trimethoxybenzonitrile), whereas free Cu(I) and Ag(I) were modeled as the tetrakis(acetonitrile) complexes.

The computed energies of binding matched the experimentally observed trend, where guests bound more strongly in the D_4 isomer and larger group-11 metals bound more strongly than smaller ones. This trend is consistent, allowing for reasonable extrapolation to the binding of the Ag(CN)$_2^-$ and Cu(CN)$_2^-$ guests in the D_{2d} host isomer. It is

central cation	peripheral anions in N≡C-M'-C≡N-M-N≡C-M'-C≡N		
	$Cu(CN)_2^-$	$Ag(CN)_2^-$	$Au(CN)_2^-$
D_4-host			
Cu(I)	-36.8	-52.7	-69.0
Ag(I)	-41.8	-53.1	72.4
Au(I)	-116.3	-129.3	-143.9
D_{2d}-host			
Cu(I)	^{a}	^{a}	2.9
Ag(I)	^{a}	^{a}	-15.1
Au(I)	^{a}	^{a}	-97.9

^{a}These values were not determined; no such binding is observed experimentally.

Table 3.1.2: Computed energies of incorporation of group-11 metal centers (rows) and dicyano ends (columns) in kJ mol^{-1}

important to note that these energies of the host-guest complexes are relative to those of the solvent-filled cage and guest precursors, not the polymeric precipitate actually observed when no host is present. This distinction is likely to explain why we still obtain negative binding energies for the $Cu(Ag(CN)_2)_2^-$ and $Ag(Ag(CN)_2)_2^-$ guests, which are not observed to bind *in situ*, as these energies were not calculated relative to the global energy minimum.

Contrary to our previous inference,[155] it seems that the trend of favoring heavier group-11 metals at the center of the complex anion is predicated not upon increased cation-π interaction with the organic linkers of the host cage, but upon stronger intraguest binding. Figure 3.1.4 shows the DFT energetics of the stepwise formation and insertion of the bis-dicyanoaurate guests into both **1a**-D_4 and **1a**-D_{2d}. For this hypothetical pathway, the global minimum energy of complex **1a** was assumed to be the D_4 isomer with two incorporated acetonitrile guests, and consequently this structure was chosen as the starting material for the host cage in the second step of the pathway. By

comparing the energies of guest formation to those of host-guest complexation, the role of the comparatively strong gold-nitrogen bonds in stabilizing the $[\text{Au}(\text{Au}(\text{CN})_2)_2 \subset$ **1a**-$D_4]$ complex becomes apparent.
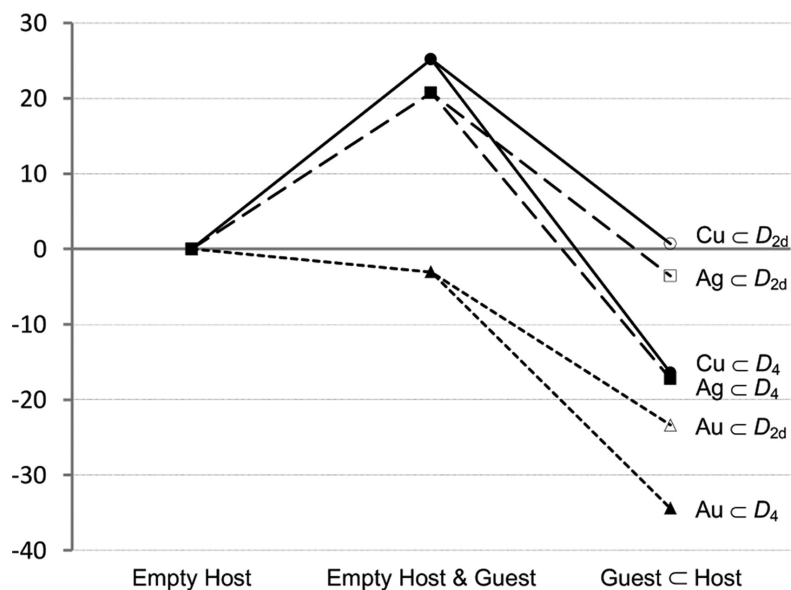
Figure 3.1.4: Calculated energetics for stepwise formation and incorporation of group-11 metal-centered bis-dicyanoaurates into **1a**-D_4 ("Guest $\subset$ Host" data from last column of Table 3.1.2, "Empty Host" for guests as their dissociated precursors).

In keeping with our theoretical predictions, the addition of $\text{Au}(\text{tmbn})_2\text{SbF}_6$ (1.2 equiv) to $[\text{Cu}(\text{Au}(\text{CN})_2)_2 \subset \textbf{1a}\text{-}D_4\cdot\text{BF}_4]$ (1 equiv) led to the formation of a new host-guest complex $[\text{Au}(\text{Au}(\text{CN})_2)_2 \subset \textbf{1a}\text{-}D_4\cdot\text{BF}_4]$ (Scheme 3.1.2), as verified by ESI-MS. A low resolution crystal structure was obtained for the product, showing that Au(I) replaced Cu(I) as the bridging cation within the guest.

NMR spectra of $[\text{Au}(\text{Au}(\text{CN})_2)_2 \subset \textbf{1a}\text{-}D_4\cdot\text{BF}_4]$ revealed additional splitting: many ^{1}H signals appeared as a set of three closely spaced peaks of roughly equal intensity. Using isotopically labeled $\text{KAu}(^{13}\text{CN})_2$, in the ^{13}C NMR spectrum (Figure S37, supporting information) the ^{13}C-labeled guest gave rise to three doublets and four singlets
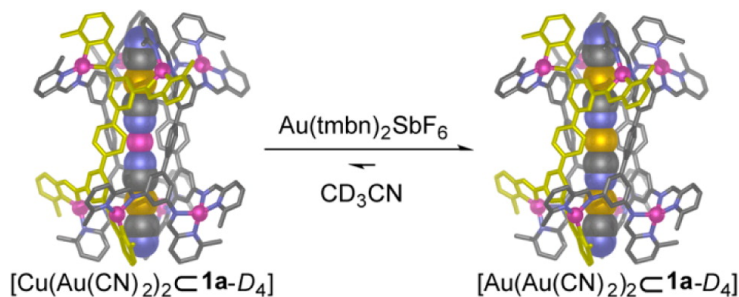
Scheme 3.1.2: Formation of trigold host-guest complex *via* transmetalation.[a]

[a]The two representations shown are X-ray crystal structures. One configuration of the trigold guest is shown.

with different intensity, indicating the presence of multiple carbon environments.

The ^{13}C NMR spectra of the labeled host-guest complexes [Cu(Au(^{13}CN)$_2$)$_2$ $\subset$ **1a**-D_4] and [Ag(Au(^{13}CN)$_2$)$_2$ $\subset$ **1a**-D_4] exhibited a pair of characteristic doublets with J_{C-C} = 47 Hz for the guest signals, consistent with conservation of the NC-Au-CN aurocyanide configurations within the complex anion guests. Similar signals were not observed in the ^{13}C NMR spectrum for [Au(Au(^{13}CN)$_2$)$_2$ $\subset$ **1a**-D_4]. This observation indicates that in [Au(Au(CN)$_2$)$_2$ $\subset$ **1a**-D_4], the guest configuration is different from that in [Cu(Au(CN)$_2$)$_2$ $\subset$ **1a**-D_4] and [Ag(Au(CN)$_2$)$_2$ $\subset$ **1a**-D_4]. We thus infer that the conformation NC-Au-CN-Au-NC-Au-CN$^-$ is not adopted by the guest in [Au(Au(CN)$_2$)$_2$ $\subset$ **1a**-D_4]. Our data were consistent with the guest adopting the conformations NC-Au-CN-Au-CN-Au-CN$^-$ and NC-Au-NC-Au-CN-Au-CN$^-$, in which each gold(I) center is bonded to at least one carbon atom.

DFT calculations of the relative energies of the free complex anions in continuum acetonitrile solvent predict NC-Au-CN-Au-CN-Au-CN$^-$ and NC-Au-NC-Au-CN-Au-CN$^-$ to be more stable than NC-Au-CN-Au-NC-Au-CN$^-$ by 15.5 and 14.6 kJ mol^{-1}, respectively. Thus, to have one gold atom not coordinated by at least one cyanide carbon

atom is disfavored energetically. In so far as only two complex anion isomers are predicted to dominate in the absence of encapsulation, and assuming that binding energies are similar for the different complex anion isomers, upon guest binding we expect to observe close to a 2:1 statistical distribution of NC-Au-CN-Au-CN-Au-CN$^-$, and NC-Au-NC-Au-CN-Au-CN$^-$. We thus infer the tripling of host signals in the NMR to result from *one* set of signals associated with binding of NC-Au-NC-Au-CN-Au-CN$^-$ and *two* sets of signals associated with binding of the asymmetric complex anion NC-Au-CN-Au-CN-Au-CN$^-$, which results in desymmetrization of the two ends of the tube. The presence of multiple conformations is mirrored in the solid-state behavior of group-11 cyanides.[166]

The titration of Au(tmbn)$_2$SbF$_6$ into an acetonitrile solution of [Cu(Au(CN)$_2$)$_2$ $\subset$ **1a**-D_4·BF$_4$] allowed the stability constant of 1.6×10^{11} M^{-3} for [Au(Au(CN)$_2$)$_2$ $\subset$ **1a**-D_4·BF$_4$] to be determined, 129 times greater than that of [Cu(Au(CN)$_2$)$_2$ $\subset$ **1a**-D_4·BF$_4$] and 3.7-fold higher than [Ag(Au(CN)$_2$)$_2$ $\subset$ **1a**-D_4·BF$_4$].

Tetraphenyl tube **1b**·PF$_6$ did not form any host-guest complex in the presence of KAu(CN)$_2$, which suggests the energy gained by trapping the guest Cu(Au(CN)$_2$)$_2^-$ is not enough to compensate energy lost during isomerization from **1b**-D_{2d} to **1b**-D_4. In contrast, for naphthalene-based tube **1c**·PF$_6$ the addition of KAu(CN)$_2$ resulted in a rapid and clean transformation to [Cu(Au(CN)$_2$)$_2$ $\subset$ **1c**-D_4] (Scheme 3.1.3), despite the low abundance of **1c**-D_4 in solution. The crystal structure of the product confirmed the encapsulation of Cu(Au(CN)$_2$)$_2^-$ within **1c**-D_4, consistent with NMR and ESI-MS observations. The central Cu(I) within the guest could be replaced by Ag(I) or Au(I) in a similar way to the analogous terphenyl tube [Cu(Au(CN)$_2$)$_2$ $\subset$ **1a**-D_4] (Scheme 3.1.3).

Linear dicyanoargentate, Ag(CN)$_2^-$, has very similar dimensions to Au(CN)$_2^-$, yet no host-guest complex formation was observed when **1a**·PF$_6$ was treated with Ag(CN)$_2^-$
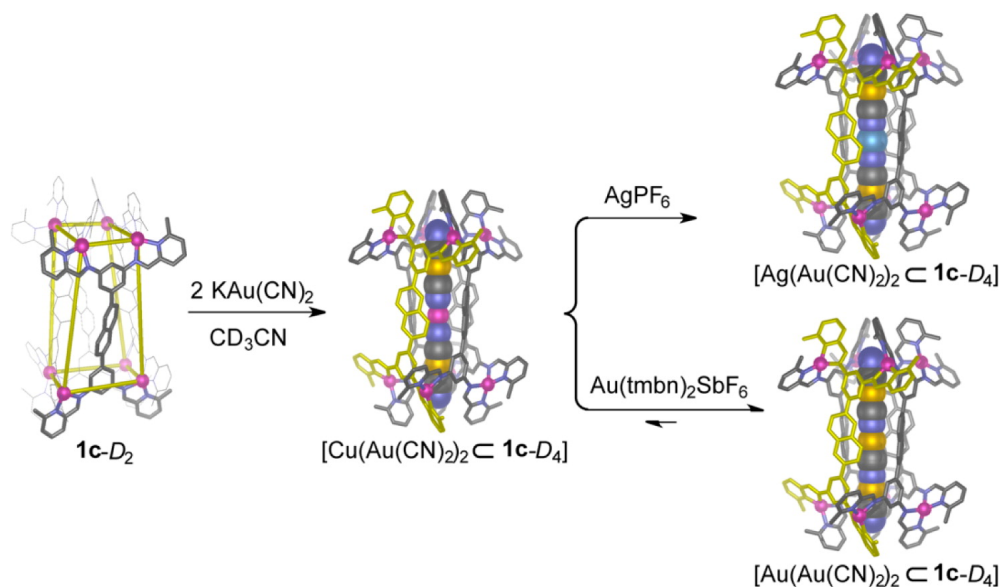
Scheme 3.1.3: Formation of host-guest complexes from **1c**·PF$_6$.[a]

---

[a][Cu(Au(CN)$_2$)$_2$ ⊂ **1c**-D_4] is shown as the X-ray crystal structure.

in the presence of either Cu(I) or Ag(I). In contrast, when Au(I) was added, a new D_4-symmetric complex was rapidly generated. This new product was not the expected [Au(Ag(CN)$_2$)$_2$ ⊂ **1a**-D_4]·PF$_6$, but a transmetalated product [Ag(Au(CN)$_2$)$_2$ ⊂ **1a**-D_4]·PF$_6$, as verified by NMR and ESI-MS (Scheme 3.1.4). In the absence of the host **1a**·PF$_6$, mixing Ag(CN)$_2^-$ with Au(I) resulted in the formation of white precipitate, which we infer to be the polymeric mixed-metal cyanide.[167, 168] Host **1a**·PF$_6$ therefore acts as a solubilizing carrier, allowing the encapsulated guest to be studied using routine spectroscopic methods.

The lack of observed binding of [Au(Ag(CN)$_2$)$_2$]$^-$ in **1a** can be explained computationally. DFT calculations show that while the fully formed guest Au(Ag(CN)$_2$)$_2^-$ is predicted to bind to **1a**-D_4 more strongly than Ag(Au(CN)$_2$)$_2^-$ (by 56.9 kJ mol^{-1}, see
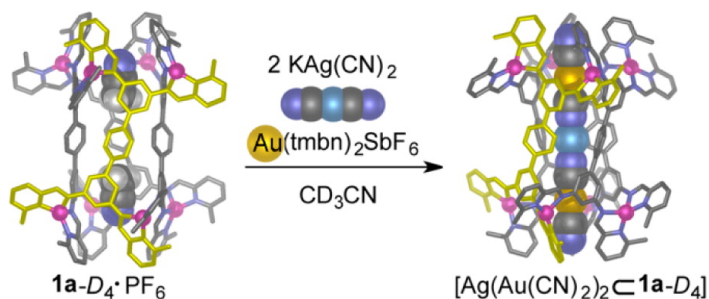
Scheme 3.1.4: Formation of $[\text{Ag}(\text{Au}(\text{CN})_2)_2 \subset \textbf{1a-}D_4]\cdot\text{PF}_6$ *via* transmetalation between $\text{Ag}(\text{CN})_2^-$ and $\text{Au}(\text{I})$

Table 3.1.2), the transmetalation of dicyanoargentate to dicyanoaurate by the pathway

$$\text{Ag}(\text{CN})_2^- + \text{Au}(\text{tmbn})_2^+ + 4\text{CH}_3\text{CN} \rightarrow \text{Au}(\text{CN})_2^- + \text{Ag}(\text{CH}_3\text{CN})_4^+ + 2\text{tmbn}$$
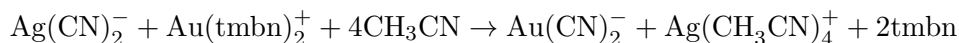
is predicted to be exoergic by 146.4 kJ mol^{-1}, making the $[\text{Ag}(\text{Au}(\text{CN})_2)_2 \subset \textbf{1a-}D_4]$ complex more enthalpically favorable than its gold bis-dicyanoargentate counterpart by 235.6 kJ mol^{-1}.

3.1.3 Conclusion

In this study we have developed a general synthetic procedure for M_8L_4 tubular complexes using tetraamines with two 3,5-diaminophenylene moieties connected by a suitable spacer. This technique allows facile investigations into the influences of subtle changes in any of the subcomponents on the complex structure. The M_8L_4 tubes are present in solution as either D_4-symmetric or D_{2d}/D_2-symmetric isomers, which are in dynamic equilibrium. The D_4 isomer, which is the only one observed to bind guests, is more stabilized when PF_6^- is present as the counteranion, whereas the D_{2d}/D_2 isomer is stabilized by the elongation of the ligand or the introduction of an offset between tube termini. Further systemic adaptation is revealed in the host-guest chemistry of the tubes. Dicyanoaurate is a necessary subcomponent of all guests that we observe

to be bound by any tube, and the system will undertake to transform guests in order to achieve an optimal host-guest complex through guest recombination or transmetalation. This work therefore builds upon and contributes to fundamental studies of systems chemistry,[169] specifically the dynamic response of a system to external stimuli, as is required in the design and creation of increasingly complex molecular machines.[170–174] The design of a system that is specifically adapted to bind gold cyanides may also be of relevance to the mining industry,[175] and the ability to specifically bind linear guests may allow for their catalytic transformation, as has been observed in other systems.[114–119]

3.1.4 Methods

Computational Methods

All calculations employed the PBE-D3[13,176] functional as implemented in the ADF 2013 software package.[177–179] TZP basis sets with large frozen cores were employed for metal atoms, and DZP basis sets for the organic linkers.[180] The zero-order regular approximation (ZORA) was employed to account for scalar relativistic effects.[181–183]

Empty cages and host-guest complexes were first optimized in the gas phase, and final energies were computed from single-point calculations on these minima including acetonitrile solvation effects computed from the COSMO continuum solvent model.[184] When representative host-guest complexes were subjected to reoptimization including solvation effects, their energies were observed to fluctuate but not to decrease (or converge, because of apparent numerical noise), on which basis we concluded that for the large cage structures, solvated single-point calculations on gas-phase geometries were sufficiently accurate for our purposes. The geometries of small molecule guests and guest precursors, however, were optimized including acetonitrile solvation effects. Because of the size of the host structures, no frequency calculations were performed, and

consequently the theoretical energies reported in this section include no thermal corrections.

General Experimental Methods

Unless otherwise specified, all starting materials were purchased from commercial sources and used as supplied. Chromatographic separations were performed on silica gel 60 (particle size: 0.040-0.063 mm) purchased from Aldrich. TLC was performed on silica gel 60 F254 plates purchased from Merck and visualized under ultraviolet light (254 nm). NMR spectra were recorded on a Bruker DRX-400 and Bruker Avance 500 Cryo. Chemical shifts (δ) are reported in parts per million (ppm) and are reported relative to acetonitrile-d_3 at 1.94 ppm at 298 K unless otherwise noted. Low resolution electrospray ionization mass spectra (ESI-MS) were obtained on a Micromass Quattro LC, infused from a Harvard Syringe Pump at a rate of 10 μL per minute. MALDI was carried out by the EPSRC National MS Service Centre at Swansea. Building blocks [1,1':4',1"-terphenyl]-3,3",5,5"-tetraamine **A** and Au(tmbn)$_2$SbF$_6$ were synthesized following literature procedures.[155, 185]

3.2   Pyrene-Edged Fe(II)$_4$L$_6$ Cages Adaptively Reconfigure During Guest Binding

3.2.1   Introduction

Metal-organic cages[134,186–191] have attracted significant recent attention due to their wide-ranging applications[192] as photoreactors[193,194] and in gas sequestration,[195] catalysis,[114,117,118,196–199] stabilization of reactive species,[200–202] and generation of unusual reaction products.[203]   These abiological structures are also of relevance as functional mimics of biological molecules such as protein receptors and enzymes. In order to extend the range of applications of synthetic metal-organic capsules toward the level of complexity exhibited by biological hosts it is necessary to create synthetic capsules capable of tightly and selectively binding large substrates. Cages assembled from ligands with extended aromatic panels[204,205] have shown promise as hosts for a variety of large neutral molecules.[2,206–208] Such hosts provide well-enclosed cavities isolated from their surroundings in addition to cage walls rich in π-electron density to provide favorable interactions with targeted guests. In addition to binding spherical[131] or planar aromatic guests of high symmetry,[209,210] the design of hosts for asymmetric molecules is necessary for potential applications such as drug delivery[211,212] and asymmetric catalysis.[213] The design of specifically tailored asymmetric hosts remains challenging[154,214,215] so it is desirable to employ hosts that can be readily prepared from simple symmetric building blocks.

Subcomponent self-assembly has been shown to be a versatile approach for the

creation of increasingly complex architectures[152,216,217] which are obtained from simple building blocks through the formation of dynamic-covalent (C=N)[135] and coordinative (N → M) bonds during the same self-assembly process. We[216,218] and others[137,144,149,219] have recently employed this technique to achieve a variety of functional ends, including to obtain tetrahedral structures with different shapes and varied molecular recognition properties, based on the self-assembly of iron(II) with amine-containing subcomponents and 2-formylpyridine.[207,220–223] An inherent advantage of this approach is that the properties of the metal-organic cages can be readily altered[224] through variation of the subcomponents employed.[142] Herein, we describe the preparation of two new Fe_4L_6 cages from two isomeric pyrene-containing diamines. The two cages display contrasting guest-binding properties depending on the arrangement of the pyrene panels around the surface of the cage; the cage based on a 1,6-pyrene scaffold provides a suitably isolated microenvironment for effective guest-binding while the 2,7-pyrene edged cage does not encapsulate neutral guests. In addition to examining the host-guest properties of the constitutionally isomeric cages, we show how different diastereomers of one of the cages contribute differentially to guest binding, which led to guest-induced adaptation on a system-wide level.

3.2.2   Results and Discussion

Self-Assembly of Cages 1-2

Pyrene-containing subcomponents **A** and **B** were each synthesized in a single step from commercially available starting materials *via* Pd-catalyzed Suzuki-Miyaura cross-coupling reactions;[225] a full description of their synthesis is provided in the supporting information. The reaction of diamine **A** (6 equiv) with 2-formylpyridine (12 equiv) and iron(II) triflimide (4 equiv) yielded tetrahedral cage **1** (Scheme 3.2.1). The Fe_4L_6 stoichiometry of the assembly was confirmed by electrospray ionization mass spectrometry

(ESI-MS) (supporting information Figure S12).
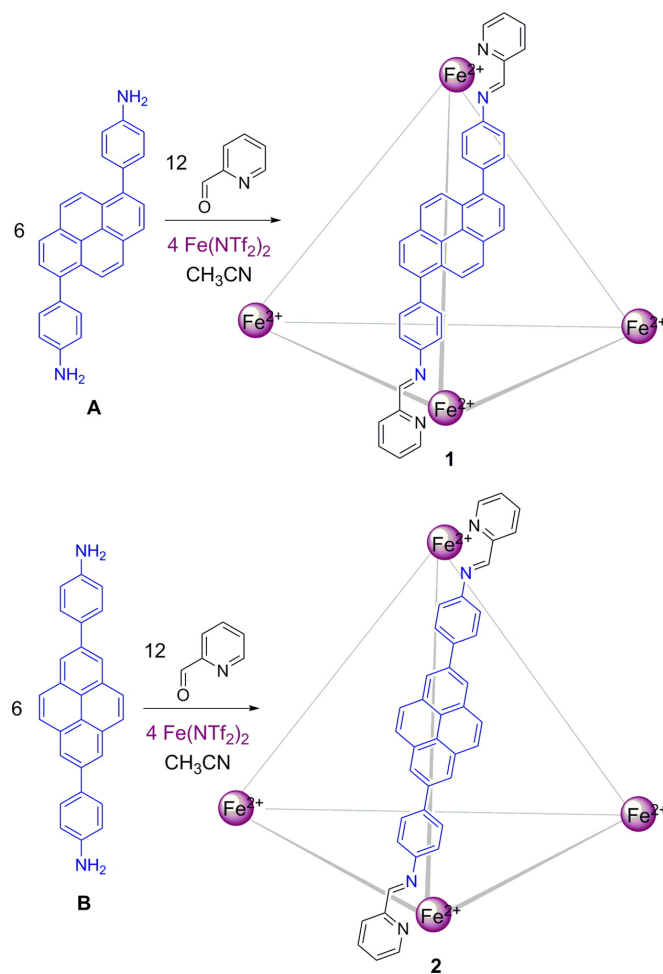
Scheme 3.2.1: Preparation of $[Fe_4L_6]^{8+}$ tetrahedra **1** and **2** *via* subcomponent self-assembly

Both the ^{1}H (supporting information Figure S5) and ^{13}C (supporting information Figure S7) NMR spectra of **1** were complicated; NMR signals were observed as clusters of peaks, consistent with a mixture of homochiral T ($\Delta\Delta\Delta\Delta/\Lambda\Lambda\Lambda\Lambda$),[226,227] heterochiral C_3 ($\Delta\Delta\Delta\Lambda/\Lambda\Lambda\Lambda\Delta$), and achiral S_4 ($\Delta\Delta\Lambda\Lambda$)[228] diastereomers[229] in equilibrium, as has been observed for other cages prepared *via* subcomponent self-assembly.[230,231] The

DOSY (diffusion-ordered spectroscopy) spectrum of **1** confirmed that all peaks between 5.7 and 9.2 ppm had the same diffusion coefficient (supporting information Figure S11). Deconvolution of the imine region of the ^{1}H NMR spectrum of **1** gave percentages of 13%, 42%, and 45% for **1**-T, **1**-C_3, and **1**-S_4, respectively, which is close to the expected statistical distribution of 12.5% T, 50% C_3, and 37.5% S_4, suggesting that the three diastereomers are of similar energy. All efforts to grow X-ray quality single crystals of **1** were unsuccessful, likely due to the presence of diastereomers and possible further conformational complexity arising from different conformations of the offset pyrene groups.

Density functional theory (DFT) was employed in order to gain further insight into the structure of **1**. The structures of the three diastereomers of **1** (Figure 3.2.1) were optimized in the TURBOMOLE software package[232–236] using the PBE-D3 functional[13, 176] and MIDI![237] (C, H, and N) and def2-TZVP[238, 239] (Fe) basis sets. The three isomers are predicted to be similar in energy with a slight preference for **1**-S_4, which is predicted to be 11.7 and 18.0 kJ mol^{-1} more stable than **1**-C_3 and **1**-T, respectively, consistent with the observed distribution of diastereomers in solution. This observed diastereomer distribution indicates that they are nearly isoenergetic, placing the error in the DFT energies at ~8 kJ mol^{-1}, which we consider reasonable, particularly given the difficulty in estimating differential rotational and vibrational contributions to entropy for systems of this size.

The metal-metal separations in **1** are calculated to be in the range 18.9-19.8 Å. The pyrene units in the energy-minimized structures display a variety of conformations. The cavity volume accessible for guest binding is expected to be strongly dependent on the conformation adopted by these groups in solution. The volume is expected to be maximized when the pyrene units adopt a conformation tangential to the edges of the tetrahedron as observed for four pyrene units in the DFT structures of **1**-T and

$\mathbf{1}$-C_3 but for only two pyrene units in $\mathbf{1}$-S_4 (Figure 3.2.1). A tangential conformation of the pyrene units is also expected to maximize the degree of cavity enclosure and minimize the size of the pores through which solvent and guest species may diffuse, factors expected to lead to efficient guest encapsulation.[2, 206]

The reaction of diamine $\mathbf{B}$ (6 equiv) with 2-formylpyridine (12 equiv) and iron(II) triflimide (4 equiv) yielded tetrahedral cage $\mathbf{2}$ (Scheme 3.2.1) as the only observed product as indicated by NMR spectroscopy, ESI-MS, and elemental analysis. The ^{1}H NMR spectrum of $\mathbf{2}$ (supporting information Figure S14) revealed a mixture of three diastereomers, with the ratio of $\mathbf{2}$-T:$\mathbf{2}$-C_3:$\mathbf{2}$-S_4 estimated to be 12%:45%:43%, which is close to the expected statistical distribution, as observed for cage $\mathbf{1}$.
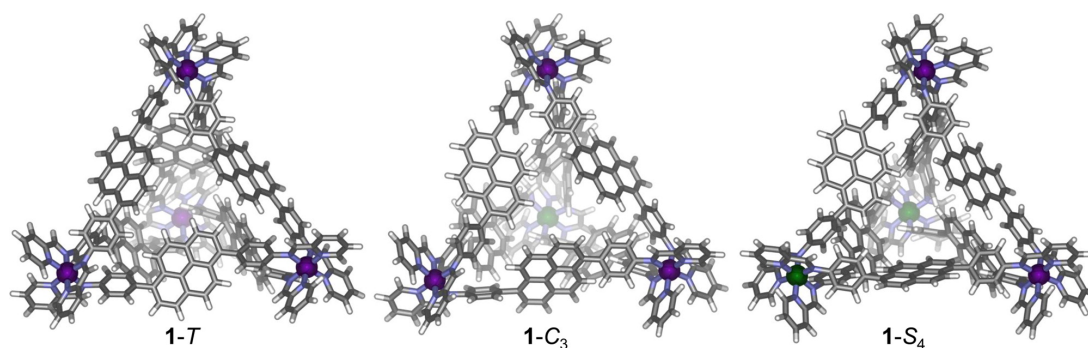
Figure 3.2.1: DFT-optimized structures of the three diastereomers of $\mathbf{1}$. Fe(II) centers with Δ and Λ stereochemistry are colored purple and green, respectively.

Vapor diffusion of benzene into an acetonitrile solution (1 mM) of $\mathbf{2}$·(NTf$_2$)$_8$ containing [^{n}Bu$_4$N]PF$_6$ (10 equiv) gave crystals of $\mathbf{2}$·(PF$_6$)$_8$ suitable for single-crystal X-ray diffraction analysis. Two representations of the X-ray structure of $\mathbf{2}$ are shown in Figure 3.2.2. Cage $\mathbf{2}$ crystallized in the triclinic space group P$\bar{1}$ with one complete cage molecule in the asymmetric unit. The crystals were found to contain the diastereomer of C_3 point symmetry, with both $\Lambda\Lambda\Lambda\Delta$ and $\Delta\Delta\Delta\Lambda$ enantiomers present in the unit

cell, related by inversion symmetry. Of the six ligands that bridge the four octahedral iron(II) centers, three ligands display a *syn* conformation, bridging iron(II) centers of opposing handedness, and three adopt an *anti* conformation, linking iron(II) centers of the same handedness. The pyrene units of the *anti* ligands almost completely close the cage face that they define (Figure 3.2.2, top). The remaining three faces are more open, with large pores (Figure 3.2.2, bottom). The interior of **2** is filled with three partial-occupancy benzene molecules in the solid state. The metal-metal separations are in the ranges 20.4-20.7 Å and 20.8-20.9 Å for the *syn* and *anti* ligands respectively, placing this cage among the largest M_4L_6 species to be structurally characterized to date.[230, 240, 241] In the solid state pairs of cage molecules associate through aromatic stacking interactions involving the most planar cage faces (supporting information Figure S75); these favorable intermolecular interactions coupled with the high abundance of the C_3 diastereomer in solution may explain the preferential crystallization[230, 231] of this cage isomer.

Host-Guest Chemistry of Cage 1

To investigate the scope of guest binding within **1**, the molecules listed in Figure 3.2.3 were screened as potential guests. Each prospective guest (5 equiv) was added to a CD_3CN solution of host **1** (1-3 mM), and the mixture was allowed to equilibrate prior to the acquisition of NMR and mass spectra. UV-vis spectra were observed to undergo only minimal changes upon guest binding, and the fluorescence of the pyrene moieties was largely quenched by the Fe(II) centers in the cages; hence, these techniques were not used to investigate guest binding. The addition of different guests brought about a re-equilibration among the different diastereomers of **1**, as the system adapted in order to maximize binding affinity.[231]
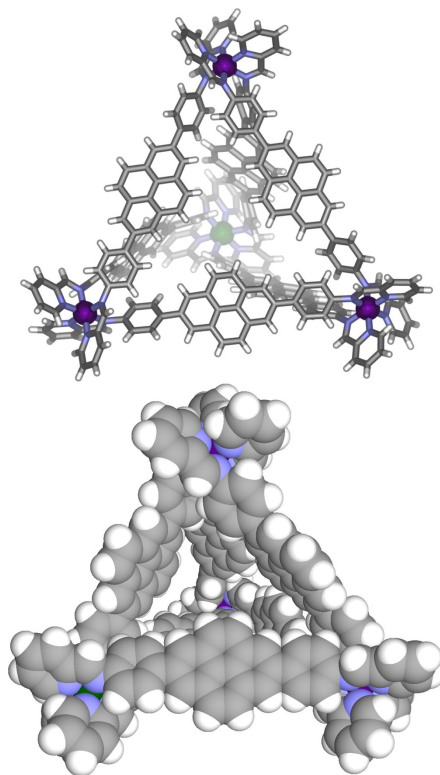
Figure 3.2.2: Two views of the cationic part of the crystal structure of **2**-C_3 showing the $\Delta\Delta\Delta\Lambda$ enantiomer: view down the pseudo-C_3-axis (top) and space-filling representation of the structure illustrating one of the open faces (bottom). Counterions, solvents, and disorder are omitted for clarity. Δ and Λ Fe(II) centers are colored purple and green, respectively.

Cage **1** was initially investigated as a fullerene receptor, because fullerenes were expected to interact with the pyrene moieties through $\pi - \pi$ stacking and have previously been shown to be encapsulated by metal-organic cages containing large aromatic panels.[2, 131, 206, 207, 242–245] Both C_{60} and C_{70} were observed to form 1:1 host-guest complexes with cage **1** in CD_3CN. In each case host occupation was inferred through disappearance of the peaks corresponding to the free host and concurrent appearance of a new set of

(a)

C$_{60}$ C$_{70}$ *coronene*

(b)

perylene   *pyrene*   *triphenylene*

cholesterol   *strychnine*   *diadamantane*

(c)

tetracene

1,4,5,8-naphthalene tetracarboxylic dianhydride   *triptycene*
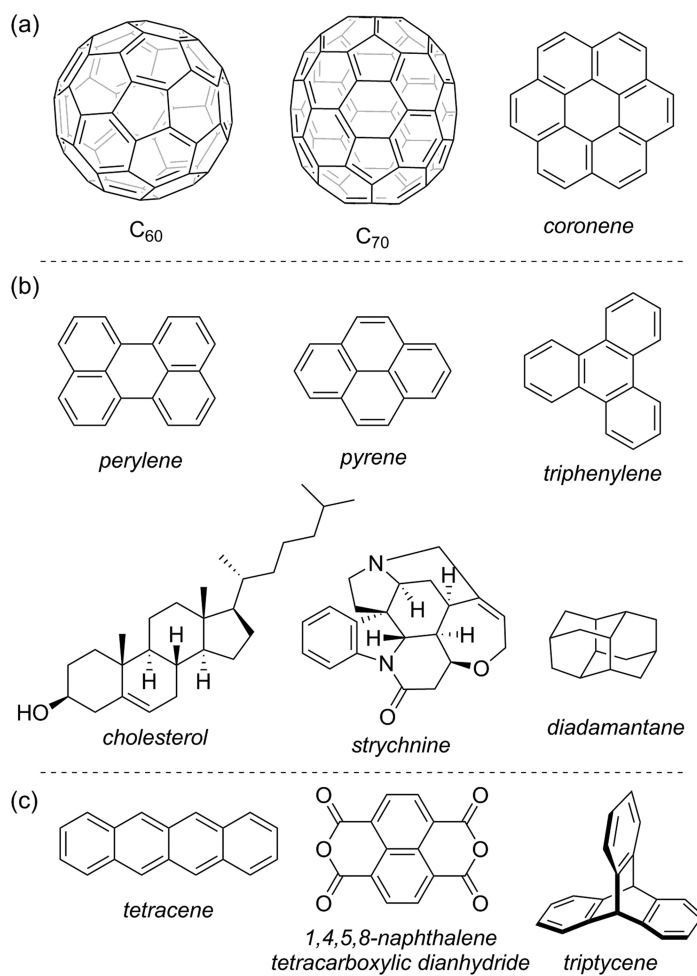
Figure 3.2.3: Prospective guest molecules for host **1**: (a) larger guests that show slow-exchange binding by NMR; (b) guests for which fast-exchange binding was observed; (c) compounds for which no evidence of encapsulation was observed.

cage peaks corresponding to the host-guest complex. ESI-MS of the host-guest complexes confirmed formation of the 1:1 complexes $[C_{60} \subset \mathbf{1}]$ and $[C_{70} \subset \mathbf{1}]$; in each case the free host was no longer observed in the ESI mass spectrum (supporting information Figures S35 and S45).

The imine region of the ^{1}H NMR spectrum of $[C_{60} \subset \mathbf{1}]$ appeared simpler than that of cage $\mathbf{1}$, displaying five signals of equal intensity, which corresponds to a 20%:80% mixture of the T and C_3 isomers (Figure 3.2.4). As these two isomers were equally amplified relative to the statistical distribution, we infer their C_{60} affinities to be similar. ^{1}H NMR spectra revealed no detectable amount of the S_4 isomer, suggesting that C_{60} binding in this isomer is not favorable. Examination of the phenyl resonances of $[C_{60} \subset \mathbf{1}]$ also revealed the presence of five magnetically distinct ligand environments: one for the T isomer and four for the C_3 isomer, (Figure 3.2.4 and supporting information Figure S28). For each of these environments, two distinct sets of signals attributable to those phenyl protons that are *endo* (H^6 and H^7) and those that are *exo* ($H^{6'}$ and $H^{7'}$) to the edge of the cage were observed, consistent with slow rotation of the phenyl rings on the NMR time scale, compared to the fast rotation observed for cage $\mathbf{1}$ in the absence of guest molecules. The phenyl resonances are also more dispersed relative to those of the empty cage due to contacts with the aromatic guest. Although C_{60} is effectively insoluble in CD_3CN,[246] the ^{13}C NMR spectrum of $[C_{60} \subset \mathbf{1}]$ in CD_3CN showed an intense resonance at 140.1 ppm, providing further confirmation of encapsulation of C_{60} by host $\mathbf{1}$ (supporting information Figure S29).

The binding energies of the three diastereomers of $\mathbf{1}$ with C_{60} were further probed through DFT calculations. The structures of $[C_{60} \subset \mathbf{1}\text{-}T]$, $[C_{60} \subset \mathbf{1}\text{-}C_3]$, and $[C_{60} \subset \mathbf{1}\text{-}S_4]$ were computed. The energy-minimized structures of $[C_{60} \subset \mathbf{1}]$ predicted all six pyrene units to lie tangentially to the edges of the cage, resulting in favorable $\pi - \pi$ interactions with the encapsulated C_{60} and a well-enclosed cavity. Pyrene units on
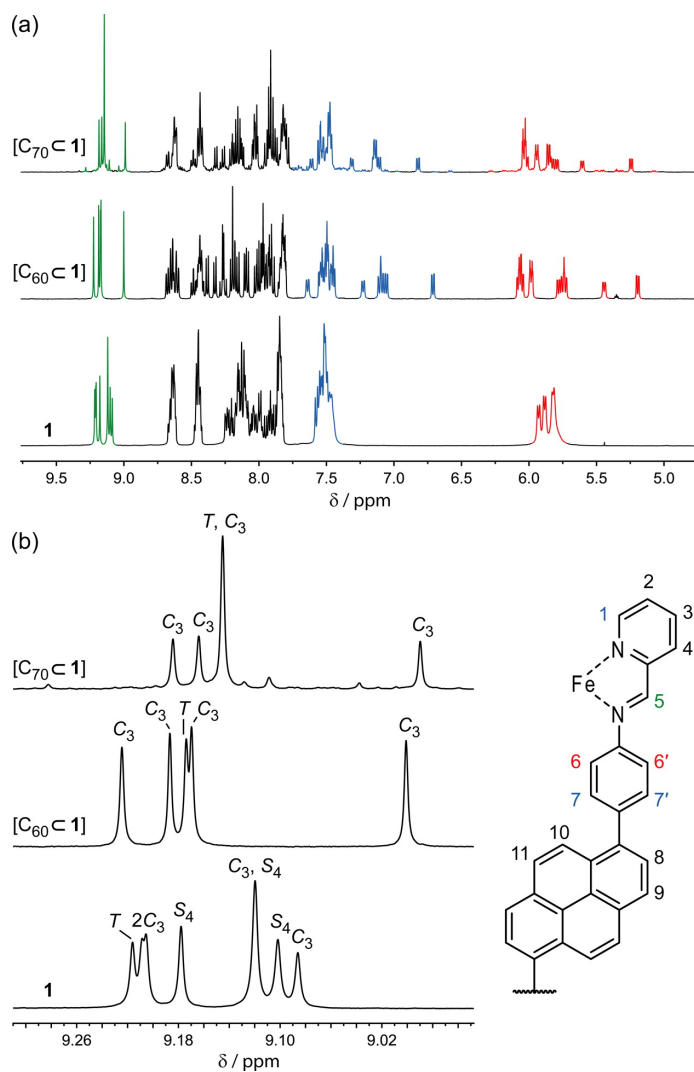
Figure 3.2.4: (a) Aromatic region of the ^{1}H NMR spectra (500 Hz, CD$_3$CN, 298 K) of cage **1**, [C$_{60}$ ⊂ **1**] and [C$_{70}$ ⊂ **1**]. The imine protons (H^5) are colored green, phenyl H^6 and H$^{6'}$ are colored red, and phenyl H^7, H$^{7'}$ and pyridyl H^1 are colored blue. (b) Expansion of the imine region of the ^{1}H NMR spectra of cage **1**, [C$_{60}$ ⊂ **1**] and [C$_{70}$ ⊂ **1**] with the peaks for the T, C_3, and S_4 isomers labeled.[b]

opposite edges of the tetrahedron are separated by ca. 13 Å, and the cavity volumes of all three isomers are estimated to be in the range 625 ± 5 Å^3 using VOIDOO.[247] This void matches the size and shape of the spherical guest well (Figure 3.2.5).
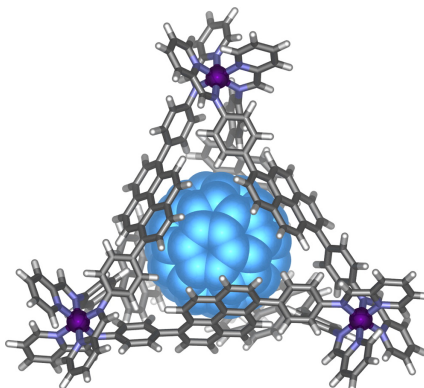
Figure 3.2.5: DFT-optimized structure of $[C_{60} \subset \mathbf{1}]$. The $\Delta\Delta\Delta\Lambda$ enantiomer of the most abundant C_3 isomer is shown with the Λ Fe(II) center behind the fullerene.

The computed energies of binding (Table 3.2.1) match the experimentally observed trend. While the $\mathbf{1}$-S_4 diastereomer is predicted to be thermodynamically favored when empty, the energetic cost of deforming it to accommodate the guest is significantly higher than predicted for the other two cage diastereomers, thereby disfavoring the formation of the $[C_{60} \subset \mathbf{1}$-$S_4]$ adduct. Examination of the overlaid empty and deformed structures (supporting information Figures S76-S78) shows that while only two pyrene rings must rotate to incorporate C_{60} in the C_3 and T diastereomers, four must rotate in the S_4 isomer. Even in the absence of accounting for the energy required to deform the cage (and guest) for binding, the host-guest complexation energy for $\mathbf{1}$-S_4 is still the lowest out of the three isomers, consistent with the observation that C_{60} is not observed to bind to this diastereomer. Nevertheless, the span of binding energies of C_{60} to preorganized hosts is only 18.8 kJ mol^{-1} (line 4, Table 3.2.1), while the span of

deformation energies required to organize the host diastereomers from their minimum-energy geometries is 51.9 kJ mol^{-1}; *i.e.*, it is the deformation energy that is decisive for the change in diasteromeric population of the $C_{60} \subset 1$ isomers. The DFT analysis thus provides insight into both adaptation on the molecular level, through rotation of the pyrene units to provide a tailored guest-binding pocket, as well as the system-wide level through diastereomer interconversion,[231] in order to express the diastereomers that form the most stable host-guest complexes.

E(kJ mol^{-1})	$\mathbf{1}$-C_3	$\mathbf{1}$-S_4	$\mathbf{1}$-T
$\mathbf{1}$ E_{relative}	0.0	-11.7	6.3
$[C_{60} \subset \mathbf{1}]$ E_{relative}	0.0	59.4	22.2
$\Delta E_{\text{deformation}}$ ^{a}	33.9	85.8	41.0
$\Delta E_{\text{host-guest}} - \Delta E_{\text{deformation}}$ ^{b}	-515.9	-497.1	-507.5

Table 3.2.1: DFT electronic energies in kJ mol^{-1} for each diastereomer of $\mathbf{1}$ and $[C_{60} \subset \mathbf{1}]$ Relative to $\mathbf{1}$-C_3 and $[C_{60} \subset \mathbf{1}$-$C_3]$, respectively

^{a}Energy of host at geometry adopted in complex relative to relaxed geometry when empty.
^{b}Energy of guest binding with host predistorted to geometry found in complex.

Similar trends were observed in the ^{1}H NMR spectrum of $[C_{70} \subset \mathbf{1}]$; the distribution of the T, C_3, and S_4 isomers was estimated to be 32%, 63%, and 5%. As observed for $[C_{60} \subset \mathbf{1}]$, the C_3 isomer was the most abundant species in the host-guest mixture while the S_4 isomer was disfavored compared to the ratio observed for the free host $\mathbf{1}$ (Figure 3.2.4). However, the T isomer shows the largest amplification relative to the statistical distribution, suggesting that it formed the most stable host-guest complex with the larger C_{70} guest.

Host $\mathbf{1}$ could be utilized for the extraction of fullerenes from fullerene soot. When $\mathbf{1}$ (5% by weight) was agitated with fullerene soot in CH_3CN for 10 days at 343 K, the ESI-MS showed peaks corresponding to $[C_{60} \subset \mathbf{1}]$ and $[C_{70} \subset \mathbf{1}]$ with intensities in a ratio of roughly 1:1 (supporting information Figure S47), compared to the reported abundances

of 66.6% and 23.4% for C_{60} and C_{70}, respectively, in the commercial product.[248] This observation suggests that **1** has a slight preference for encapsulation of C_{70} over C_{60}. Traces of host-guest complexes of higher fullerenes were also detected.

No guest substitution was detected by ^{1}H NMR or ESI-MS when excess C_{70} was added to a solution of $[C_{60} \subset \mathbf{1}]$ following 7 days at 343 K (supporting information Figures S48 and S49), nor when excess C_{60} was added to a solution of $[C_{70} \subset \mathbf{1}]$ (supporting information Figure S50 and S51). We infer that guest release rates for C_{60} and C_{70} are slow, resulting in the fullerene guests becoming kinetically trapped inside the cavity of **1** under the experimental conditions employed.[249]

Further binding studies of large hydrophobic guest molecules were carried out using planar polycyclic aromatic hydrocarbons (PAHs). The addition of excess coronene (5 equiv) to **1** in CD_3CN resulted in broadening of the ^{1}H NMR spectrum to such a degree that peaks for individual cage diastereomers could no longer be resolved (supporting information Figure S52). ESI-MS of the mixture suggested formation of a host-guest complex in which exactly 2 equiv of coronene were encapsulated per host (supporting information Figure S55). The encapsulated coronene gave rise to a broad ^{1}H NMR signal at 5.66 ppm, which is shifted significantly upfield relative to that of free coronene at 9.03 ppm. The broad NMR of $[\text{coronene}_2 \subset \mathbf{1}]$ could be due to an intermediate rate of exchange between free and bound guests on the NMR time scale, or to tumbling of the bound coronenes within host **1**. Cooling a CD_3CN solution of $[\text{coronene}_2 \subset \mathbf{1}]$ to 233 K led to a sharpening and increase in number of signals in the ^{1}H NMR spectrum (supporting information Figure S54), although dynamic behavior was not completely frozen out within the temperature range accessible in CD_3CN. The DOSY spectrum of $[\text{coronene}_2 \subset \mathbf{1}]$ at 233 K (supporting information Figure S53) confirmed that the signals of coronene diffused at the same rate as those of the host, supporting guest encapsulation.

The addition of excess C_{60} (5 equiv) to a CD_3CN solution of [coronene$_2$ $\subset$ **1**] resulted in complete displacement of the coronene in favor of C_{60}: [C_{60} $\subset$ **1**] was the only product observed by ^{1}H NMR and ESI-MS following 12 h at 323 K. Therefore, we infer that C_{60} binds more strongly within **1** compared to coronene, possibly due to a better size and shape match between the host cavity and the spherical guest, resulting in maximization of favorable $\pi - \pi$ interactions. Of course, there is also an entropic preference for a 1:1 host-guest complex *versus* a 1:2 alternative.

The addition of any of the smaller PAHs perylene, pyrene, or triphenylene (Figure 3.2.3) to **1** resulted in host occupation by a guest that was observed to exchange rapidly between free and bound states on the NMR time scale. This behavior was signaled by small shifts to the ^{1}H NMR resonances of **1** and broadening of some host peaks, along with upfield shifts in the guest signals (supporting information Figures S57-S59). ESI mass spectra of the host-guest mixtures displayed multiple (guest)$_n$ $\subset$ **1** ($n =$ 0-4) adducts. These guests are inferred to be too small to bind tightly within the cavity of **1**. Fast-exchange binding was also observed for aliphatic diadamantane (supporting information Figure S60) while no evidence of interaction was observed between **1** and triptycene, tetracene, or 1,4,5,8-naphthalene tetracarboxylic dianhydride.

We also investigated cage **1** as a host for asymmetric natural-product molecules and derivatives. Steroid derivatives were chosen for initial studies due to their importance in biological systems and as therapeutic agents, as well as their known ability to form complexes with aromatic substrates in the solid state.[250] The addition of cholesterol (1 equiv) to a solution of host **1** in CD_3CN (1 mM) gave a single set of cholesterol resonances, shifted upfield by up to 1.1 ppm relative to those of free cholesterol (Figure 3.2.6a). This observation is consistent with host-guest complexation in fast exchange on the NMR time scale. The host signals were also broadened, and additional peaks were observed in the imine region, consistent with desymmeterization as a result of

interaction with the asymmetric guest. The ^{1}H DOSY NMR spectrum of the mixture confirmed that all aromatic signals belong to cage **1**. The diffusion coefficients of the cholesterol resonances were reduced relative to those of the unbound guest, consistent with binding to host **1** under fast exchange on the NMR time scale (supporting information Figure S63). The addition of excess C_{60} (5 equiv) to the mixture of **1** and cholesterol resulted in complete conversion to $[C_{60} \subset \mathbf{1}]$, with the cholesterol resonances returning to chemical shifts characteristic of the free guest, providing further evidence for binding of cholesterol within the cavity of **1** (supporting information Figure S62) rather than through interaction with the exterior of the cage. A Job plot (supporting information Figure S64) suggested that a 1:1 binding stoichiometry dominates at 1 mM concentration.

Upon titration of cholesterol into a solution of **1**, its imine signals were observed to disperse and shift downfield, with different signals showing variable degrees of response to the presence of the guest (Figure 3.2.6b). Three signals were sufficiently sharp and separated from the others for their chemical shifts to be monitored and fit to 1:1 binding isotherms, giving association constants of $1.0 \pm 0.2 \times 10^3$ M^{-1} and $1.6 \pm 0.5 \times 10^3$ M^{-1} from peaks tentatively assigned to the C_3 isomer and $5 \pm 1 \times 10^3$ M^{-1} from the peak for the T isomer (supporting information Figures S67-S69). As with fullerenes, these results are consistent with the different diastereomers of **1** contributing differentially to the binding of cholesterol. The errors in the calculated association constants, however, preclude certainty.

The steroidal hormones progesterone and testosterone as well as the synthetic derivative fludrocortisone also bound within **1**, as inferred from clear shifts in the ^{1}H NMR spectra of the guests (supporting information Figures S70-S72) in the presence of **1**, indicating that this cage shows promise as a host for a variety of steroids. In each case the chemical shift changes were more modest than those observed for cholesterol,
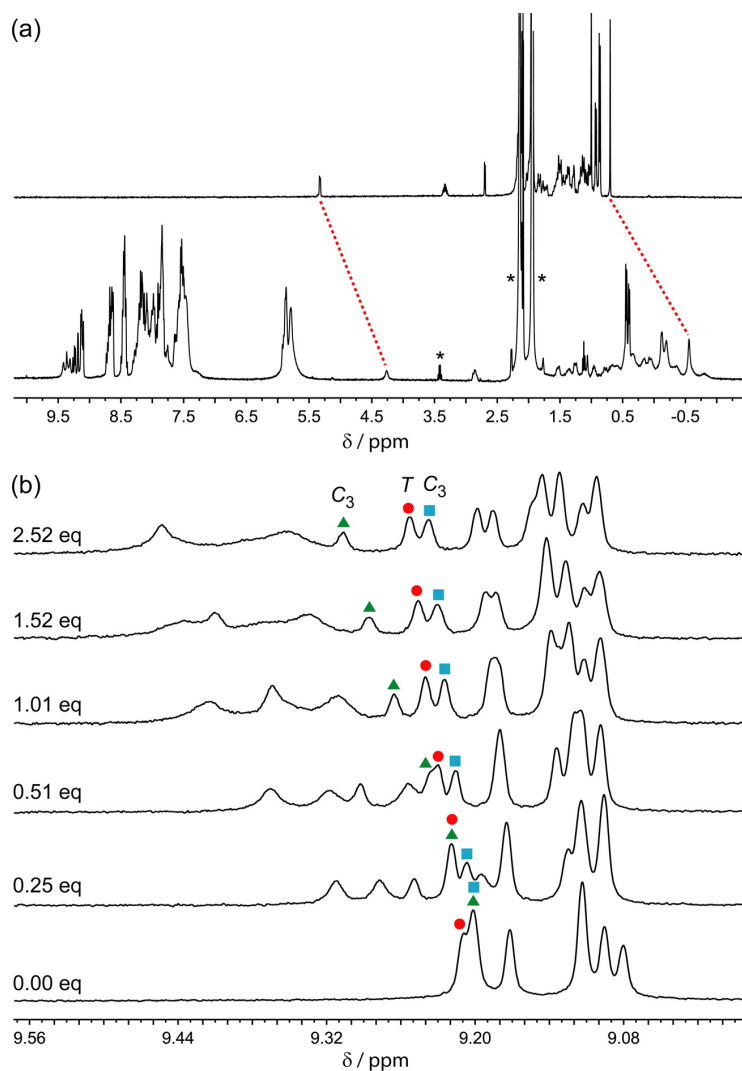
Figure 3.2.6: (a) Bottom: ^{1}H NMR spectrum (400 MHz, 298 K, CD$_3$CN) of a mixture of **1** (1 mM) and cholesterol (1 mM). Top: ^{1}H NMR spectrum (400 MHz, 298 K, CD$_3$CN) of cholesterol (1 mM). Shifts in selected cholesterol signals are marked with red dashed lines, and solvent peaks are marked by an asterisk. (b) Expansion of the imine region of the ^{1}H NMR spectrum (400 MHz, 298 K, CD$_3$CN) of **1** following the progressive addition of 0-2.52 equiv of cholesterol. Chemical shifts that were fit to 1:1 binding isotherms are marked with green triangles, red circles, and blue squares.

suggesting that **1** is a weaker host for these more polar steroids. Intriguingly, no evidence of interaction was observed with androsterone and estradiol, despite the chemical similarity of these steroids to those observed to bind within **1**.

Fast-exchange guest binding was also observed for the alkaloid strychnine, although ^{1}H NMR chemical shift changes upon guest binding were less pronounced for this smaller guest (supporting information Figure S73).

Host-Guest Chemistry of Cage 2

Cage **2** was investigated as a host for each hydrophobic guest that was observed to bind within **1** (Figure 3.2.3). However, in all cases no encapsulation was inferred to have taken place, as the ^{1}H NMR signals for **2** appeared at the same chemical shifts as in the absence of the guest and the signals for all acetonitrile soluble guests were identical or very close[c] to those in the absence of host. We infer the marked reduction in guest binding ability of cage **2** compared to **1** to be due to the cavity of **2** not being sufficiently enclosed to constrain potential guests inside.

3.2.3 Conclusions

In conclusion we have shown that two isomeric pyrene-edged cages show very different host-guest properties depending on the arrangement of the pyrene groups around the surface of the tetrahedron. Cage **2**, based on a 2,7-pyrene scaffold with an open cavity, was not observed to bind neutral guests. In contrast, isomeric cage **1**, based on a 1,6-pyrene scaffold, is able to provide a well-enclosed cavity and is a good host for large aromatic and hydrophobic guests, demonstrating the importance of cavity enclosure for strong host-guest interactions. This cage was shown to adapt when binding fullerenes, amplifying the diastereomers best able to bind the guest in order to maximize binding

---

[c] In some cases small shifts were observed in the guest signals. In all cases these shifts were at least an order of magnitude less than those observed when the guest was bound by cage **1**.

affinity. DFT analysis provided insights into the origin of this adaptive response, which is primarily driven by differential distortion energies required to transform free host geometries to those geometries required to encapsulate guests. In addition to binding symmetric guests, cage **1** also displayed binding affinity for steroid derivatives, allowing these asymmetric guests to be bound without the need to design an asymmetric host. Future work will investigate whether the reactivity of these guests can be altered through encapsulation.

3.2.4 Methods

Computational Methods

All calculations were performed using the PBE-D3 density functional[13, 176] with Becke-Johnson damping[14] as implemented in the TURBOMOLE 6.4 software package. Initial structures for each of the diastereomers of **1** were arranged so that all of the pyrene moieties were approximately equivalently disposed, but over the course of optimization, some of the pyrenes in the empty C_3 and S_4 isomers rotated. As a result, the final structures for the C_3 and S_4 isomers and their host-guest complexes have ratios of 3:3 left-to-right flipped pyrene moieties.

The heteroatom-polarized split-valence MIDI! basis set[237] was used for H, C, and N atom types, and the def2-TZVP basis set[238, 239] for Fe atoms. A resolution of the identity procedure was employed, using the def2-TZVP fitting basis implemented in TURBOMOLE[232–236] for Fe atoms and def-SVP[251] for H, C, and N atom types. The MIDI! and def-SVP fitting basis sets were employed to keep the calculations (particularly of the host-guest complexes) tractable.

One consequence of the large sizes of the various structures was that the standard convergence criteria for geometry optimization in TURBOMOLE[232–236] were generally found to be too strict to be practical. Consequently, more lenient convergence criteria

were employed, namely, the energy was required to change by less than 0.4 kJ mol^{-1} cumulatively over the course of five consecutive geometry-optimization steps.

General

Unless otherwise specified, all starting materials were purchased from commercial sources and used as supplied. NMR spectra were recorded on a Bruker DRX-400, Bruker Avance 500 Cryo, and a Bruker 500 TCI-ATM Cryo. ^{1}H chemical shifts (δ) are reported in parts per million (ppm) and are reported relative to the solvent residual peaks. ^{19}F chemical shifts (δ) are reported relative to hexafluorobenzene at -164.9 ppm. Low-resolution electrospray ionization mass spectra (ESI-MS) were obtained on a Micromass Quattro LC and high-resolution mass spectra acquired using a Thermofisher LTQ Orbitrap XL.

General Procedure for Host-Guest Investigations

A solution of **1** or **2** in CD$_3$CN (1.0-3.0 mM) was transferred to an NMR tube, and the prospective guest molecule (typically ∼5 equiv) was added as a solid. The mixture was sonicated for 10 min and allowed to equilibrate for at least 24 h at 298 K prior to measurement of the NMR and mass spectra. Characterization of the resulting host-guest complexes is given in the supporting information.

Chapter 4

Metal-Organic Frameworks as Supports

for Heterogeneous Catalysts

4.1 Sintering-Resistant Single-Site Nickel Catalyst Supported by Metal-Organic Framework

4.1.1 Introduction

Supported catalysts, composed of small metal/metal-oxide crystallites well dispersed on porous solid materials, play essential roles in a plethora of industrial gas-phase catalytic reactions including steam reforming, Fischer-Tropsch, and Haber-Bosch processes.[252–254] Solid supports such as porous activated carbon[255] or zeolites[256] are commonly used to increase the number, and/or enhance the activity ("support effects"), of candidate catalysis sites, thereby boosting the overall efficiency of a catalyst.[254] As compared to conventional supports, the structures of MOFs,[257–259] a class of porous materials comprised of organic linkers and inorganic nodes, are more readily tuned by rational ligand design, as evidenced by the vast number of unique structures[260] and by wide potential for applications in gas storage[261] and separation,[262] chemical sensing,[263] and catalysis.[264,265] Furthermore, using crystalline MOFs as supports provides opportunities for atomically precise structural characterization of both active sites and supports, thereby facilitating detailed mechanistic studies of reactions.[266]

Appropriately designed Zr-based MOFs hold great potential for use as solid supports in gas-phase catalysis due to their extraordinary thermal and chemical stabilities, as well as their substantial internal surface areas.[267] More importantly, it has been shown that these MOFs are readily modified post-synthetically to impart novel properties.[268] These functionalization processes, however, usually occur in solution phase, requiring laborious experimental procedures to remove trapped reagents and/or solvent.[268] Under certain circumstances, the ligation of solvent molecules to the coordinatively unsaturated metal

sites can lead to a distinct reduction in, or even a complete loss of, the desired functionalities,[269] necessitating delivery of modifying agents *via* the vapor phase. In fact, early reports demonstrated that a few "metal@MOF" materials could be obtained by using volatile metal complexes under sublimation-like conditions.[270] However, the lack of specific metal attachment sites in these MOFs, together with the non-self-limiting nature of sublimation, precludes precise control of the metal distribution within the frameworks and results in unstable and/or poorly defined hybrid materials. Thus, the metal atoms in these materials often agglomerate, leading to a reduction in the number of active sites and corresponding loss of catalytic activity.[270] With these challenges in mind, we set out to use atomic layer deposition in MOF, or AIM to incorporate catalytic metal oxides in a site-specific and atomically controlled fashion.[271] More critically, by isolating support sites from each other *via* lengthy organic spacers, we aimed to preclude metal atom/ion migration and catalyst sintering – an all too common mode of deactivation of metal catalysts on conventional supports, especially when the catalysis occurs at elevated temperatures and under a reducing environment.[252]

NU-1000, composed of $Zr_6(\mu_3\text{-}O)_4(\mu_3\text{-}OH)_4(H_2O)_4(OH)_4$ nodes and tetratopic 1,3,6,8-(p-benzoate)pyrene (TBAPy^{4-}) linkers, makes an excellent platform for AIM studies due to the readily accessible -OH/-OH$_2$ groups on the Zr$_6$ nodes (Figure 4.1.1).[272] We have previously demonstrated that the structurally well-defined -OH/-OH$_2$ groups on Zr$_6$ nodes[273] can behave as site-isolating grafting sites to control the positions of deposited metal ions.[274] Our target metal was nickel as it exhibits excellent catalytic activity for gas-phase alkene hydrogenation/oligomerization when dispersed on porous platforms.[275] In this report, we first detail our investigations on ethylene hydrogenation catalyzed by Ni-AIM as a proof-of-concept reaction to (i) demonstrate that AIM affords an effective strategy in producing single-site catalysts and circumvents active-site sintering during catalysis and (ii) validate our computational modeling protocols for

this new class of catalysts. Guided by theoretical predictions, we further investigated the potential of Ni-AIM for ethylene oligomerization, and our preliminary experimental results in this aspect are also presented herein.
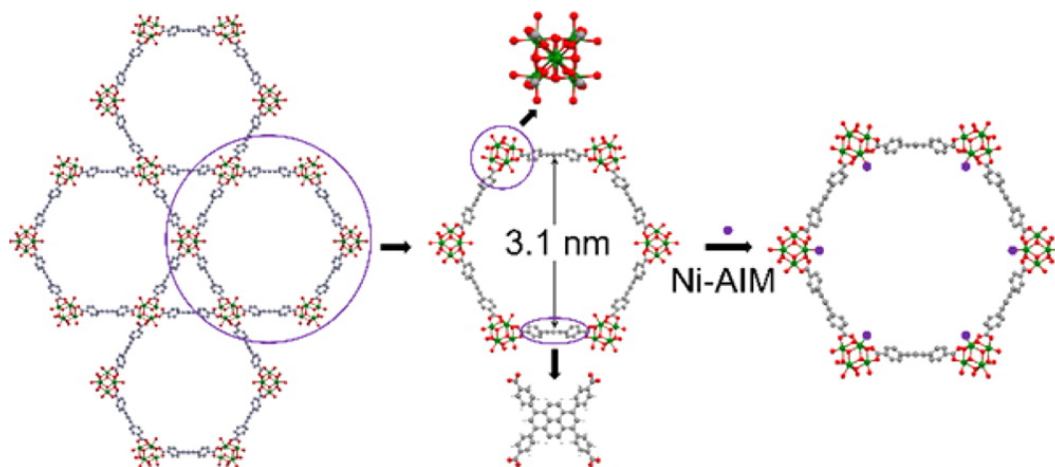
Figure 4.1.1: Structural representation of NU-1000, highlighting its organic linker, mesoporous channel, and Zr_6-containing node and a schematic depiction of the process used to anchor Ni to the Zr_6 node of NU-1000 *via* AIM. Color code: Zr (green), O (red), C (gray), H (white), Ni (purple).

4.1.2 Results and Discussion

The synthesis and characterization of Ni-AIM are detailed in the Methods section and supporting information. The as-synthesized material showed negligible ethylene hydrogenation activity over a temperature range of 50-200 °C. However, pretreatment in flowing 3% H_2/Ar at 200 °C renders the material catalytically active, with a per-nickel-atom turnover frequency (TOF) for ethylene hydrogenation of 0.9 ± 0.3 s^{-1} (Figure 4.1.2a). Notably, Ni-AIM is highly stable; e.g., with an initial ∼90% ethylene conversion, the deactivation of Ni-AIM was demonstrated to be minimal after 2 weeks' time

on stream, reaching a final steady state conversion of $\sim$80% (Figure 4.1.2b). Additionally, with only 68 mg of material, ongoing 100% ethylene conversion (flow conditions) was observed for 2 weeks with no detectable loss of activity. Exposing the catalyst to ambient atmosphere causes complete deactivation; however, the catalytic activity was fully restored by repeating the H_2 pretreatment at 200 °C for 5 h (Figure S1). The apparent activation barrier of the reaction was 8.3 $\pm$ 1.4 kcal mol^{-1} (Figure 4.1.2c), similar to other reported hydrogenation catalysts.[276] For comparison, a commercial Pt catalyst supported on alumina (5 wt %, 40% dispersion) and a lab-synthesized catalyst, Ni-ZrO$_2$, were tested under the same conditions. Being 4 orders of magnitude more expensive than nickel, the platinum catalyst has a TOF of 35 $\pm$ 8 s^{-1}. Prepared by ALD, Ni-ZrO$_2$ had an initial TOF of 0.6 s^{-1} but quickly and irreversibly deactivated (Figure 4.1.2d). The observed decay is a striking, but hardly atypical illustration of catalytically debilitating consequences of active-site migration and sintering. The hexazirconium(IV)-oxo, hydroxo nodes of NU-1000 present a chemically similar environment/support but with migration and sintering systematically blocked by organic linkers/spacers of about nanometer dimensions. The practical manifestation of blocking is the contrasting persistence of high catalytic activity illustrated in the panels b and d of Figure 4.1.2. Additionally, it was found that Ni-SiO$_2$ (preparation method is detailed in the supporting information) consists mainly of NiO particles (Figure S3), illustrating the difficulty in producing site-isolated catalysts, especially with a high density of active sites. Moreover, a higher temperature (400 °C) is required for its activation, under which circumstances the material became black in color, indicative of Ni nanoparticle formation. This is in line with the previous reports that metallic Ni supported on silica[277] and zeolites[278] is active for hydrogenation reactions but only after activation at high temperatures.

In situ X-ray absorption spectroscopy experiments were performed to investigate
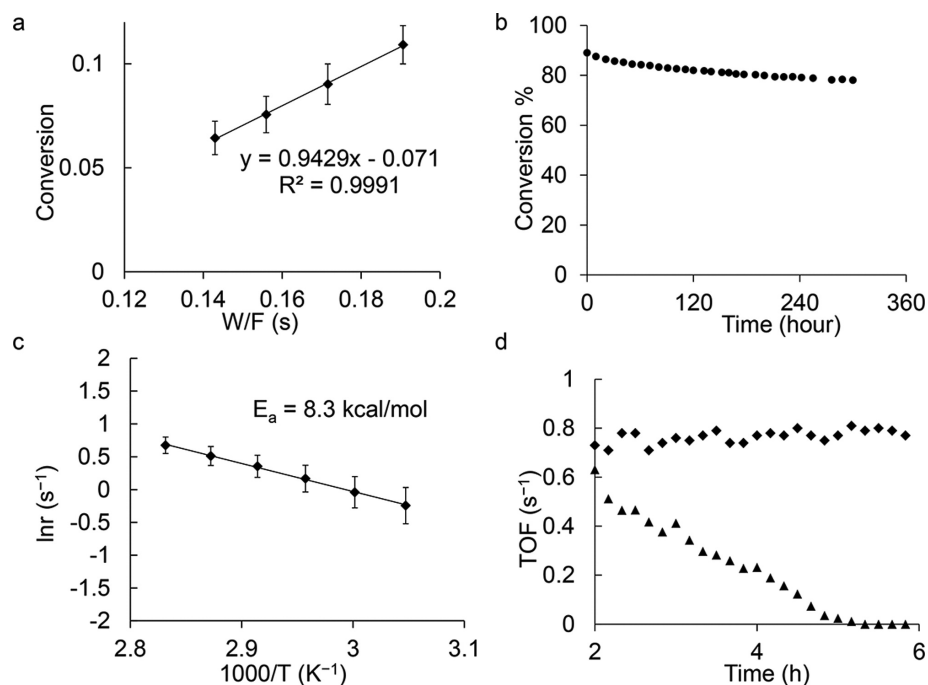
Figure 4.1.2: Catalytic conversion of ethylene to ethane. (a) TOF of the hydrogenation of ethylene catalyzed by activated Ni-AIM. (b) Stability test of activated Ni-AIM with initial 90% ethylene conversion. (c) Arrhenius plot of ethylene hydrogenation reaction rates by activated Ni-AIM. (d) Comparison of TOFs for Ni-AIM (diamond) and Ni-ZrO$_2$ (triangle).

the electronic and geometric structure of the Ni-AIM sites before and after activation with H$_2$ at 200 °C. X-ray absorption near edge structure (XANES) assessments of both the as-synthesized and activated Ni-AIM (Figure S2a) point to the retention of the Ni(II) oxidation state after the activation. We also observe a minor increase in XANES intensity $\sim$8342 eV upon activation corresponding to the region of the 1s-4p electronic transition. Overall the pre-edge region indicates that the majority of Ni species in the catalyst retains the original symmetry upon activation. From extended X-ray absorption fine structure (EXAFS) spectra, we observe that upon activation the intensity of the peak at a phase uncorrected distance of $\sim$1.6 Å (Ni-O scattering path) decreased, and

its position shifted slightly (Figure 4.1.3a and Figure S2b). Fitting this peak suggests a decrease of the average Ni first shell coordination number from 5.4 ± 0.6 to 5.0 ± 0.5. This decrease is accompanied by a decrease of the average Ni-O first shell bond distance from 2.056 and 2.033 Å (Figures S3-S5, Table S1). Both the XANES and the EXAFS results suggest some structural change upon activation – one consistent, as discussed below, with the formation of a small fraction of Ni hydride. EXAFS suggests that under reaction conditions this species likely exists as a transient state rather than a stable initial state.

Density functional theory (DFT) calculations were conducted to elucidate the reaction pathway of the Ni-AIM process (for details, see supporting information Figure S6). Given the experimental observation of four Ni atoms per Zr_6 node, we first examined the energetics of depositing one Ni atom at the node (**1**, Movie S1[a]) and then subsequently the energetics of depositing a second Ni atom at either another face of the node (**2**, Movie S2[a]) or the same face as the first Ni atom (**3**, Movie S3[a]). As shown in Figure 4.1.3, deposition of Ni atoms on separate faces is energetically (computationally) preferred by $\sim$10 kcal mol^{-1}. Two factors likely contribute to this energy difference: (i) removal of a proton from the μ_3-OH group to permit formation of a μ_3-O-Ni bond renders **1** the most stable structure for single-Ni tautomers, but each face presents only one μ_3-OH group, and (ii) depositing two Ni atoms on the same node face involves using the node μ_3-O atom on that face as a ligand to nickel – the μ_3-O atom is slightly displaced toward the center of the node core compared to the sitting of the μ_3-OH group (which is deprotonated to serve as a ligand to the first deposited Ni atom). Coordination of the second Ni atom to the inwardly displaced μ_3-O is sufficiently sterically demanding such that one external water ligand moves from the inner coordination sphere of the second

---

[a] Supporting information, including movies, can be found at: `http://pubs.acs.org/doi/suppl/10.1021/jacs.5b12515`

Ni into the second solvation shell, and this reduces the overall stability of the single-face dimer. Hence the isolated Ni model is used for DFT calculations of a plausible reaction energy pathway. Modeling the Ni atoms on separate faces allows for a direct evaluation of any cooperativity associated with the presence of the second metal. As the exothermicity required to deposit one Ni atom (-41.9 kcal mol^{-1}) is approximately half of that for the deposition of two adjacent Ni atoms (-86.8 kcal mol^{-1}), we conclude there is little communication between the faces, a situation similar to predictions for AIM reactions of NU-1000 nodes with Group 13 ALD precursors.[274]
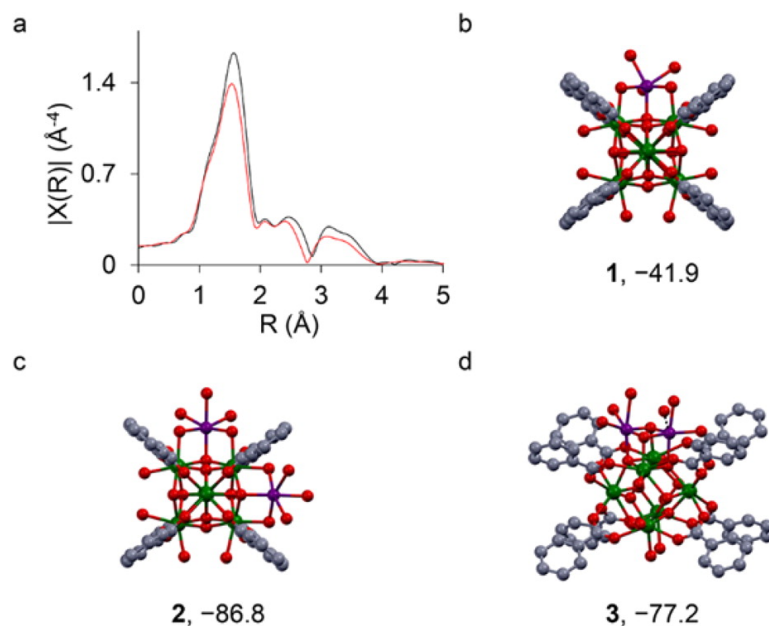
Figure 4.1.3: (a) EXAFS spectra of Ni-AIM before (black) and after (red) activation in 3% H_2/N_2 at 200 °C for 2 h; DFT calculated node structure for (b) one Ni atom per face model with one Ni atom included (-41.9 kcal mol^{-1}), (c) one Ni atom per face model with two Ni atoms included (-86.8 kcal mol^{-1}), and (d) two Ni atoms per face model (-77.2 kcal mol^{-1}). The enthalpies are relative to the reactants, *i.e.*, bare NU-1000 node, two Ni(MeC(Nt-Bu)$_2$)$_2$, and six water molecules.

The mechanism for catalytic ethylene hydrogenation was subsequently investigated

using the calculated species **1** (Figure 4.1.4). We predict that one -OH equivalent is protonated by H_2 and departs as water during the activation process, leaving a hydride in its place (Figure S7). The transition-state structure we identified, involving the reaction of H_2 with yet another tautomer, **4**, generates **5** and has a fairly high enthalpy (43.2 kcal mol^{-1}), consistent with the overall strongly endothermic nature of the reaction, and rationalizes the forcing conditions associated with Ni-AIM activation.[279]

Upon activation, the complex binds one ethylene molecule to generate **6** from **5** with concomitant loss of two water molecules, which is predicted to be endothermic by 15 kcal mol^{-1} (but is strongly favorable in a free-energy sense under conditions that remove the water). Subsequent migratory insertion to generate the ethyl-nickel species **7** occurs with a low activation enthalpy of 3.7 kcal mol^{-1} and is exothermic by 12.0 kcal mol^{-1} once the initial loss of water ligands occurs. Subsequent binding of H_2 to **7** generates **8**, which then reacts to liberate ethane and generate the tetracoordinate nickel hydride species **9** with an activation enthalpy of 4.1 kcal mol^{-1} relative to **7** and an exothermicity of 4.9 kcal mol^{-1}. It is unclear whether this portion of the catalytic reaction is stepwise or concerted. While **8** exists as a minimum on the potential energy surface, the loss of zero-point vibrational energy associated with the binding of H_2 places **8** slightly higher in enthalpy than **7**. From an enthalpic standpoint, one might consider the production of ethane to proceed *via* the direct route from **7** to **9**. Nonetheless, both reaction pathways are predicted to proceed with very low activation enthalpies, leading to a very efficient catalytic cycle (Figure 4.1.4). Including a factor of RT at 373 K to convert an enthalpy of activation to an Arrhenius activation energy, the predicted value of 4.9 kcal mol^{-1} for the rate-determining step is slightly below the lower error bar on the measured value (*vide supra*), but we deem the agreement satisfactory given the limitations associated with modeling the MOF as a truncated cluster. We note, however, that while the Ni-AIM structure predicted from DFT calculations is consistent

with the observed chemistry exploring other possible Ni-coordination motifs that may have similar energy minima is currently an active area of theoretical and experimental research.

The prediction of a Ni-H species in the hydrogenation process prompts us to target the ethylene oligomerization reaction as this intermediate is also involved in the mechanistic step for Ni-catalyzed alkene oligomerization.[280] Developing light alkene oligomerization catalysts has attracted tremendous industrial and academic interest in recent years since high-valued hydrocarbons such as gasoline, diesel fuel, lubricants, and surfactants can be produced *via* this process.[275] By the addition of $(CH_3CH_2)_2AlCl$, Ni-AIM becomes active for ethylene oligomerization at 45 °C and 2 bar pressure, with an estimated initial TOF of 0.3 s^{-1}. During the first 10 h on stream the catalyst deactivates, which is attributed to the formation of polymeric products (*vide infra*). Thereafter, a constant ethylene conversion is observed with the products being C_4, C_6, and C_8 (for product distributions, see Table S2). A series of detailed kinetics measurements were conducted in a similar fashion to the hydrogenation process, revealing a TOF of 0.07 ± 0.01 s^{-1} and an activation barrier of 8.5 kcal mol^{-1} (Figure 4.1.5), outperforming another reported MOF-based alkene oligomerization catalyst.[281]

4.1.3 Conclusions

With high activity, long-term stability, and excellent regenerability, the Ni-AIM material presented is one of the best available hydrogenation catalysts based on earth-abundant elements. Detailed structural analysis confirms that AIM affords an effective strategy to produce stable single-site catalysts because (i) there are strong interactions between the deposited metal ions and the Zr_6 node and (ii) the organic ligands that are used to construct the MOF can prevent the metal ions from migration and agglomeration. In addition, the molecular nature of the MOF support allows for the detailed characterization
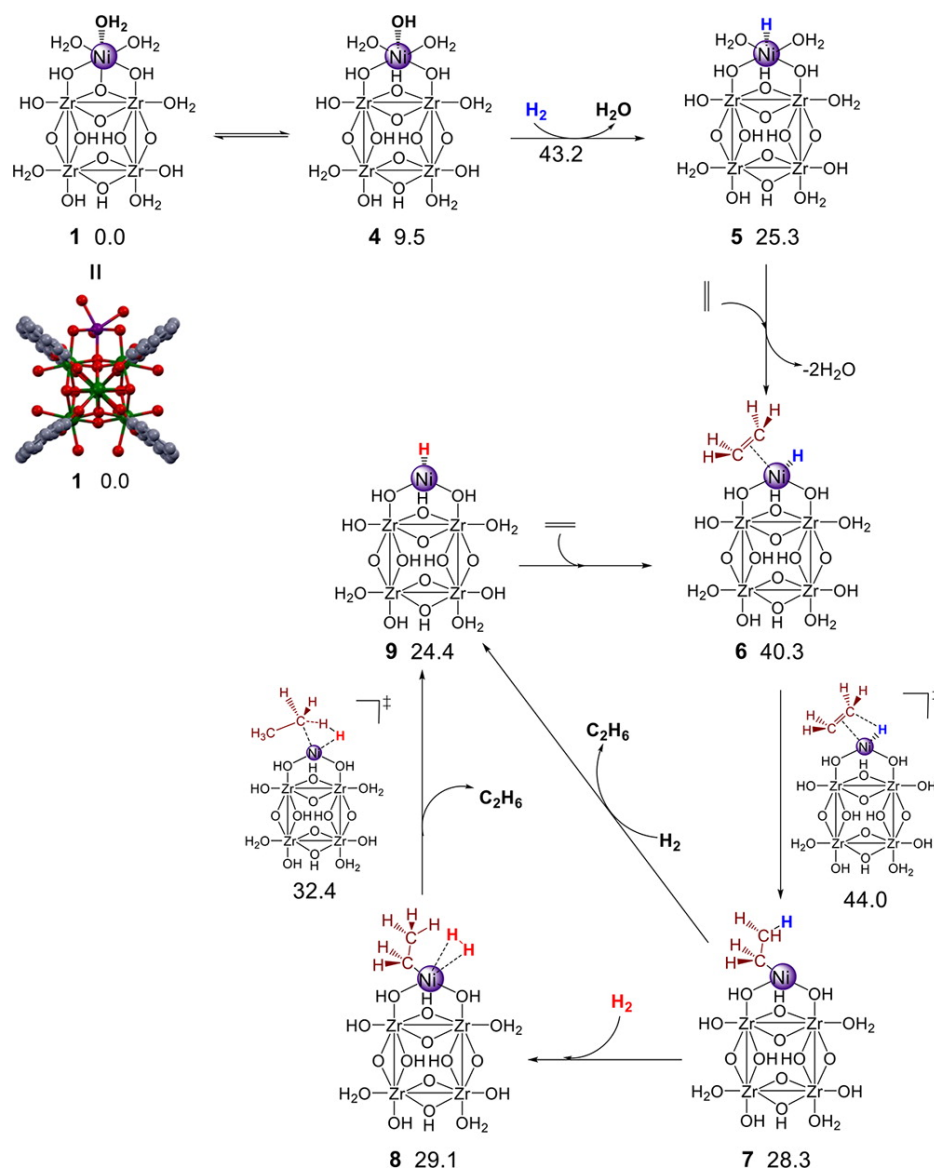
Figure 4.1.4: DFT-calculated enthalpies (kcal mol^{-1} relative to each reactant, *i.e.*, **1**, 2 H$_2$, and H$_2$C=CH$_2$) for intermediates and transition state structures associated with Ni activation and single-turnover catalytic hydrogenation of ethylene (simplified for one Ni per node). For clarity, the benzoate ligands and the apical Zr atoms of the MOF are not shown.
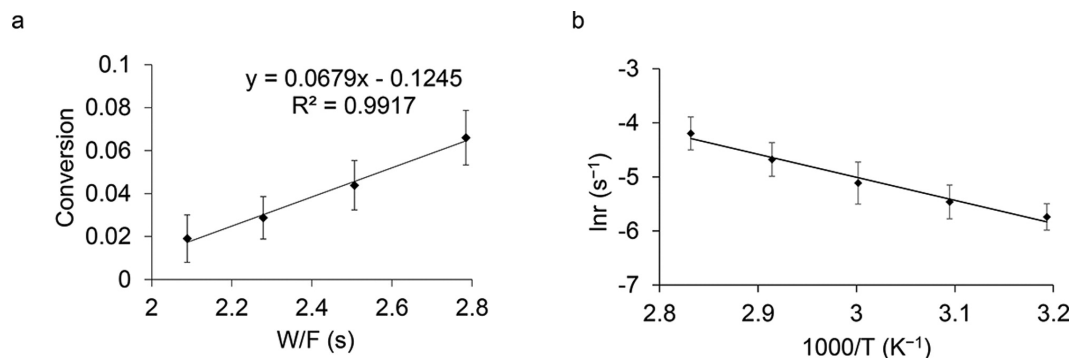
Figure 4.1.5: Catalytic conversion of ethylene oligomerization. (a) TOF of the oligomerization of ethylene catalyzed by activated Ni-AIM. (b) Arrhenius plot of ethylene oligomerization reaction rates by activated Ni-AIM.

of the catalyst, providing a convenient platform for detailed mechanistic investigations of the catalytic cycle computationally. Of greater interest, with the validation of computational modeling protocols by the hydrogenation process, we successfully predicted and achieved the oligomerization process catalyzed by Ni-AIM. Further efforts involving the detailed mechanistic study of the oligomerization reaction are currently in progress.

4.1.4   Methods

Computational Details (Reproduced from the Supporting Information)

All calculation were performed using the mix-node topology of NU-1000, $[\mathrm{Zr}_6(\mu_3\text{-O})_4(\mu_3\text{-OH})_4(\mathrm{H}_2\mathrm{O})_4(\mathrm{OH})_4]^{8+}$,[273] with the M06-L density functional[11,104] in Gaussian '09.[56] An automatic density-fitting set generated by the Gaussian program was used to reduce the cost of calculations.

Calculations for the ALD process were performed on a single Zr_6 node with linkers truncated to benzoate groups. During geometry optimization, the carbon atoms of the truncated linkers were kept fixed in order to simulate the structural rigidity of the

framework. The 6-31G(d) basis set[55] was employed for H, C, N, and O atom types during geometry optimization, along with the SDD basis set and pseudopotential[54] for Ni and Zr atom types. Thermal corrections to enthalpies were derived from vibrational frequency calculations performed at the same level of theory.

During the ALD process the organic linker of the MOF were kept, due to the interaction with the bulky amidinate ligands from the Ni precursor. These linkers were reduced to formate groups during the catalytic cycle of ethylene hydrogenation, where the steric interactions with the MOF linkers would not play a significant role. Consequently, the benzoate groups of the linkers were truncated further to formate groups, and a larger basis set was employed to improve the accuracy of the calculations. The Def2-SVP basis set was used for H, C, and O atom types, and the Def2-TZVP basis set for Ni and Zr atom types.[238] Ni atoms were treated with an all-electron basis set,while Zr atoms were treated with the SDD pseudopotential, as in the computations related to the ALD process. The nature of all stationary points was again verified by analytical computation of vibrational frequencies.

4.1.5 Acknowledgments

4.2 Computationally-Guided Discovery of Active Cobalt-Decorated Metal-Organic Framework for Ethylene Oligomerization

4.2.1 Introduction

The heterogenization of molecular catalysts, where the role of the solid support is analogous to a ligand, has emerged as one of the frontiers in modern catalysis to improve catalyst stability and broaden reaction scope while preserving, or even enhancing, catalyst tunability and activity-selectivity profile.[253,282,283] For this purpose, porous materials such as silica, zirconia, zeolites, and metal-organic frameworks, inter alia, are used as supports.[283-288]

Metal-organic frameworks (MOFs) are porous materials with a well-defined crystalline structure formed by metal ions or clusters connected in three dimensions by multitopic organic linkers.[289] Due to the wide variety of metal nodes and linkers, tunability and rational design can inform MOF synthesis. As a result, MOFs have found use in many processes, such as gas separation, gas storage, and catalysis,[281,290-292] and recently they have emerged as highly promising heterogeneous supports for incorporating transition-metal-based catalysts.[282,293] Heterogeneous catalysis in a MOF provides an opportunity to design isolated single-site catalysts that, by remaining isolated from one another (owing to the intervention of the MOF framework) resist loss of catalytic activity that might otherwise occur through sintering or rearrangement. In addition, detailed mechanistic studies are possible for single-site catalysts that are homogeneous in constitution.[294]

Recently, atomic layer deposition of metals in MOFs (AIM) and solution-based post-synthetic MOF functionalization have both been used to decorate MOFs with group

XIII metals, e.g., Al(III)[272,274] and In(III),[274] and also transition metals (TMs) such as, Fe(III),[293] Co(II),[295–298] Ni(II),[282,294,295,298,299] Cu(II),[295] Zn(II),[272,295] Zr(IV),[300] and Ir(I).[301,302] Both techniques allow for modification of the mesoporous material and the inclusion of potentially well-defined and catalytically active sites.

In terms of post-synthetic functionalization, the linkers of the MOF Fe-MIL-101, consisting of trimeric iron(III) octahedral clusters linked by 2-aminoterephthalate ligands,[303] have been functionalized with a Ni(II)L homogeneous catalyst by Canivet *et al.* that upon activation with diethyl aluminum chloride (Et_2AlCl) display a high activity for ethylene dimerization.[304] Another successful example involves the anchoring of a Ni molecular complex onto the inorganic Zr_6 node of the NU-1000 MOF. This material also acts as a catalyst for ethylene dimerization following activation with Et_2AlCl.[282]

The Zr_6-based NU-1000 node, $[Zr_6(\mu_3\text{-}O)_4(\mu_3\text{-}OH)_4(OH)_4(OH_2)_4]^{8+}$, is particularly suitable for the installation of transition metals *via* AIM or other post-synthetic functionalization methodologies owing to the reactive -OH and -OH_2 groups that decorate the node (Figure 4.2.1). NU-1000 derives from combining such nodes with the tetratopic 1,3,6,8-tetrakis(*p*-benzoate)pyrene linker, generating a MOF with high pore volume, as well as high thermal and chemical stabilities – all important characteristics for a single-site catalyst platform.[267,272–274,282,293–297,300–302]

NU-1000 is characterized by three distinguishable large pores, two of which are shown in Figure 4.2.1. The largest pore is associated with channels having a diameter of about 31 Å, facilitating the diffusion of reactants and products to and from reactive sites.[282,294] Perpendicular to the hexagonal pore the second largest pore located the *c*-axis present a separation between Zr-nodes of about 10 Å. The triangular microchannel depicted in Figure 4.2.1 represents the smallest pore with 8 Å diameter and lack of -OH/-OH_2 groups.

Improved molecular organometallic catalysts often emerge from extensive tuning of
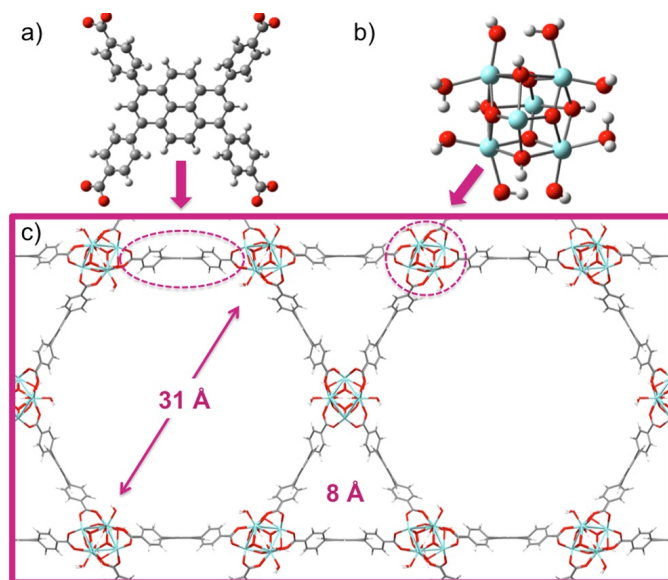
Figure 4.2.1: Schematic representation of NU-1000 MOF topology and Zr_6-based inorganic and organic building block (a) 1,3,6,8-Tetrakis(p-benzoic acid)pyrene linker, $TBAPy^{4-}$; (b) $[Zr_6(\mu_3\text{-O})_4(\mu_3\text{-OH})_4(OH)_4(OH_2)_4]^{8+}$ node; (c) the Zr_6-based framework of the NU-1000; Color code: Carbon is gray; hydrogen is white; zirconium is cyan; and oxygen is red.

ligands to optimize their steric and electronic effects.[284] When a metal is anchored or grafted to a support such as a metal oxide, the same principles and methods apply.[284,301,302] Zr_6-based MOFs, such as UiO-66/67 and NU-1000, have been reported as good supports for $Ir(acac)(CO)_2$ and $Ir(acac)(C_2H_4)_2$ (acac = acetyl acetonate), which have catalytic activity for ethylene hydrogenation and dimerization. The iridium metal has been shown to be strongly influenced by the electronic properties of the underlying node.[301,302]

Recently, we installed Ni ions by AIM on the node faces in NU-1000, which we will hereafter designate as Ni-AIM+NU-1000.[294] Upon activation, this catalyst showed remarkable activity for ethylene hydrogenation and oligomerization.[294] A quantum

chemical characterization of a mononuclear catalytic site and the details of its ethylene hydrogenation cycle were presented. Ni-AIM+NU-1000 also showed promising catalytic activity for dimerization and oligomerization of ethylene.[294] There is substantial interest in the design of heterogeneous catalysts for selective ethylene dimerization, since this process is essential for the formation of high purity 1-butene, a precursor in the production of linear low-density polyethelene which is the most common plastic in everyday life.[305]

In this article we report a detailed investigation of three plausible mechanisms for ethylene oligomerization with a mononuclear Ni-AIM+NU-1000 catalyst, and we compare this catalyst to an isostructural mononuclear Co-AIM+NU-1000 assembly.[296] Multireference calculations on key transition states are presented and analyzed in order to understand how the coordination environment of the support influences the catalytic properties of the two transition metals. [As a point of nomenclature, we note that AIM as an experimental procedure can create M-AIM+NU-1000 products that contain mixtures of mono-, bi-, and polynuclear metallated nodes. Theory unambiguously addresses specific nuclearities by construction of the computational model, and in this section we will consider only mononuclear metallated nodes, noting that this does not preclude the possibility of additional catalytic activity from bi- and polynuclear sites in experimentally prepared samples.]

4.2.2 Models and Computational Details

Cluster model. All calculations were performed starting from the mix-S topology of the Zr_6-NU-1000 node, $[Zr_6(\mu_3\text{-O})_4(\mu_3\text{-OH})_4(OH)_4(OH_2)_4]^{8+}$, reported by Planas *et al.*[273] The Zr_6 node of NU-1000 was modeled as a finite cluster extracted from an optimized periodic unit cell to allow a detailed investigation of the supported M^{2+} (M = Co and Ni) complexes. The organic linkers were modeled as benzoate (150-atom cluster)

and formate (70-atom cluster) groups when studying deposition and oligomerization mechanisms, respectively (Figure 4.2.2).[273, 301]
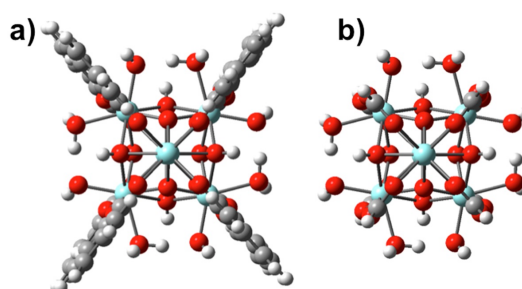
Figure 4.2.2: Schematic representation of (a) benzoate and (b) formate cluster model used to calculate the AIM process and oligomerization mechanism, respectively. Color code: Carbon is gray; hydrogen is white; zirconium is cyan; and oxygen is red.

Kohn-Sham density functional calculations. Clusters were optimized using the M06-L[11] density functional as implemented in the Gaussian '09 software package,[56] together with the def2-SVP basis set for C, H, and O atoms, and the def2-TZVPP[238, 239] basis set for Co, Ni, and Zr atoms. Associated effective core potentials were used on Zr atoms. In all cases, the positions of all atoms were optimized, except for the C and H atoms of the capping benzoate and formate groups. The nature of all stationary points was verified by analytical computation of vibrational frequencies, which were also used to compute 298.15 K thermochemical quantities.

Multireference calculations. The key reactive intermediates identified by density functional theory (DFT; *vide infra*), ethyl-M-AIM+NU-1000 (**1**, M = Co or Ni) and ethylene bound to **1** (**2**) and the first C-C bond formation transition states (**TS2-3**) of cycle III for Co-AIM+ and Ni-AIM+NU-1000 were further characterized at the complete active space self-consistent field (CASSCF) level of theory, followed by second order perturbation theory (CASPT2) calculations.[306] All CASSCF calculations were performed with the MOLCAS-7.8 package[307] for the M06-L optimized geometries, using

the all-electron ANO-RCC basis sets.[308,309] In all of these calculations, the triple-zeta quality ANO-RCC-VTZP basis set was used for Co and Ni, the double-zeta quality ANO-RCC-VDZP basis set was used for O and Zr, and the minimal ANO-RCC-MB basis set was chosen for the C and H atoms. Scalar relativistic effects were included by using the Douglas-Kroll-Hess Hamiltonian.[310] Two-electron integral evaluation was simplified by employing the Cholesky decomposition technique.[311]

In the CASSCF/CASPT2 calculations, an active space of n electrons in m orbitals (n,m) was used for all species, where n is the number of $3d$ electrons for the mononuclear catalyst TM, together with the electrons in substrate C-C π bonds (two electrons per ethylene molecule). In order to reduce the computational cost, we designed a small cluster of 43 atoms for **1**, and 49 atoms for **2** and **TS2-3**, respectively. These clusters included the first coordination sphere of the Co and Ni atom and two proximal Zr atoms connected as supports. Terminal hydrogen atoms were added to keep charge neutrality; the positions of the added hydrogen atoms were optimized using the same level of theory as for the larger cluster (for more details, see supporting information).

4.2.3 Results and Discussion

Experimental evidence indicates that installation of Co(II) *via* AIM to produce Co-AIM+NU-1000 yields between one and four cobalt ions per Zr_6-node, where the loading of Co can be modified by changing certain experimental conditions.[295–297] In order to model the catalytic activity and compare with the nickel analogue, Ni-AIM+NU-1000, an idealized system was considered, where only one cobalt or one nickel atom was deposited onto one face of the Zr_6-node of NU-1000, thereby generating an isolated, single-site, mononuclear catalyst.[294,295] The most energetically favorable products from the AIM process as determined by DFT are intermediates **A** and **B** (Figure 4.2.3; a

similar computational procedure to that reported previously for following Ni(II) deposition was employed in this work for Co(II) (See the supporting information for more details)). These structures are pre-catalysts for ethylene oligomerization.

Ethylene Oligomerization Catalyzed *via* a Single-Site Co(II) and Ni(II) Atom Deposited at the NU-1000 Node

Three plausible mechanisms for ethylene oligomerization were investigated and are summarized in Figure 4.2.3. Cycle I involves the generation of an active catalyst by C-H bond activation of ethylene to form a vinyl-metal species (with proton transfer to a coordinated oxide or hydroxide). Subsequent generation of α-olefins by consecutive ethylene insertion steps is followed by a proteolytic release at some point (regenerating the catalyst, **B**). In Cycle II, the potential formation of metallo-cyclic intermediates was also investigated, which begins with the binding of two ethylene molecules to **B** followed by generation of the new C-C bond through oxidative coupling.[312,313] The third mechanism, Cycle III, involves the pre-activation of the M-AIM+NU-1000 catalyst by Et$_2$AlCl, as previously reported for nickel functionalized MOFs acting as catalysts for ethylene oligomerization (*vide supra*).[282,294,304]

Cycle I is a Philips-type reaction,[286] and the calculated activation enthalpy, $\Delta H^{\ddagger}$, for this step proceeding from intermediate **A** (*i.e.*, with coordinated hydroxide that activates the ethylene C-H bond to form the vinyl group), is about 32 kcal mol^{-1} for Co-AIM+ and 27 kcal mol^{-1} for Ni-AIM+NU-1000.[b] The alternative addition to intermediate **B** involves the μ_3-O atom activating the ethylene C-H bond and activation enthalpies of 43 and 44 kcal mol^{-1} are computed for Co-AIM+NU-1000 and Ni-AIM+NU-1000, respectively. Although previously reported as a viable mechanism

---

[b] Note that we focus on enthalpies in most of our energetic discussion, as the corresponding free energies will depend on the partial pressures of reactant ethylene and product olefins. Our goal is to understand intrinsic bond-making/bond-breaking barriers, noting that entropic effects associated with reactant and product concentrations may be exploited under favorable conditions.
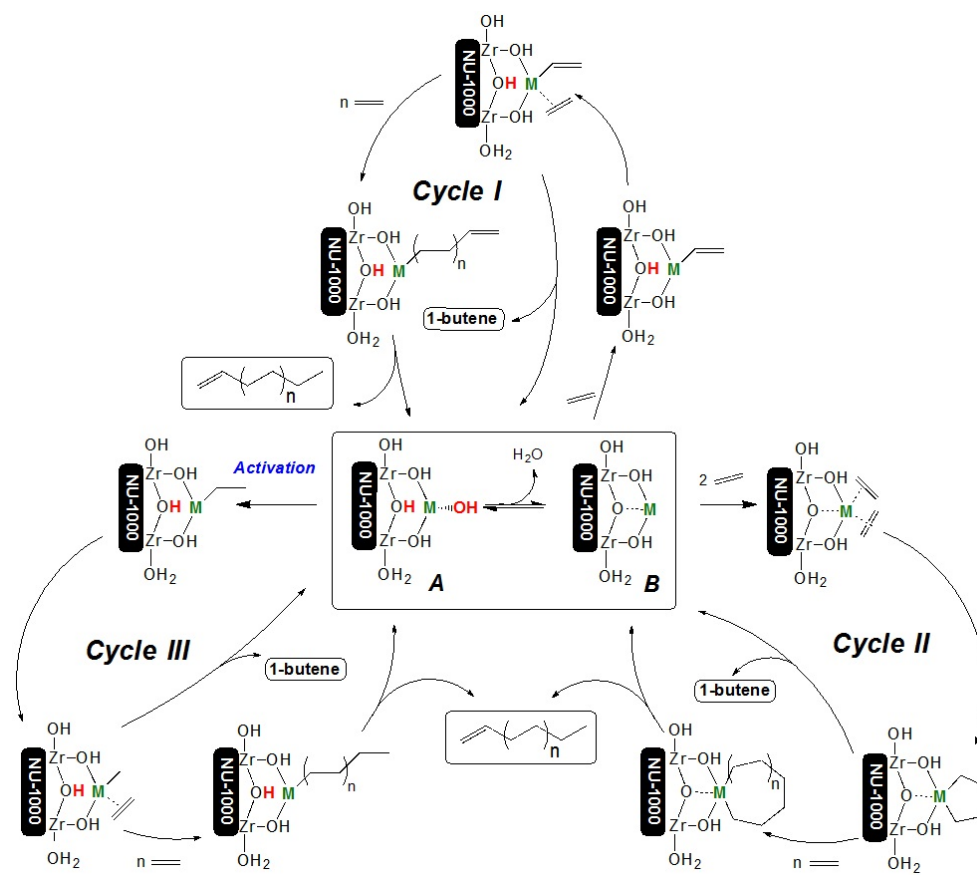
Figure 4.2.3: Schematic representation of three mechanistic pathways for ethylene oligomerization mediated by M-AIM+NU-1000, where M = Co(II) or Ni(II) metal. Linkers of the MOF are omitted for clarity.

for Cr-atom deposited on silica,[286] these $\Delta H^{\ddagger}$ are too high to make Cycle I accessible under relevant reaction conditions.

Cycle II involves Ziegler-Natta-like chemistry,[312, 313] with two coordinated ethylene molecules reacting to form a metallocycle. However, the activation enthalpies for this oxidative cyclization are 35 and 42 kcal mol^{-1} for Co-AIM+ and Ni-AIM+NU-1000, respectively. As the metal oxidation state formally increases from 2 to 4 for this step, its overall poor kinetic favorability is unsurprising. More detailed descriptions of cycles I and II that include full characterization of all relevant stationary points are provided in the supporting information.

In Cycle III (Scheme 4.2.1, Figure 4.2.4), alkylation of intermediate **A** with Et$_2$AlCl generates tetracoordinate M(II) species **1**, which readily coordinates ethylene in a π complex. The resulting intermediate **2** is lower in enthalpy than the separated reactants by 12 and 19 kcal mol^{-1} for Co and Ni, respectively. Insertion of ethylene into the existing metal-carbon bond forms **3** with its extended alkyl chain. This process can repeat to oligomerize ethylene. Consequently, β-hydride elimination to generate **4** can occur, after which ethylene may substitute the coordinated α-olefin, leading to intermediate **5**. Metal-hydride addition across the double bond regenerates **1**, which may then re-enter the oligomerization cycle. Selected bond lengths of the first coordination sphere of the metal center in intermediate **1** are showed in Figure 4.2.5. These intermediates present similar geometries for the two metals. However, compared to Ni, Co presents shorter bonds with the terminal -OH groups, and longer bonds with the μ_3-OH and C(ethyl).

The energetics associated with all of these steps are summarized in Figure 4.2.4 for Ni-AIM+ and Co-AIM+NU-1000. In each case, the rate-determining step is insertion, with activation enthalpies of 24.1 and 15.6 kcal mol^{-1} to go from **2** to **3** for Co and Ni, respectively. It is apparent that Ni-AIM+NU-1000 is therefore a considerably more
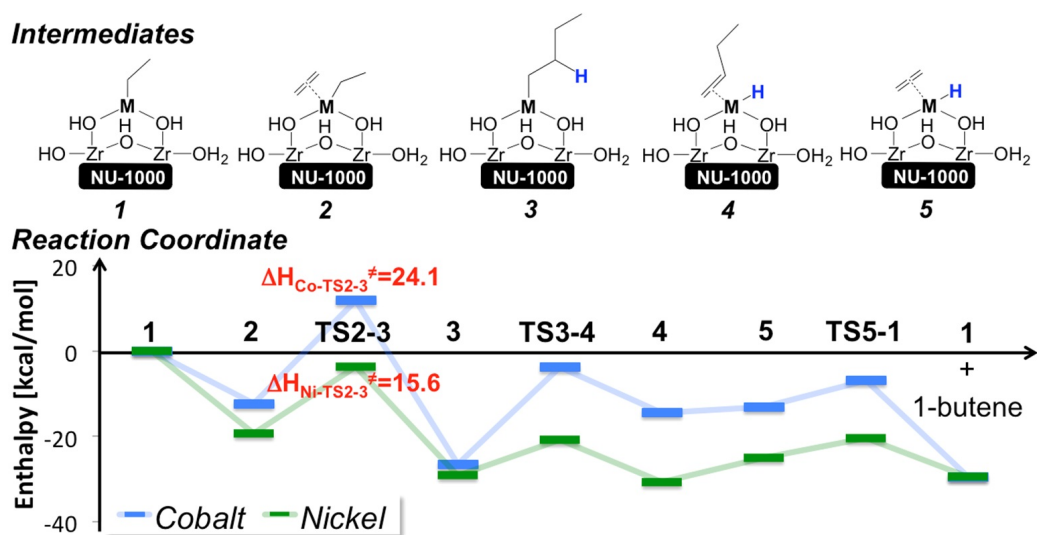
Figure 4.2.4: Computed enthalpies (298.15 K, in kcal mol^{-1}) for stationary points along reaction coordinate for ethylene dimerization catalyzed by M-AIM+NU-1000 (M = Co or Ni). Note that the energy presented for **5** includes the product liberated (1-butene) energy.
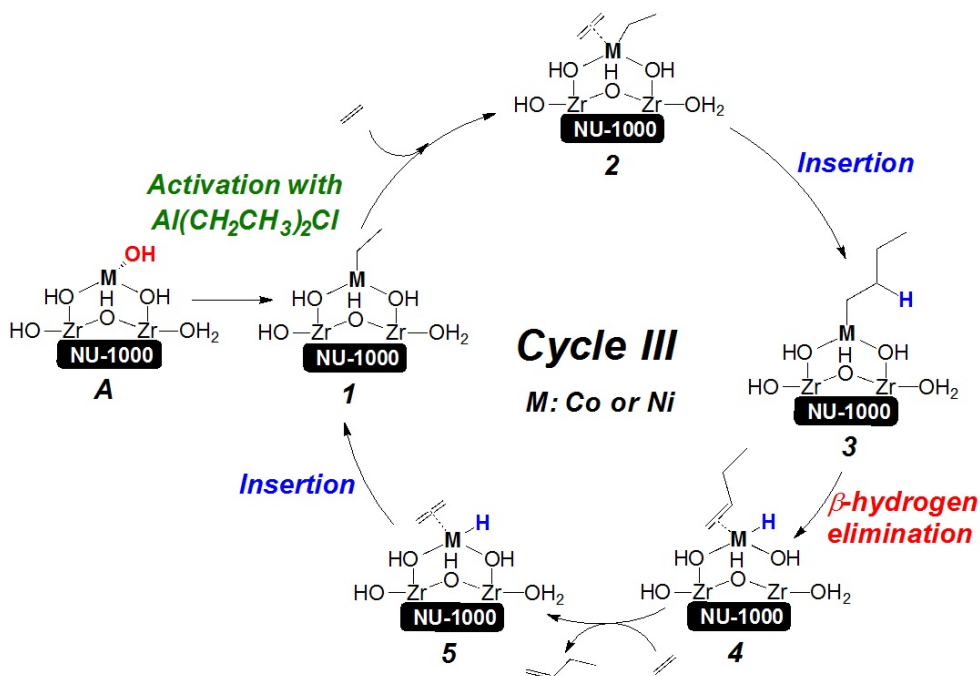
Scheme 4.2.1: Cycle III

effective catalyst than Co-AIM+NU-1000.

A key difference between the two catalysts is the electronic configuration of the transition metal: $3d^7$ for Co(II) and $3d^8$ for Ni(II). The Co(II) species can have either one or three unpaired electrons, giving rise to doublet and quartet states. The Ni(II) species, by contrast, must adopt singlet or triplet electronic states. This difference in electron count has a profound influence on the geometries associated with the rate-determining transition-state (TS) structures, as shown in Figure 4.2.6. Co(II) has a penta-coordinated environment that is approximately trigonal bypyramidal: the metal interacts with three oxygen atoms of the node (one μ_3-OH (apical) and two terminal -OH groups (equatorial)), the ethyl group (apical) and the reacting ethylene molecule (equatorial). By contrast, the Ni(II)-AIM+NU-1000 species is effectively square planar,
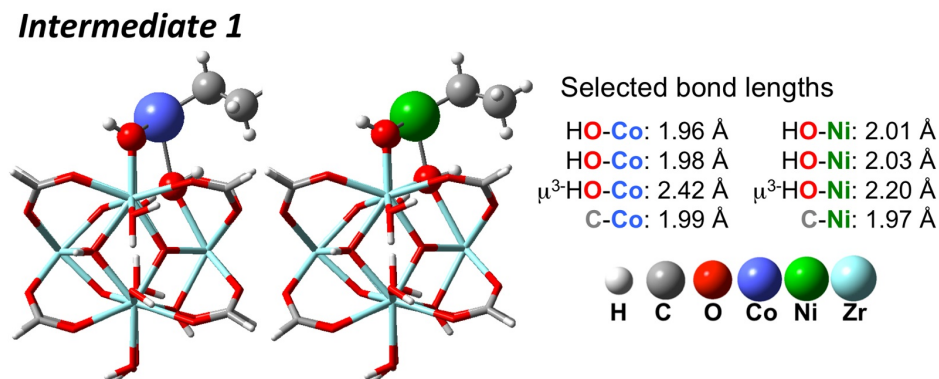
Figure 4.2.5: Intermediate **1** for Co(II) (in blue) and Ni(II) (in green).

lacking any significant interaction with the μ_3-OH group and organizing the hydrocarbon groups trans to the remaining hydroxyls on the node.

Analysis of the Electronic Configuration by Multireference Methods

The most relevant CASSCF molecular orbitals (MOs) for the rate-determining TS structure **TS2-3** of cycle III are presented in Figure 4.2.7 for Co-AIM+ and Ni-AIM+NU-1000. The frontier $(C_2H_4\text{-}2p)_2$ MO is a combination of the $2p$ orbitals of the reactive carbon atoms, *i.e.*, the π bond of the ethylene, where one of the two p orbitals is being redirected as the forming bond to the ethyl group. This orbital is stabilized through some degree of hybridization with the $3d$ orbitals of the coordinating metal. For the Ni case, there are four doubly occupied $3d$ orbitals. The fifth, formally empty d orbital, hybridizes strongly (48%) with the $2p$ orbitals of the reactive carbon atoms (52%) (Figure 4.2.7). By contrast, the high-spin configuration of Co leaves the appropriate d orbital half-filled and thus substantially less prone to stabilize the TS structure through hybridization with the $(C_2H_4\text{-}2p)^2$ MO; the CASSCF frontier MO has only a 15% Co $3d$ orbital contribution. This key difference in the ability of the two metal centers to
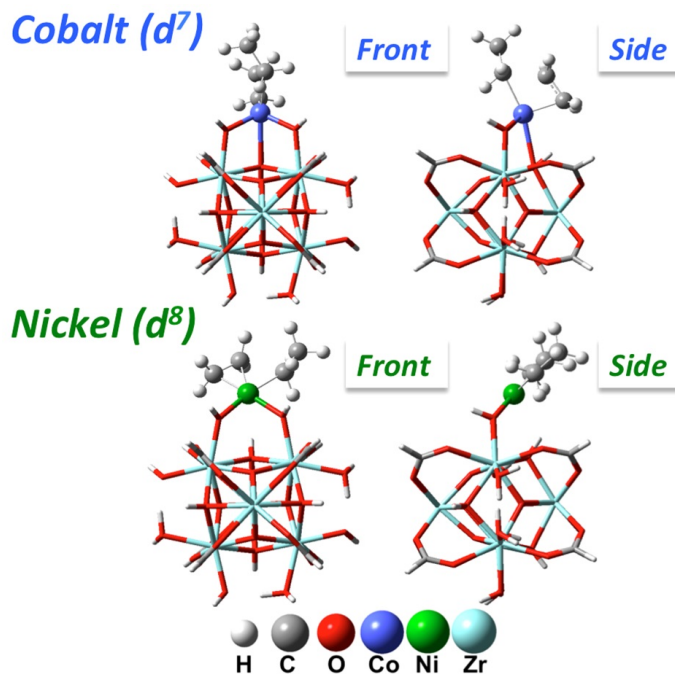
Figure 4.2.6: Rate-determining TS structures **TS2-3** for Co(II) (blue, quartet, trigonal bipyramidal) and Ni(II) (green, singlet, square planar).

stabilize the C-C bond-forming TS structure explains the enhanced catalytic activity of the Ni (for further details of the overall electronic structures, see the supporting information).

Propagation *versus* Termination Steps

In order to assess the likely formation of longer α-olefin chains, we compared the relative energetics of propagation and termination. The propagation step involves coordination of an ethylene molecule to the butyl-metal intermediate **3** to generate **6** (Scheme 4.2.2), which is exothermic by 12.3 and 12.6 kcal mol^{-1} for Co and Ni, respectively. The subsequent insertion steps required for oligomerization are computed to have activation enthalpies of 24.7 and 8.9 kcal mol^{-1} for Co and Ni, respectively (Table 4.2.1). These
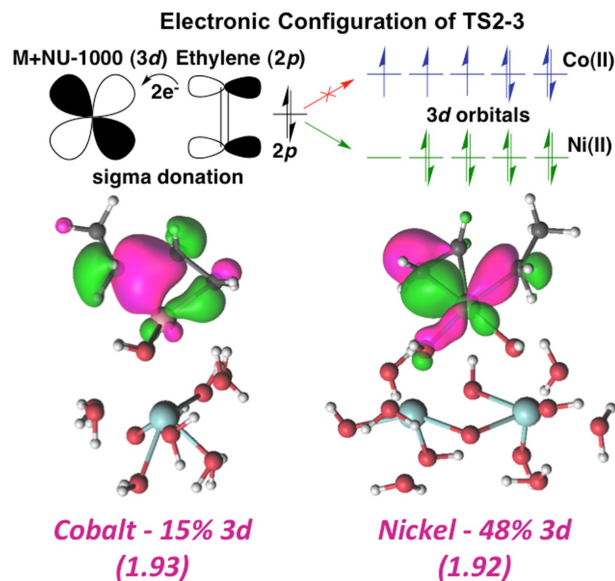
Figure 4.2.7: Electronic configuration of **TS2-3** of Co(II)-AIM+ and Ni(II)-AIM+NU-1000, where Ni(II) better stabilizes the frontier MO through hybridization with an empty d orbital. The frontier MOs are shown with d orbital percentage amplitudes and CASSCF occupation numbers in parentheses.

$\Delta H^{\ddagger}$ values are similar to those for the competing β-hydride elimination reactions, 22.7 and 8.4 kcal mol^{-1} for Co and Ni, respectively. As propagation and termination are similar from a kinetic standpoint, it is clear that the distribution of α-olefins will be sensitive to the partial pressure of ethylene in the MOF interior. In addition, while we have not studied it here, it is likely that local accessible volume constraints imposed by the organic linkers in the MOF framework may significantly reduce the ability of ethylene to approach the open metal site as oligomers of increasing length occupy that volume.
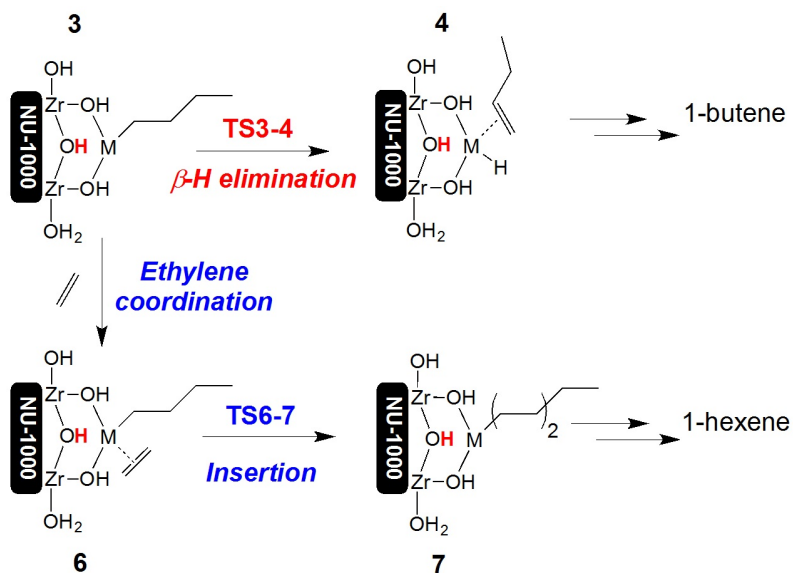
Scheme 4.2.2: Propagation *versus* Termination Step

Experimental Verification of Co-NU-1000 Catalytic Activity

Motivated by the above computational results, which suggest that ethylene dimerization should be catalyzed by Co-AIM+NU-1000, albeit with lower activity than that of Ni-AIM+NU-1000, we conducted experiments to assess its efficacy. As with Ni-AIM+NU-1000, Co-AIM+NU-1000 (both, in this case, prepared by atomic layer deposition (ALD) in MOFs (AIM)) can be transformed into its catalytically active form by the addition of Et_2AlCl under air- and moisture-free conditions. (See the supporting information for detailed experimental procedure.) During the first 10 hours on stream, there was a constant loss of the catalytic activity of the activated Co-AIM+NU-1000, similar to Ni-AIM+NU-1000.[294] The products were determined to be mainly butenes, including 1-butene ($\sim$70%), trans-2-butene ($\sim$20%), and cis-2-butene ($\sim$10%) (Figure 4.2.8). By varying the flow rates of ethylene, the TOF for this catalytic process was determined to

Catalyst	ΔH^{ab} (kcal mol^{-1})	
	Co-AIM+NU-1000	Ni-AIM+NU-1000
	Propagation Path	
6	-38.8	-41.8
TS6-7	-14.1 (24.7)	-32.9 (8.9)
7	-51.2	-51.7
	Termination Path	
3	-26.5	-29.2
TS3-4	-3.8 (22.7)	-20.8 (8.4)
4	-14.5	-30.7

Table 4.2.1: Computed enthalpies (298.15 K) for stationary points along propagation and termination step catalyzed by M-AIM+NU-1000 (M = Co and Ni).

[a]**1** and separated reactants as zero of enthalpy (see Figure 4.2.4).

[b]Activation enthalpies for elementary steps are shown in parentheses.

be ~0.012 s^{-1} on a per-cobalt-atom basis, ~5 times lower than that with Ni-AIM+NU-1000 under the same experimental conditions (Figure 4.2.9a). The apparent Arrhenius activation energy for this process is ~12.4 kcal mol^{-1} for Co-AIM+NU-1000 (Figure 4.2.9b), which ~4 kcal mol^{-1} higher than that for Ni-AIM+NU-1000.[294]

The differences between the calculated and experimental absolute activation energies/enthalpies (which are related by a factor of RT) are likely attributable to the nature of the employed cluster model, which focused on a mononuclear reactive site in order to understand relevant electronic structure details differentiating the metals. This model does not consider the influence of a second metal deposited on the same face of the NU-1000 node or on an adjacent face, although if such polynuclearity does not affect the local spin-state at each metal center, that same analysis as that presented in Figure 4.2.7 will hold. We note that the effect of the alkyl-aluminum precursor (Et$_2$AlCl) depositing directly onto the node, *i.e.*, to generate Al(III)+NU-1000,[274] has also been studied and been found not to affect the overall reactivity trend, *i.e.*, Ni-AIM+NU-1000 remains more reactive than Co-AIM+NU-1000 (see supporting information). Our mononuclear
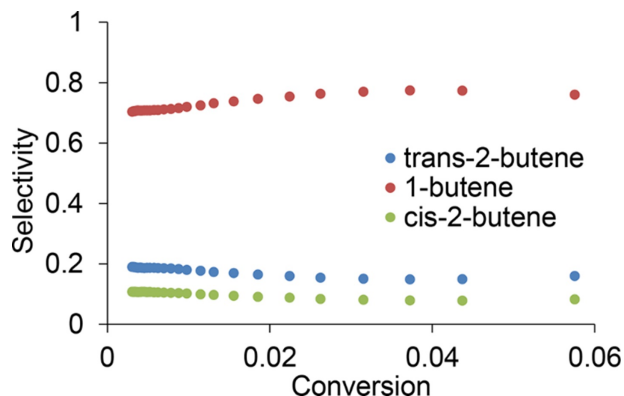
Figure 4.2.8: Product distribution of ethylene dimerization by activated Co-AIM+NU-1000 at different ethylene conversion.

model successfully predicted, at low computational cost, the trend in catalytic ethylene dimerization activity subsequently confirmed by experiment. Theory further proved useful for rationalizing electronic structure effects on overall catalytic activity.

4.2.4   Conclusions

Ethylene oligomerization can be catalyzed by Co-AIM+ and Ni-AIM+NU-1000, upon activation with Et$_2$AlCl. In the Ni case, this reaction was originally suggested[294] to proceed *via* the formation of an ethyl-nickel intermediate. We have now elucidated the full dimerization mechanism and compared it with non-activated Ni-AIM+NU-1000, which showed no catalytic activity. A Co-AIM+NU-1000 analogue was examined computationally, and predicted to also be competent for the catalysis of ethylene dimerization, albeit with lower activity than Ni-AIM+NU-1000. This theoretical prediction was subsequently validated by experimental measurement.

For both Co-AIM+ and Ni-AIM+NU-1000, ethylene insertion into the ethyl-metal bond is the rate-determining step, with calculated activation enthalpies of 24.1 and 15.6 kcal mol^{-1} for mononuclear Co-AIM+ and Ni-AIM+NU-1000, respectively. The
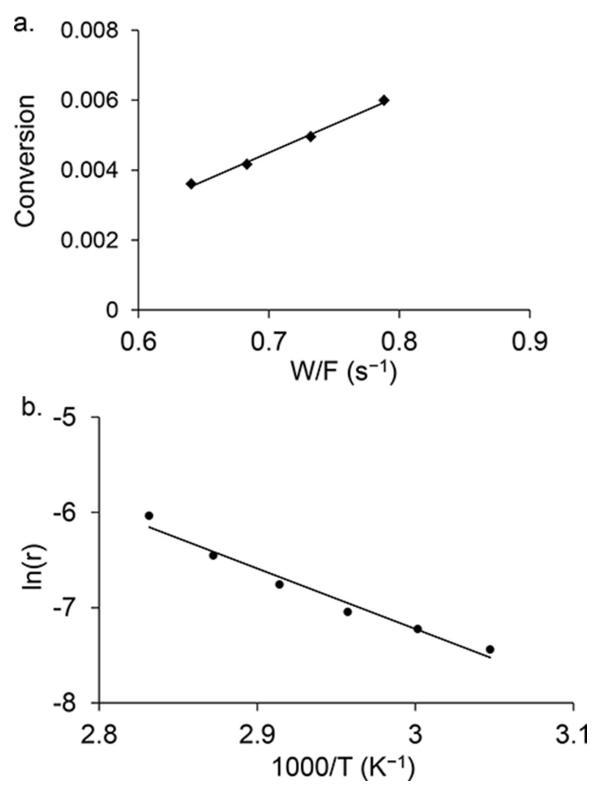
Figure 4.2.9: Catalytic conversion of ethylene dimerization by activated Co-AIM+NU-1000. a, TOF of ethylene dimerization. b, Arrhenius plot of ethylene dimerization reaction rates.

greater activity of the Ni(II) active site is attributed to TS stabilization associated with an empty $3d$ orbital that hybridizes more readily with relevant carbon p orbitals in low-spin Ni-AIM+NU-1000 than in high-spin Co-AIM+NU-1000. Nevertheless, based on computational and subsequent experimental results, we have demonstrated a first Co-AIM+NU-1000 supported catalyst that offers a promising route for the formation of linear products from olefins. While this new material has a higher activation enthalpy and lower TOF than that previously reported for Ni-AIM+NU-1000,[294] it contributes to our growing understanding of the structure-function relationship between transition-metal electronic configuration and catalytic activity for such catalysts, and points to broader opportunities for theory-guided discovery of new catalysts.

4.2.5 Acknowledgments

References

[1] P. Mal, D. Schultz, K. Beyeh, K. Rissanen, and J. R. Nitschke, *Angew Chem Int Ed*, vol. 47, no. 43, pp. 8297–8301, 2008.

[2] W. Meng, B. Breiner, K. Rissanen, J. D. Thoburn, J. K. Clegg, and J. R. Nitschke, *Angew Chem Int Ed*, vol. 50, no. 15, pp. 3479–3483, 2011.

[3] I. A. Riddell, M. M. J. Smulders, J. K. Clegg, Y. R. Hristova, B. Breiner, J. D. Thoburn, and J. R. Nitschke, *Nat Chem*, vol. 4, no. 9, pp. 751–756, 2012.

[4] B. Olenyuk, M. D. Levin, J. A. Whiteford, J. E. Shield, and P. J. Stang, *J Am Chem Soc*, vol. 121, no. 44, pp. 10434–10435, 1999.

[5] F. Bozoglian, S. Romain, M. Z. Ertem, T. K. Todorova, C. Sens, J. Mola, M. Rodriguez, I. Romero, J. Benet-Buchholz, X. Fontrodona, C. J. Cramer, L. Gagliardi, and A. Llobet, *J Am Chem Soc*, vol. 131, no. 42, pp. 15176–15187, 2009.

[6] A. Poater *Catal Commun*, vol. 44, pp. 2–5, 2014.

[7] S. J. Coles and P. A. Gale, *Chem Sci*, vol. 3, no. 3, pp. 683–689, 2012.

[8] P. Hohenberg and W. Kohn, *Physical Review*, vol. 136, no. 3B, pp. B864–B871, 1964.

[9] C. J. Cramer, *Essentials of Computational Chemistry: Theories and Models*. Wiley, 2004.

[10] W. Kohn and L. J. Sham, *Physical Review*, vol. 140, no. 4A, pp. A1133–A1138, 1965.

[11] Y. Zhao and D. G. Truhlar, *J Chem Phys*, vol. 125, no. 19, p. 194101, 2006.

[12] J. Antony and S. Grimme, *Phys Chem Chem Phys*, vol. 8, no. 45, pp. 5287–5293, 2006.

[13] S. Grimme, J. Antony, S. Ehrlich, and H. Krieg, *J Chem Phys*, vol. 132, no. 15, p. 154104, 2010.

[14] S. Grimme, S. Ehrlich, and L. Goerigk, *J Comp Chem*, vol. 32, no. 7, pp. 1456–1465, 2011.

[15] A. V. Marenich, C. J. Cramer, and D. G. Truhlar, *J Phys Chem B*, vol. 113, no. 18, pp. 6378–6396, 2009.

[16] C. Sens, I. Romero, M. Rodriguez, A. Llobet, T. Parella, and J. Benet-Buchholz, *J Am Chem Soc*, vol. 126, no. 25, pp. 7798–7799, 2004.

[17] M. Hirahara, M. Z. Ertem, M. Komi, H. Yamazaki, C. J. Cramer, and M. Yagi, *Inorg Chem*, vol. 52, no. 11, pp. 6354–6364, 2013.

[18] D. Cram, M. Tanner, and R. Thomas, *Angew Chem Int Ed*, vol. 30, no. 8, pp. 1024–1027, 1991.

[19] R. W. Saalfrank, H. Maid, and A. Scheurer, *Angew Chem Int Ed*, vol. 47, no. 46, pp. 8794–8824, 2008.

[20] B. Breiner, J. K. Clegg, and J. R. Nitschke, *Chem Sci*, vol. 2, no. 1, pp. 51–56, 2011.

[21] M. Fujita, M. Tominaga, A. Hori, and B. Therrien, *Acc Chem Res*, vol. 38, no. 4, pp. 369–378, 2005.

[22] S. R. Seidel and P. J. Stang, *Acc Chem Res*, vol. 35, no. 11, pp. 972–983, 2002.

[23] N. Armaroli and V. Balzani, *ChemSusChem*, vol. 4, no. 1, pp. 21–36, 2011.

[24] S. Berardi, S. Drouet, L. Francas, C. Gimbert-Surinach, M. Guttentag, C. Richmond, T. Stoll, and A. Llobet, *Chem Soc Rev*, vol. 43, no. 22, pp. 7501–7519, 2014.

[25] D. Kim, K. K. Sakimoto, D. Hong, and P. Yang, *Angew Chem*, vol. 127, no. 11, pp. 3309–3316, 2015.

[26] J. M. Thomas *Energy Environ Sci*, vol. 7, no. 1, pp. 19–20, 2014.

[27] A. Fujishima and K. Honda, *Nature*, vol. 238, no. 5358, pp. 37–8, 1972.

[28] K. Sanderson *Nature*, vol. 452, no. 7186, pp. 400–402, 2008.

[29] M. W. Kanan and D. G. Nocera, *Science*, vol. 321, no. 5892, pp. 1072–1075, 2008.

[30] T. Arai, S. Sato, T. Kajino, and T. Morikawa, *Energy Environ Sci*, vol. 6, no. 4, pp. 1274–1282, 2013.

[31] S. W. Gersten, G. J. Samuels, and T. J. Meyer, *J Am Chem Soc*, vol. 104, no. 14, pp. 4029–4030, 1982.

[32] J. D. Blakemore, R. H. Crabtree, and G. W. Brudvig, *Chem Rev*, vol. 115, no. 23, pp. 12974–13005, 2015.

[33] Y. Xu, A. Fischer, L. Duan, L. Tong, E. Gabrielsson, B. Aakermark, and L. Sun, *Angew Chem Int Ed*, vol. 49, no. 47, pp. 8934–8937, 2010.

[34] T. M. Laine, M. D. Kaerkaes, R.-Z. Liao, P. E. M. Siegbahn, and B. Aakermark, *Chem Eur J*, vol. 21, no. 28, pp. 10039–10048, 2015.

[35] L.-Z. Zeng, C.-J. Wang, T.-T. Li, X. Gan, C. Li, and W.-F. Fu, *Catal Commun*, vol. 68, pp. 84–87, 2015.

[36] A. C. Sander, A. Schober, S. Dechert, and F. Meyer, *Eur J Inorg Chem*, vol. 2015, no. 26, pp. 4348–4353, 2015.

[37] S. Neudeck, S. Maji, I. Lopez, S. Meyer, F. Meyer, and A. Llobet, *J Am Chem Soc*, vol. 136, no. 1, pp. 24–27, 2014.

[38] T. Wada, K. Tsuge, and K. Tanaka, *Inorg Chem*, vol. 40, no. 2, pp. 329–337, 2001.

[39] J. Mola, C. Dinoi, X. Sala, M. Rodriguez, I. Romero, T. Parella, X. Fontrodona, and A. Llobet, *Dalton Trans*, vol. 40, no. 14, pp. 3640–3646, 2011.

[40] S. Maji, L. Vigara, F. Cottone, F. Bozoglian, J. Benet-Buchholz, and A. Llobet, *Angew Chem Int Ed*, vol. 51, no. 24, pp. 5967–5970, 2012.

[41] Z. Deng, H.-W. Tseng, R. Zong, D. Wang, and R. Thummel, *Inorg Chem*, vol. 47, no. 6, pp. 1835–1848, 2008.

[42] Y. Jiang, F. Li, B. Zhang, X. Li, X. Wang, F. Huang, and L. Sun, *Angew Chem Int Ed*, vol. 52, no. 12, pp. 3398–3401, 2013.

[43] S. Roeser, M. Z. Ertem, C. Cady, R. Lomoth, J. Benet-Buchholz, L. Hammarstrom, B. Sarkar, W. Kaim, C. J. Cramer, and A. Llobet, *Inorg Chem*, vol. 51, no. 1, pp. 320–327, 2012.

[44] J. Mola, E. Mas-Marza, X. Sala, I. Romero, M. Rodriguez, C. Vinas, T. Parella, and A. Llobet, *Angew Chem Int Ed*, vol. 47, no. 31, pp. 5830–5832, 2008.

[45] L. Francas, X. Sala, J. Benet-Buchholz, L. Escriche, and A. Llobet, *ChemSusChem*, vol. 2, no. 4, pp. 321–329, 2009.

[46] J. Aguilo, L. Francas, H. J. Liu, R. Bofill, J. Garcia-Anton, J. Benet-Buchholz, A. Llobet, L. Escriche, and X. Sala, *Catal Sci Technol*, vol. 4, no. 1, pp. 190–199, 2014.

[47] L. Francas, X. Sala, E. Escudero-Adan, J. Benet-Buchholz, L. Escriche, and A. Llobet, *Inorg Chem*, vol. 50, no. 7, pp. 2771–2781, 2011.

[48] D. J. Wasylenko, C. Ganesamoorthy, M. A. Henderson, B. D. Koivisto, H. D. Osthoff, and C. P. Berlinguette, *J Am Chem Soc*, vol. 132, no. 45, pp. 16094–16106, 2010.

[49] J. J. Concepcion, J. W. Jurss, J. L. Templeton, and T. J. Meyer, *J Am Chem Soc*, vol. 130, no. 49, pp. 16462–16463, 2008.

[50] S. Berardi, L. Francas, S. Neudeck, S. Maji, J. Benet-Buchholz, F. Meyer, and A. Llobet, *ChemSusChem*, vol. 8, no. 21, pp. 3688–3696, 2015.

[51] S. Roeser, P. Farras, F. Bozoglian, M. Martinez-Belmonte, J. Benet-Buchholz, and A. Llobet, *ChemSusChem*, vol. 4, no. 2, pp. 197–207, 2011.

[52] H. D. Gafney and A. W. Adamson, *J Am Chem Soc*, vol. 94, no. 23, pp. 8238–9, 1972.

[53] M. C. DeRosa and R. J. Crutchley, *Coord Chem Rev*, vol. 233-234, pp. 351–371, 2002.

[54] D. Andrae, U. Haussermann, M. Dolg, H. Stoll, and H. Preuss, *Theor Chim Acta*, vol. 77, no. 2, pp. 123–141, 1990.

[55] W. J. Hehre, L. Radom, P. V. R. Schleyer, and J. Pople,, *Ab Initio Molecular Orbital Theory*. New York: Wiley, 1986.

[56] M. J. Frisch, G. W. Trucks, H. B. Schlegel, G. E. Scuseria, M. A. Robb, J. R. Cheeseman, G. Scalmani, V. Barone, B. Mennucci, G. A. Petersson, H. Nakatsuji, M. Caricato, X. Li, H. P. Hratchian, A. F. Izmaylov, J. Bloino, G. Zheng, J. L. Sonnenberg, M. Hada, M. Ehara, K. Toyota, R. Fukuda, J. Hasegawa, M. Ishida, T. Nakajima, Y. Honda, O. Kitao, H. Nakai, T. Vreven, J. J. A. Montgomery, J. E. Peralta, F. Ogliaro, M. Bearpark, J. J. Heyd, E. Brothers, K. N. Kudin, V. N. Staroverov, R. Kobayashi, J. Normand, K. Raghavachari, A. Rendell, J. C. Burant, S. S. Iyengar, J. Tomasi, M. Cossi, N. Rega, J. M. Millam, M. Klene, J. E. Knox, J. B. Cross, V. Bakken, C. Adamo, J. Jaramillo, R. Gomperts, R. E. Stratmann, O. Yazyev, A. J. Austin, R. Cammi, C. Pomelli, J. W. Ochterski, R. L. Martin, K. Morokuma, V. G. Zakrzewski, G. A. Voth, P. Salvador, J. J. Dannenberg, S. Dapprich, A. D. Daniels, . Farkas, J. B. Foresman, J. V. Ortiz, J. Cioslowski, and D. J. Fox,, "Gaussian," 2009.

[57] M. D. Tissandier, K. A. Cowen, W. Y. Feng, E. Gundlach, M. H. Cohen, A. D. Earhart, J. V. Coe, and T. R. T. Jr., *J Phys Chem A*, vol. 102, no. 40, pp. 7787–7794, 1998.

[58] D. M. Camaioni and C. A. Schwerdtfeger, *J Phys Chem A*, vol. 109, no. 47, pp. 10795–10797, 2005.

[59] C. P. Kelly, C. J. Cramer, and D. G. Truhlar, *J Phys Chem B*, vol. 110, no. 32, pp. 16066–16081, 2006.

[60] V. S. Bryantsev, M. S. Diallo, and W. G. III, *J Phys Chem B*, vol. 112, no. 32, pp. 9709–9719, 2008.

[61] A. Lewis, J. A. Bumpus, D. G. Truhlar, and C. J. Cramer, *J Chem Educ*, vol. 81, no. 4, pp. 596–604, 2004.

[62] P. Winget, C. J. Cramer, and D. G. Truhlar, *Theor Chem Acc*, vol. 112, no. 4, pp. 217–227, 2004.

[63] T. Ziegler, A. Rauk, and E. J. Baerends, *Theor Chim Acta*, vol. 43, no. 3, pp. 261–271, 1977.

[64] C. J. Cramer and D. G. Truhlar, *Phys Chem Chem Phys*, vol. 11, no. 46, pp. 10757–10816, 2009.

[65] K. Yamaguchi, F. Jensen, A. Dorigo, and K. N. Houk, *Chem Phys Lett*, vol. 149, no. 5-6, pp. 537–42, 1988.

[66] T. Soda, Y. Kitagawa, T. Onishi, Y. Takano, Y. Shigeta, H. Nagao, Y. Yoshioka, and K. Yamaguchi, *Chem Phys Lett*, vol. 319, no. 3, pp. 223–230, 2000.

[67] L. Noodleman, C. Y. Peng, D. A. Case, and J. M. Mouesca, *Coord Chem Rev*, vol. 144, pp. 199–244, 1995.

[68] I. Ciofini and C. A. Daul, *Coord Chem Rev*, vol. 238-239, pp. 187 – 209, 2003.

[69] J. N. Harvey *Structure and Bonding*, vol. 112, pp. 151–183, 2004.

[70] F. Neese *Coord Chem Rev*, vol. 253, no. 5, pp. 526–563, 2009.

[71] K. Kalyanasundaram *Coord Chem Rev*, vol. 46, no. OCT, pp. 159–244, 1982.

[72] A. Juris, V. Balzani, F. Barigelletti, S. Campagna, P. Belser, and A. Vonzelewsky, *Coord Chem Rev*, vol. 84, pp. 85–277, 1988.

[73] V. Balzani and A. Juris, *Coord Chem Rev*, vol. 211, pp. 97–115, 2001.

[74] M. Kirch, J. M. Lehn, and J. P. Sauvage, *Helv Chim Acta*, vol. 62, no. 4, pp. 1345–1384, 1979.

[75] D. A. Nicewicz and D. W. C. MacMillan, *Science*, vol. 322, no. 5898, pp. 77–80, 2008.

[76] D. V. Pinnick and B. Durham, *Inorg Chem*, vol. 23, no. 10, pp. 1440–1445, 1984.

[77] B. Durham, J. L. Walsh, C. L. Carter, and T. J. Meyer, *Inorg Chem*, vol. 19, no. 4, pp. 860–865, 1980.

[78] C. R. Hecker, P. E. Fanwick, and D. R. Mcmillin, *Inorg Chem*, vol. 30, no. 4, pp. 659–666, 1991.

[79] B. Durham, S. R. Wilson, D. J. Hodgson, and T. J. Meyer, *J Am Chem Soc*, vol. 102, no. 2, pp. 600–607, 1980.

[80] G. B. Porter and R. H. Sparks, *Journal of Photochemistry*, vol. 13, no. 2, pp. 123–131, 1980.

[81] H. Yamazaki, T. Hakamata, M. Komi, and M. Yagi, *J Am Chem Soc*, vol. 133, no. 23, pp. 8846–8849, 2011.

[82] S. K. Padhi, R. Fukuda, M. Ehara, and K. Tanaka, *Inorg Chem*, vol. 51, no. 9, pp. 5386–5392, 2012.

[83] S. Miyazaki, T. Kojima, and S. Fukuzumi, *J Am Chem Soc*, vol. 130, no. 5, p. 1556, 2008.

[84] T. Wada, K. Tsuge, and K. Tanaka, *Angew Chem Int Ed*, vol. 39, no. 8, p. 1479, 2000.

[85] R. Zong and R. P. Thummel, *J Am Chem Soc*, vol. 127, no. 37, pp. 12802–12803, 2005.

[86] M. Yagi, S. Tajima, M. Komi, and H. Yamazaki, *Dalton Trans*, vol. 40, no. 15, pp. 3802–3804, 2011.

[87] D. J. Wasylenko, C. Ganesamoorthy, B. D. Koivisto, M. A. Henderson, and C. P. Berlinguette, *Inorg Chem*, vol. 49, no. 5, pp. 2202–2209, 2010.

[88] S. Masaoka and K. Sakai, *Chem Lett*, vol. 38, no. 2, pp. 182–183, 2009.

[89] J. L. Boyer, D. E. Polyansky, D. J. Szalda, R. Zong, R. P. Thummel, and E. Fujita, *Angew Chem Int Ed*, vol. 50, no. 52, pp. 12600–12604, 2011.

[90] T. Funaki, M. Yanagida, N. Onozawa-Komatsuzaki, K. Kasuga, Y. Kawanishi, and H. Sugihara, *Inorganica Chim Acta*, vol. 362, no. 7, pp. 2519–2522, 2009.

[91] N. Chanda, D. Paul, S. Kar, S. M. Mobin, A. Datta, V. G. Puranik, K. K. Rao, and G. K. Lahiri, *Inorg Chem*, vol. 44, no. 10, pp. 3499–3511, 2005.

[92] G. Sathyaraj, M. Kiruthika, T. Weyhermueller, and B. U. Nair, *Dalton Trans*, vol. 41, no. 27, pp. 8460–8471, 2012.

[93] T. Fujihara, T. Wada, and K. Tanaka, *Dalton Trans*, no. 4, pp. 645–652, 2004.

[94] R. F. Zong, F. Naud, C. Segal, J. Burke, F. Y. Wu, and R. Thummel, *Inorg Chem*, vol. 43, no. 20, pp. 6195–6202, 2004.

[95] X. J. Yang, F. Drepper, B. Wu, W. H. Sun, W. Haehnel, and C. Janiak, *Dalton Trans*, no. 2, pp. 256–267, 2005.

[96] D. Oyama, K. Yuzuriya, and T. Takase, *Acta Crystallographica Section E-Structure Reports Online*, vol. 67, pp. M737–U908, 2011.

[97] N. Gupta, N. Grover, G. A. Neyhart, W. G. Liang, P. Singh, and H. H. Thorp, *Angew Chem Int Ed*, vol. 31, no. 8, pp. 1048–1050, 1992.

[98] C. Sens, M. Rodriguez, I. Romero, A. Llobet, T. Parella, and J. Benet-Buchholz, *Inorg Chem*, vol. 42, no. 25, pp. 8385–8394, 2003.

[99] S. Bonnet, J. P. Collin, N. Gruber, J. P. Sauvage, and E. R. Schofield, *Dalton Trans*, no. 24, pp. 4654–4662, 2003.

[100] C. A. Bessel, J. A. Margarucci, J. H. Acquaye, R. S. Rubino, J. Crandall, A. J. Jircitano, and K. J. Takeuchi, *Inorg Chem*, vol. 32, no. 25, pp. 5779–5784, 1993.

[101] M. H. V. Huynh, J. M. Lasker, M. Wetzler, B. Mort, L. F. Szczepura, L. M. Witham, J. M. Cintron, A. C. Marschilok, L. J. Ackerman, R. K. Castellano, D. L. Jameson, M. R. Churchill, A. J. Jircitano, and K. J. Takeuchi, *J Am Chem Soc*, vol. 123, no. 36, pp. 8780–8784, 2001.

[102] S. Li, V. R. Cooper, T. Thonhauser, A. Puzder, and D. C. Langreth, *J Phys Chem A*, vol. 112, no. 38, pp. 9031–9036, 2008.

[103] S. A. Trammell, J. C. Wimbish, F. Odobel, L. A. Gallagher, P. M. Narula, and T. J. Meyer, *J Am Chem Soc*, vol. 120, no. 50, pp. 13248–13249, 1998.

[104] Y. Zhao and D. G. Truhlar, *Acc Chem Res*, vol. 41, no. 2, pp. 157–167, 2008.

[105] Y. Zhao and D. G. Truhlar, *Theor Chem Acc*, vol. 120, no. 1-3, pp. 215–241, 2008.

[106] O. Salomon, M. Reiher, and B. A. Hess, *J Chem Phys*, vol. 117, no. 10, pp. 4729–4737, 2002.

[107] R. Peverati and D. G. Truhlar, *J Phys Chem Lett*, vol. 3, no. 1, pp. 117–124, 2012.

[108] R. Chakrabarty, P. S. Mukherjee, and P. J. Stang, *Chem Rev*, vol. 111, no. 11, pp. 6810–6918, 2011.

[109] M. D. Ward *Chem Commun*, no. 30, pp. 4487–4499, 2009.

[110] S. J. Dalgarno, N. P. Power, and J. L. Atwood, *Coord Chem Rev*, vol. 252, no. 8-9, pp. 825–841, 2008.

[111] D. J. L. Tranchemontagne, Z. Ni, M. O'Keeffe, and O. M. Yaghi, *Angew Chem Int Ed*, vol. 47, no. 28, pp. 5136–5147, 2008.

[112] N. J. Young and B. P. Hay, *Chem Commun*, vol. 49, no. 14, pp. 1354–1379, 2013.

[113] M. Yoshizawa, J. K. Klosterman, and M. Fujita, *Angew Chem Int Ed*, vol. 48, no. 19, pp. 3418–3438, 2009.

[114] M. Yoshizawa, M. Tamura, and M. Fujita, *Science*, vol. 312, no. 5771, pp. 251–254, 2006.

[115] M. D. Pluth, R. G. Bergman, and K. N. Raymond, *Science*, vol. 316, no. 5821, pp. 85–88, 2007.

[116] C. J. Hastings, D. Fiedler, R. G. Bergman, and K. N. Raymond, *J Am Chem Soc*, vol. 130, no. 33, pp. 10977–10983, 2008.

[117] M. Kuil, T. Soltner, P. W. N. M. van Leeuwen, and J. N. H. Reek, *J Am Chem Soc*, vol. 128, no. 35, pp. 11344–11345, 2006.

[118] M. Otte, P. F. Kuijpers, O. Troeppner, I. Ivanovic-Burmazovic, J. N. H. Reek, and B. de Bruin, *Chem Eur J*, vol. 19, no. 31, pp. 10170–10178, 2013.

[119] Z. J. Wang, K. N. Clary, R. G. Bergman, K. N. Raymond, and F. D. Toste, *Nat Chem*, vol. 5, no. 2, pp. 100–103, 2013.

[120] T. Gunnlaugsson, M. Glynn, G. M. T. (nee Hussey), P. E. Kruger, and F. M. Pfeffer, *Coord Chem Rev*, vol. 250, no. 23-24, pp. 3094–3117, 2006.

[121] K. Kondo, A. Suzuki, M. Akita, and M. Yoshizawa, *Angew Chem Int Ed*, vol. 52, no. 8, pp. 2308–2312, 2013.

[122] S. S. Li, B. H. Northrop, Q. H. Yuan, L. J. Wan, and P. J. Stang, *Acc Chem Res*, vol. 42, pp. 249–259, 2008.

[123] J. L. Sessler, S. Camiolo, and P. A. Gale, *Coord Chem Rev*, vol. 240, no. 1-2, pp. 17–55, 2003.

[124] D. K. Smith and F. Diederich, *Top Curr Chem*, vol. 210, pp. 183–227, 2000.

[125] M. M. Watt, L. N. Zakharov, M. M. Haley, and D. W. Johnson, *Angew Chem Int Ed*, vol. 52, no. 39, pp. 10275–10280, 2013.

[126] V. M. Dong, D. Fiedler, B. Carl, R. G. Bergman, and K. N. Raymond, *J Am Chem Soc*, vol. 128, no. 45, pp. 14464–14465, 2006.

[127] P. Mal, B. Breiner, K. Rissanen, and J. R. Nitschke, *Science*, vol. 324, no. 5935, pp. 1697–1699, 2009.

[128] T. Sawada, M. Yoshizawa, S. Sato, and M. Fujita, *Nat Chem*, vol. 1, no. 1, pp. 53–56, 2009.

[129] M. Yoshizawa, M. Tamura, and M. Fujita, *Angew Chem Int Ed*, vol. 46, no. 21, pp. 3874–3876, 2007.

[130] I. A. Riddell, M. M. J. Smulders, J. K. Clegg, and J. R. Nitschke, *Chem Commun*, vol. 47, no. 1, pp. 457–459, 2011.

[131] N. Kishi, M. Akita, M. Kamiya, S. Hayashi, H.-F. Hsu, and M. Yoshizawa, *J Am Chem Soc*, vol. 135, no. 35, pp. 12976–12979, 2013.

[132] J. Berna, D. A. Leigh, M. Lubomska, S. M. Mendoza, E. M. Perez, P. Rudolf, G. Teobaldi, and F. Zerbetto, *Nat Mater*, vol. 4, no. 9, pp. 704–710, 2005.

[133] N. Sakai and S. Matile, *Langmuir*, vol. 29, no. 29, pp. 9031–9040, 2013.

[134] R. Custelcean, P. V. Bonnesen, N. C. Duncan, X. Zhang, L. A. Watson, G. V. Berkel, W. B. Parson, and B. P. Hay, *J Am Chem Soc*, vol. 134, no. 20, pp. 8525–8534, 2012.

[135] M. E. Belowich and J. F. Stoddart, *Chem Soc Rev*, vol. 41, no. 6, pp. 2003–2024, 2012.

[136] K. Osowska and O. S. Miljanic, *Angew Chem Int Ed*, vol. 50, no. 36, pp. 8345–8349, 2011.

[137] H. Bunzen, Nonappa, E. Kalenius, S. Hietala, and E. Kolehmainen, *Chem Eur J*, vol. 19, no. 39, pp. 12978–12981, 2013.

[138] V. E. Campbell, X. de Hatten, N. Delsuc, B. Kauffmann, I. Huc, and J. R. Nitschke, *Chem Eur J*, vol. 15, no. 25, pp. 6138–6142, 2009.

[139] J. Doemer, J. C. Slootweg, F. Hupka, K. Lammertsma, and F. E. Hahn, *Angew Chem Int Ed*, vol. 49, no. 36, pp. 6430–6433, 2010.

[140] Y. Wu, X.-P. Zhou, J.-R. Yang, and D. Li, *Chem Commun*, vol. 49, no. 33, pp. 3413–3415, 2013.

[141] J. Nitschke, T. Ronson, S. Zarra, and S. P. Black, *Chem Commun*, vol. 49, p. 24762490, 2012.

[142] R. A. Bilbeisi, J. K. Clegg, N. Elgrishi, X. de Hatten, M. Devillard, B. Breiner, P. Mal, and J. R. Nitschke, *J Am Chem Soc*, vol. 134, no. 11, pp. 5110–5119, 2012.

[143] A. Ferguson, M. A. Squire, D. Siretanu, D. Mitcov, C. Mathoniere, R. Clerac, and P. E. Kruger, *Chem Commun*, vol. 49, no. 16, pp. 1597–1599, 2013.

[144] S. Yi, V. Brega, B. Captain, and A. E. Kaifer, *Chem Commun*, vol. 48, no. 83, pp. 10295–10297, 2012.

[145] O. Chepelin, J. Ujma, X. Wu, A. M. Z. Slawin, M. B. Pitak, S. J. Coles, J. Michel, A. C. Jones, P. E. Barran, and P. J. Lusby, *J Am Chem Soc*, vol. 134, no. 47, pp. 19334–19337, 2012.

[146] Y. L. Liu, V. Kravtsov, R. D. Walsh, P. Poddar, H. Srikanth, and M. Eddaoudi, *Chem Commun*, no. 24, pp. 2806–2807, 2004.

[147] A. Stephenson and M. D. Ward, *Dalton Trans*, p. 1036010369, 2011.

[148] X.-P. Zhou, J. Liu, S.-Z. Zhan, J.-R. Yang, D. Li, K.-M. Ng, R. W.-Y. Sun, and C.-M. Che, *J Am Chem Soc*, vol. 134, no. 19, pp. 8042–8045, 2012.

[149] X.-P. Zhou, Y. Wu, and D. Li, *J Am Chem Soc*, vol. 135, no. 43, pp. 16062–16065, 2013.

[150] R. A. Bilbeisi, T. K. Ronson, and J. R. Nitschke, *Angew Chem Int Ed*, vol. 52, no. 34, pp. 9027–9030, 2013.

[151] W. Meng, T. K. Ronson, J. K. Clegg, and J. R. Nitschke, *Angew Chem Int Ed*, vol. 52, no. 3, pp. 1017–1021, 2013.

[152] K.-C. Sham, S.-M. Yiu, and H.-L. Kwong, *Inorg Chem*, vol. 52, no. 10, pp. 5648–5650, 2013.

[153] I. A. Riddell, Y. R. Hristova, J. K. Clegg, C. S. Wood, B. Breiner, and J. R. Nitschke, *J Am Chem Soc*, vol. 135, no. 7, pp. 2723–2733, 2013.

[154] W. Meng, T. K. Ronson, and J. R. Nitschke, *PNAS*, vol. 110, no. 26, pp. 10531–10535, 2013.

[155] W. Meng, J. K. Clegg, and J. R. Nitschke, *Angew Chem Int Ed*, vol. 51, no. 8, pp. 1881–1884, 2012.

[156] A. Ustinov, H. Weissman, E. Shirman, I. Pinkas, X. Zuo, and B. Rybtchinski, *J Am Chem Soc*, vol. 133, no. 40, pp. 16201–16211, 2011.

[157] M. Han, R. Michel, B. He, Y.-S. Chen, D. Stalke, M. John, and G. H. Clever, *Angew Chem Int Ed*, vol. 52, no. 4, pp. 1319–1323, 2013.

[158] D. T. Bong, T. D. Clark, J. R. Granja, and M. R. Ghadiri, *Angew Chem Int Ed*, vol. 40, no. 6, pp. 988–1011, 2001.

[159] N. Kimizuka, T. Kawasaki, K. Hirata, and T. Kunitake, *J Am Chem Soc*, vol. 117, no. 23, pp. 6360–6361, 1995.

[160] S. Matile, A. Som, and N. Sorde, *Tetrahedron*, vol. 60, no. 31, pp. 6405–6435, 2004.

[161] D. Ajami and J. R. Jr., *Acc Chem Res*, vol. 46, no. 4, pp. 990–999, 2013.

[162] M. Aoyagi, S. Tashiro, M. Tominaga, K. Biradha, and M. Fujita, *Chem Commun*, no. 18, pp. 2036–2037, 2002.

[163] M. Tominaga, S. Tashiro, M. Aoyagi, and M. Fujita, *Chem Commun*, no. 18, pp. 2038–2039, 2002.

[164] H. T. Chifotides, I. D. Giles, and K. R. Dunbar, *J Am Chem Soc*, vol. 135, no. 8, pp. 3039–3055, 2013.

[165] C. R. K. Glasson, G. V. Meehan, C. A. Motti, J. K. Clegg, M. S. Davies, and L. F. Lindoy, *Aust J Chem*, vol. 65, no. 10, pp. 1371–1376, 2012.

[166] S. J. Hibble, S. M. Cheyne, A. C. Hannon, and S. G. Eversfield, *Inorg Chem*, vol. 41, no. 5, pp. 1042–1044, 2002.

[167] A. Veldkamp and G. Frenking, *Organometallics*, vol. 12, no. 11, pp. 4613–4622, 1993.

[168] W. S. Selig *Microchemical Journal*, vol. 32, no. 1, pp. 18–23, 1985.

[169] R. F. Ludlow and S. Otto, *Chem Soc Rev*, vol. 37, no. 1, pp. 101–108, 2008.

[170] J. D. Badjic, V. Balzani, A. Credi, S. Silvi, and J. F. Stoddart, *Science*, vol. 303, no. 5665, pp. 1845–1849, 2004.

[171] J. V. Hernandez, E. R. Kay, and D. A. Leigh, *Science*, vol. 306, no. 5701, pp. 1532–1537, 2004.

[172] N. C. Gianneschi, S. T. Nguyen, and C. A. Mirkin, *J Am Chem Soc*, vol. 127, no. 6, pp. 1644–1645, 2005.

[173] P. Thordarson, E. J. A. Bijsterveld, A. E. Rowan, and R. J. M. Nolte, *Nature*, vol. 424, no. 6951, pp. 915–918, 2003.

[174] D. Ray, J. T. Foy, R. P. Hughes, and I. Aprahamian, *Nat Chem*, vol. 4, no. 9, pp. 757–762, 2012.

[175] G. Hilson and A. J. Monhemius, *J Clean Prod*, vol. 14, no. 12-13, pp. 1158–1167, 2006.

[176] J. P. Perdew, K. Burke, and M. Ernzerhof, *Phys Rev Lett*, vol. 77, no. 18, pp. 3865–3868, 1996.

[177] "ADF," 2013.

[178] C. F. Guerra, J. G. Snijders, G. te Velde, and E. J. Baerends, *Theor Chem Acc*, vol. 99, no. 6, pp. 391–403, 1998.

[179] G. te Velde, F. M. Bickelhaupt, E. J. Baerends, C. F. Guerra, S. J. A. V. Gisbergen, J. G. Snijders, and T. Ziegler, *J Comp Chem*, vol. 22, no. 9, pp. 931–967, 2001.

[180] E. V. Lenthe and E. J. Baerends, *J Comp Chem*, vol. 24, no. 9, pp. 1142–1156, 2003.

[181] E. V. Lenthe, E. J. Baerends, and J. G. Snijders, *J Chem Phys*, vol. 99, no. 6, pp. 4597–4610, 1993.

[182] E. V. Lenthe, E. J. Baerends, and J. G. Snijders, *J Chem Phys*, vol. 101, no. 11, pp. 9783–9792, 1994.

[183] E. van Lenthe, A. Ehlers, and E. J. Baerends, *J Chem Phys*, vol. 110, no. 18, pp. 8943–8953, 1999.

[184] C. C. Pye and T. Ziegler, *Theor Chem Acc*, vol. 101, no. 6, pp. 396–408, 1999.

[185] M. Raducan, C. Rodriguez-Escrich, X. C. Cambeiro, E. C. Escudero-Adan, M. A. Pericas, and A. M. Echavarren, *Chem Commun*, vol. 47, no. 17, pp. 4893–4895, 2011.

[186] M. Han, D. M. Engelhard, and G. H. Clever, *Chem Soc Rev*, vol. 43, no. 6, pp. 1848–1860, 2014.

[187] K. Harris, D. Fujita, and M. Fujita, *Chem Commun*, vol. 49, no. 60, pp. 6703–6712, 2013.

[188] T. K. Ronson, J. Fisher, L. P. Harding, and M. J. Hardie, *Angew Chem Int Ed*, vol. 46, no. 47, pp. 9086–9088, 2007.

[189] C. Guetz, R. Hovorka, C. Klein, Q.-Q. Jiang, C. Bannwarth, M. Engeser, C. Schmuck, W. Assenmacher, W. Mader, F. Topic, K. Rissanen, S. Grimme, and A. Luetzen, *Angew Chem Int Ed*, vol. 53, no. 6, pp. 1693–1698, 2014.

[190] K. Ghosh, J. Hu, H. S. White, and P. J. Stang, *J Am Chem Soc*, vol. 131, no. 19, p. 6695, 2009.

[191] S. Mukherjee and P. S. Mukherjee, *Chem Commun*, vol. 50, no. 18, pp. 2239–2248, 2014.

[192] M. D. Ward and P. R. Raithby, *Chem Soc Rev*, vol. 42, no. 4, pp. 1619–1636, 2013.

[193] M. Yoshizawa, S. Miyagi, M. Kawano, K. Ishiguro, and M. Fujita, *J Am Chem Soc*, vol. 126, no. 30, pp. 9172–9173, 2004.

[194] M. Yoshizawa, Y. Takeyama, T. Okano, and M. Fujita, *J Am Chem Soc*, vol. 125, no. 11, pp. 3243–3247, 2003.

[195] M. B. Duriska, S. M. Neville, J. Lu, S. S. Iremonger, J. F. Boas, C. J. Kepert, and S. R. Batten, *Angew Chem Int Ed*, vol. 48, no. 47, pp. 8919–8922, 2009.

[196] C. J. Hastings, M. D. Pluth, R. G. Bergman, and K. N. Raymond, *J Am Chem Soc*, vol. 132, no. 20, p. 6938, 2010.

[197] T. Murase, S. Horiuchi, and M. Fujita, *J Am Chem Soc*, vol. 132, no. 9, p. 2866, 2010.

[198] Y. Jiao, J. Wang, P. Wu, L. Zhao, C. He, J. Zhang, and C. Duan, *Chem Eur J*, vol. 20, no. 8, pp. 2224–2231, 2014.

[199] D. Samanta, S. Mukherjee, Y. P. Patil, and P. S. Mukherjee, *Chem Eur J*, vol. 18, no. 39, pp. 12322–12329, 2012.

[200] K. Nakabayashi, M. Kawano, and M. Fujita, *Angew Chem Int Ed*, vol. 44, no. 33, pp. 5322–5325, 2005.

[201] S. Horiuchi, T. Murase, and M. Fujita, *J Am Chem Soc*, vol. 133, no. 32, pp. 12445–12447, 2011.

[202] M. Yoshizawa, T. Kusukawa, M. Fujita, and K. Yamaguchi, *J Am Chem Soc*, vol. 122, no. 26, pp. 6311–6312, 2000.

[203] T. Furusawa, M. Kawano, and M. Fujita, *Angew Chem Int Ed*, vol. 46, no. 30, pp. 5717–5719, 2007.

[204] D. W. Johnson and K. N. Raymond, *Inorg Chem*, vol. 40, no. 20, pp. 5157–5161, 2001.

[205] I. S. Tidmarsh, T. B. Faust, H. Adams, L. P. Harding, L. Russo, W. Clegg, and M. D. Ward, *J Am Chem Soc*, vol. 130, no. 45, pp. 15167–15175, 2008.

[206] N. Kishi, Z. Li, K. Yoza, M. Akita, and M. Yoshizawa, *J Am Chem Soc*, vol. 133, no. 30, pp. 11438–11441, 2011.

[207] K. Mahata, P. D. Frischmann, and F. Wuerthner, *J Am Chem Soc*, vol. 135, no. 41, pp. 15656–15661, 2013.

[208] S. Mirtschin, A. Slabon-Turski, R. Scopelliti, A. H. Velders, and K. Severin, *J Am Chem Soc*, vol. 132, no. 40, pp. 14004–14005, 2010.

[209] K. Li, L.-Y. Zhang, C. Yan, S.-C. Wei, M. Pan, L. Zhang, and C.-Y. Su, *J Am Chem Soc*, vol. 136, no. 12, pp. 4456–4459, 2014.

[210] Y.-R. Zheng, Z. Zhao, H. Kim, M. Wang, K. Ghosh, J. B. Pollock, K.-W. Chi, and P. J. Stang, *Inorg Chem*, vol. 49, no. 22, pp. 10238–10240, 2010.

[211] B. Therrien *Chem Eur J*, vol. 19, no. 26, pp. 8378–8386, 2013.

[212] J. E. M. Lewis, E. L. Gavey, S. A. Cameron, and J. D. Crowley, *Chem Sci*, vol. 3, no. 3, pp. 778–784, 2012.

[213] S. J. Lee, A. G. Hu, and W. B. Lin, *J Am Chem Soc*, vol. 124, no. 44, pp. 12948–12949, 2002.

[214] T. Nakamura, H. Ube, and M. Shionoya, *Chem Lett*, vol. 42, no. 4, pp. 328–334, 2013.

[215] M. Han, R. Michel, and G. H. Clever, *Chem Eur J*, vol. 20, no. 34, pp. 10640–10644, 2014.

[216] T. K. Ronson, S. Zarra, S. P. Black, and J. R. Nitschke, *Chem Commun*, vol. 49, no. 25, pp. 2476–2490, 2013.

[217] F. Reichel, J. K. Clegg, K. Gloe, K. Gloe, J. J. Weigand, J. K. Reynolds, C.-G. Li, J. R. Aldrich-Wright, C. J. Kepert, L. F. Lindoy, H.-C. Yao, and F. Li, *Inorg Chem*, vol. 53, no. 2, pp. 688–690, 2014.

[218] A. M. Castilla, W. J. Ramsay, and J. R. Nitschke, *Acc Chem Res*, vol. 47, no. 7, pp. 2063–2073, 2014.

[219] V. E. Campbell, R. Guillot, E. Riviere, P.-T. Brun, W. Wemsdorfer, and T. Mallah, *Inorg Chem*, vol. 52, no. 9, pp. 5194–5200, 2013.

[220] S. Ma, M. M. J. Smulders, Y. R. Hristova, J. K. Clegg, T. K. Ronson, S. Zarra, and J. R. Nitschke, *J Am Chem Soc*, vol. 135, no. 15, pp. 5678–5684, 2013.

[221] P. P. Neelakandan, A. Jimenez, and J. R. Nitschke, *Chem Sci*, vol. 5, no. 3, pp. 908–915, 2014.

[222] J. L. Bolliger, A. M. Belenguer, and J. R. Nitschke, *Angew Chem Int Ed*, vol. 52, no. 31, pp. 7958–7962, 2013.

[223] M. C. Young, L. R. Holloway, A. M. Johnson, and R. J. Hooley, *Angew Chem Int Ed*, vol. 53, no. 37, pp. 9832–9836, 2014.

[224] M. Albrecht, Y. Shang, K. Hasui, V. Gossen, G. Raabe, K. Tahara, and Y. Tobe, *Dalton Trans*, vol. 41, no. 31, pp. 9316–9322, 2012.

[225] N. Miyaura and A. Suzuki, *Chem Rev*, vol. 95, no. 7, pp. 2457–2483, 1995.

[226] P. J. Stang, B. Olenyuk, D. C. Muddiman, and R. D. Smith, *Organometallics*, vol. 16, no. 14, pp. 3094–3096, 1997.

[227] R. W. Saalfrank, B. Demleitner, H. Glaser, H. Maid, D. Bathelt, F. Hampel, W. Bauer, and M. Teichert, *Chem Eur J*, vol. 8, no. 12, pp. 2679–2683, 2002.

[228] R. W. Saalfrank, H. Maid, A. Scheurer, R. Puchta, and W. Bauer, *Eur J Inorg Chem*, no. 19, pp. 2903–2906, 2010.

[229] T. Beissel, R. E. Powers, T. N. Parac, and K. N. Raymond, *J Am Chem Soc*, vol. 121, no. 17, pp. 4200–4206, 1999.

[230] W. Meng, J. K. Clegg, J. D. Thoburn, and J. R. Nitschke, *J Am Chem Soc*, vol. 133, no. 34, pp. 13652–13660, 2011.

[231] J. K. Clegg, J. Cremers, A. J. Hogben, B. Breiner, M. M. J. Smulders, J. D. Thoburn, and J. R. Nitschke, *Chem Sci*, vol. 4, no. 1, pp. 68–76, 2013.

[232] R. Ahlrichs, M. Bar, M. Haser, H. Horn, and C. Kolmel, *Chem Phys Lett*, vol. 162, no. 3, pp. 165–169, 1989.

[233] M. Sierka, A. Hogekamp, and R. Ahlrichs, *J Chem Phys*, vol. 118, no. 20, pp. 9136–9148, 2003.

[234] M. Haser and R. Ahlrichs, *J Comp Chem*, vol. 10, no. 1, pp. 104–111, 1989.

[235] O. Treutler and R. Ahlrichs, *J Chem Phys*, vol. 102, no. 1, pp. 346–354, 1995.

[236] M. V. Arnim and R. Ahlrichs, *J Comp Chem*, vol. 19, no. 15, pp. 1746–1757, 1998.

[237] J. S. Binkley, J. A. Pople, and W. J. Hehre, *J Am Chem Soc*, vol. 102, no. 3, pp. 939–947, 1980.

[238] F. Weigend and R. Ahlrichs, *Phys Chem Chem Phys*, vol. 7, no. 18, pp. 3297–3305, 2005.

[239] F. Weigend *Phys Chem Chem Phys*, vol. 8, no. 9, pp. 1057–1065, 2006.

[240] J. K. Clegg, F. Li, K. A. Jolliffe, G. V. Meehan, and L. F. Lindoy, *Chem Commun*, vol. 47, no. 21, pp. 6042–6044, 2011.

[241] M. Scherer, D. L. Caulder, D. W. Johnson, and K. N. Raymond, *Angew Chem Int Ed*, vol. 38, no. 11, pp. 1587–1592, 1999.

[242] T. Nakamura, H. Ube, R. Miyake, and M. Shionoya, *J Am Chem Soc*, vol. 135, no. 50, pp. 18790–18793, 2013.

[243] N. Kishi, M. Akita, and M. Yoshizawa, *Angew Chem*, vol. 126, no. 14, pp. 3678–3681, 2014.

[244] D. Canevet, E. M. Perez, and N. Martin, *Angew Chem Int Ed*, vol. 50, no. 40, pp. 9248–9259, 2011.

[245] I. Sanchez-Molina, B. Grimm, R. M. K. Calderon, C. G. Claessens, D. M. Guldi, and T. Torres, *J Am Chem Soc*, vol. 135, no. 28, pp. 10503–10511, 2013.

[246] K. N. Semenov, N. A. Charykov, V. A. Keskinov, A. K. Piartman, A. A. Blokhin, and A. A. Kopyrin, *J Chem Eng Data*, vol. 55, no. 1, pp. 13–36, 2010.

[247] G. J. Kleywegt and T. A. Jones, *Acta Crystallographica Section D-Biological Crystallography*, vol. 50, pp. 178–185, 1994.

[248] Y. Shoji, K. Tashiro, and T. Aida, *J Am Chem Soc*, vol. 126, no. 21, pp. 6570–6571, 2004.

[249] Q. Ji, R. C. Lirag, and O. S. Miljanic, *Chem Soc Rev*, vol. 43, no. 6, pp. 1873–1884, 2014.

[250] T. Friscic, R. W. Lancaster, L. Fabian, and P. G. Karamertzanis, *PNAS*, vol. 107, no. 30, pp. 13216–13221, 2010.

[251] K. Eichkorn, O. Treutler, H. Ohm, M. Haser, and R. Ahlrichs, *Chem Phys Lett*, vol. 242, no. 6, pp. 652–660, 1995.

[252] M. Flytzani-Stephanopoulos and B. C. Gates, *Annu Rev Chem Biomol Eng*, vol. 3, pp. 545–574, 2012.

[253] J. M. Thomas, R. Raja, and D. W. Lewis, *Angew Chem Int Ed*, vol. 44, no. 40, pp. 6456–6482, 2005.

[254] O. Deutschmann, H. Knözinger, K. Kochloefl, and T. Turek,, *Heterogeneous catalysis and solid catalysts, 2. development and types of solid catalysts*. Wiley-VCH Verlag GmbH & Co. KGaA: Weinheim, 2012.

[255] H. Juntgen *Fuel*, vol. 65, no. 10, pp. 1436–1446, 1986.

[256] R. J. Davis *J Catal*, vol. 216, no. 1-2, pp. 396–405, 2003.

[257] S. Horike, S. Shimomura, and S. Kitagawa, *Nat Chem*, vol. 1, no. 9, pp. 695–704, 2009.

[258] M. Eddaoudi, D. F. Sava, J. F. Eubank, K. Adil, and V. Guillerm, *Chem Soc Rev*, vol. 44, no. 1, pp. 228–249, 2015.

[259] G. Ferey *Chem Soc Rev*, vol. 37, no. 1, pp. 191–214, 2008.

[260] H. Furukawa, K. E. Cordova, M. O'Keeffe, and O. M. Yaghi, *Science*, vol. 341, no. 6149, p. 974, 2013.

[261] L. J. Murray, M. Dinca, and J. R. Long, *Chem Soc Rev*, vol. 38, no. 5, pp. 1294–1314, 2009.

[262] T. M. McDonald, J. A. Mason, X. Kong, E. D. Bloch, D. Gygi, A. Dani, V. Crocella, F. Giordanino, S. O. Odoh, W. S. Drisdell, B. Vlaisavljevich, A. L. Dzubak, R. Poloni, S. K. Schnell, N. Planas, K. Lee, T. Pascal, L. F. Wan, D. Prendergast, J. B. Neaton, B. Smit, J. B. Kortright, L. Gagliardi, S. Bordiga, J. A. Reimer, and J. R. Long, *Nature*, vol. 519, no. 7543, p. 303, 2015.

[263] L. E. Kreno, K. Leong, O. K. Farha, M. Allendorf, R. P. V. Duyne, and J. T. Hupp, *Chem Rev*, vol. 112, no. 2, pp. 1105–1125, 2012.

[264] J. Lee, O. K. Farha, J. Roberts, K. A. Scheidt, S. T. Nguyen, and J. T. Hupp, *Chem Soc Rev*, vol. 38, no. 5, pp. 1450–1459, 2009.

[265] L. Ma, C. Abney, and W. Lin, *Chem Soc Rev*, vol. 38, no. 5, pp. 1248–1256, 2009.

[266] F. Vermoortele, M. Vandichel, B. V. de Voorde, R. Ameloot, M. Waroquier, V. V. Speybroeck, and D. E. D. Vos, *Angew Chem Int Ed*, vol. 51, no. 20, pp. 4887–4890, 2012.

[267] A. J. Howarth, Y. Liu, P. Li, Z. Li, T. C. Wang, J. T. Hupp, and O. K. Farha, vol. 2016, no. 1, p. 15018., 2016.

[268] P. Deria, J. E. Mondloch, O. Karagiaridi, W. Bury, J. T. Hupp, and O. K. Farha, *Chem Soc Rev*, vol. 43, no. 16, pp. 5896–5912, 2014.

[269] K. Sumida, D. Stueck, L. Mino, J.-D. Chai, E. D. Bloch, O. Zavorotynska, L. J. Murray, M. Dinca, S. Chavan, S. Bordiga, M. Head-Gordon, and J. R. Long, *J Am Chem Soc*, vol. 135, no. 3, pp. 1083–1091, 2013.

[270] M. Meilikhov, K. Yusenko, D. Esken, S. Turner, G. Van Tendeloo, and R. A. Fischer, *Eur J Inorg Chem*, vol. 2010, no. 24, pp. 3701–3714, 2010.

[271] S. M. George *Chem Rev*, vol. 110, no. 1, pp. 111–131, 2010.

[272] J. E. Mondloch, W. Bury, D. Fairen-Jimenez, S. Kwon, E. J. DeMarco, M. H. Weston, A. A. Sarjeant, S. T. Nguyen, P. C. Stair, R. Q. Snurr, O. K. Farha, and J. T. Hupp, *J Am Chem Soc*, vol. 135, no. 28, pp. 10294–10297, 2013.

[273] N. Planas, J. E. Mondloch, S. Tussupbayev, J. Borycz, L. Gagliardi, J. T. Hupp, O. K. Farha, and C. J. Cramer, *J Phys Chem Lett*, vol. 5, no. 21, pp. 3716–3723, 2014.

[274] I. S. Kim, J. Borycz, A. E. Platero-Prats, S. Tussupbayev, T. C. Wang, O. K. Farha, J. T. Hupp, L. Gagliardi, K. W. Chapman, C. J. Cramer, and A. B. F. Martinson, *Chem Mater*, vol. 27, no. 13, pp. 4772–4778, 2015.

[275] A. Finiels, F. Fajula, and V. Hulea, *Catal Sci Technol*, vol. 4, no. 8, pp. 2412–2426, 2014.

[276] G. A. Somorjai and Y. Li,, *Introduction to Surface Chemistry and Catalysis*. Hoboken, NJ: John Wiley & Sons, Inc., 2010.

[277] H.-P. Koh and R. Hughes, *J Catal*, vol. 33, no. 1, pp. 7–16, 1974.

[278] M. Suzuki, K. Tsutsumi, and H. Takahashi, *Zeolites*, vol. 2, no. 3, pp. 185–192, 1982.

[279] A. Andreasen, *Predicting Formation Enthalpies of Metal Hydrides*. Roskilde: Pitney Bowes Management Services, 2004.

[280] F. Speiser, P. Braunstein, and W. Saussine, *Acc Chem Res*, vol. 38, no. 10, pp. 784–793, 2005.

[281] A. N. Mlinar, B. K. Keitz, D. Gygi, E. D. Bloch, J. R. Long, and A. T. Bell, *ACS Catal*, vol. 4, no. 3, pp. 717–721, 2014.

[282] S. T. Madrahimov, J. R. Gallagher, G. Zhang, Z. Meinhart, S. J. Garibay, M. Delferro, J. T. Miller, O. K. Farha, J. T. Hupp, and S. T. Nguyen, *ACS Catal*, vol. 5, no. 11, pp. 6713–6718., 2015.

[283] M. Rimoldi and A. Mezzetti, *Catal Sci Technol*, vol. 4, pp. 2724–2740., 2014.

[284] C. Martinez-Macias, P. Serna, and B. C. Gates, *ACS Catal*, vol. 5, no. 10, pp. 5647–5656., 2015.

[285] J. Lu, C. Martinez-Macias, C. Aydin, N. D. Browning, and B. C. Gates, *Catal Sci Technol*, vol. 3, no. 9, pp. 2199–2203., 2013.

[286] M. F. Delley, F. Núñez-Zarur, M. P. Conley, A. Comas-Vives, G. Siddiqi, S. Norsic, V. Monteil, O. V. Safonova, and C. Copéret, *PNAS*, vol. 111, no. 32, pp. 11624–11629., 2014.

[287] T. Maschmeyer, F. Rey, G. Sankar, and J. M. Thomas, *Nature*, vol. 378, pp. 159–162., 1995.

[288] R. Y. Brogaard and U. Olsbye, *ACS Catal*, vol. 6, no. 2, pp. 1204–1214., 2016.

[289] H. C. Zhou, J. R. Long, and O. M. Yaghi, vol. 112, no. 2, pp. 673–674., 2012.

[290] D. J. Xiao, E. D. Bloch, J. A. Mason, W. L. Queen, M. R. Hudson, N. Planas, J. Borycz, A. L. Dzubak, P. Verma, K. Lee, F. Bonino, V. Crocellà, J. Yano, S. Bordiga, D. G. Truhlar, L. Gagliardi, C. M. Brown, and J. R. Long, *Nat Chem*, vol. 6, pp. 590–595, 2014.

[291] K. Sumida, D. L. Rogow, J. A. Mason, T. M. McDonald, E. D. Bloch, Z. R. Herm, T. Bae, and J. R. Long, vol. 112, no. 2, pp. 724–781., 2012.

[292] N. L. Rosi, J. Eckert, M. Eddaoudi, D. T. Vodak, J. Kim, M. O'Keeffe, and O. M. Yaghi, vol. 300, no. 5622, pp. 1127–1129., 2003.

[293] M. H. Beyzavi, N. Vermeulen, A. J. Howarth, S. Tussupbayev, A. B. League, N. M. Schweitzer, J. R. Gallagher, A. E. Platero-Prats, N. Hafezi, A. A. Sarjeant, J. T. Miller, K. W. Chapman, J. F. Stoddart, C. J. Cramer, J. T. Hupp, and O. K. Farha, vol. 137, no. 42, pp. 13624–13631., 2015.

[294] Z. Li, N. M. Schweitzer, A. B. League, V. Bernales, A. W. Peters, A. B. Getsoian, T.C., Wang, T., M. J., A. Vjunov, J. L. Fulton, J. A. Lercher, C. J. Cramer, L. Gagliardi, J. T. Hupp, and O. K. Farha, vol. 138, no. 6, pp. 1977–1982., 2016.

[295] R. C. Klet, T. C. Wang, L. E. Fernandez, D. G. Truhlar, J. T. Hupp, and O. K. Farha, vol. 28, no. 4, pp. 1213–1219, 2016.

[296] A. W. Peters, Z. Li, O. K. Farha, and J. T. Hupp, *Acs Nano*, vol. 9, no. 8, pp. 8484–8490, 2015.

[297] C. W. Kung, J. E. Mondloch, T. C. Wang, W. Bury, W. Hoffeditz, B. M. Klahr, R. C. Klet, M. J. Pellin, O. K. Farha, and J. T. Hupp, vol. 7, no. 51, pp. 28223–28230., 2015.

[298] S. Yuan, Y. P. Chen, J. Qin, W. Lu, X. Wang, Q. Zhang, M. Bosch, T. F. Liu, X. Lian, and H. C. Zhou, vol. 54, no. 49, pp. 14696–14700, 2015.

[299] E. D. Metzger, C. K. Brozek, R. J. Comito, and M. Dinca, vol. 2, no. 3, pp. 148–153, 2016.

[300] R. C. Klet, S. Tussupbayev, J. Borycz, J. R. Gallagher, M. M. Stalzer, J. T. Miller, L. Gagliardi, J. T. Hupp, T. J. Marks, C. J. Cramer, M. Delferro, and O. K. Farha, vol. 137, no. 50, pp. 15680–15683, 2015.

[301] D. Yang, S. O. Odoh, T. C. Wang, O. K. Farha, J. T. Hupp, C. J. Cramer, L. Gagliardi, and G. B. C., vol. 137, no. 23, pp. 7391–7396, 2015.

[302] D. Yang, S. O. Odoh, J. Borycz, T. C. Wang, O. K. Farha, J. T. Hupp, C. J. Cramer, L. Gagliardi, and B. C. Gates, vol. 6, no. 1, pp. 235–247, 2015.

[303] S. Bauer, C. Serre, T. Devic, P. Horcajada, J. Marrot, G. Ferey, and N. Stock, vol. 47, no. 17, pp. 7568–7576., 2008.

[304] J. Canivet, S. Aguado, Y. Schuurman, and D. Farrusseng, vol. 135, no. 11, pp. 4195–4198, 2013.

[305] M. Stürzel, S. Mihan, and R. Mülhaupt, vol. 116, pp. 1398–1433, 2016.

[306] B. O. Roos, P. R. Taylor, and P. E. M. Siegbahn, vol. 48, p. 157, 1980.

[307] F. Aquilante, L. D. Vico, N. Ferré, G. Ghigo, P.-A. Malmqvist, P. Neogrády, T. B. Pedersen, M. Pitonak, M. Reiher, B. O. Roos, L. Serrano-Andrés, M. Urban, V. Veryazov, and R. J. Lindh, vol. 31, p. 224, 2010.

[308] B. O. Roos, R. Lindh, P. Malmqvist, V. Veryazov, and P. O. Widmark, vol. 108, p. 2851, 2004.

[309] B. O. Roos, R. Lindh, P. Malmqvist, V. Veryazov, and P. O. Widmark, vol. 109, p. 6575, 2005.

[310] M. Douglas and N. M. Kroll, vol. 33, p. 3742, 1986.

[311] F. Aquilante, T. B. Pedersen, and R. Lindh, vol. 126, p. 114107, 2007.

[312] T. Agapie, S. J. Schofer, J. A. Labinger, and J. E. Bercaw, vol. 126, no. 5, pp. 1304–1305, 2004.

[313] L. Fan, A. Krzywicki, A. Somogyvari, and T. Ziegler, vol. 35, no. 13, pp. 4003–4006, 1996.